



TECHNISCHE
UNIVERSITÄT
WIEN
Vienna | Austria

Generation of squeezed light with nanofiber-trapped atoms

DISSERTATION

zur Erlangung des akademischen Grades

Doktor der Naturwissenschaften

eingereicht von

Jakob Gillespie Hinney

Matrikelnummer 1429330

Badhausgasse 1-3, 1070 Wien

an der
Fakultät für Physik der Technischen Universität Wien

Betreuung: Prof. Dr. Arno Rauschenbeutel, E141 – Atominstitut / Humboldt Universität Berlin

Diese Dissertation haben begutachtet:

(Assoc. Prof. Jörg Helge
Müller)

(Prof. Philipp Treutlein)

Wien, 11.11.2019

(Jakob Gillespie Hinney)



Die approbierte gedruckte Originalversion dieser Dissertation ist an der TU Wien Bibliothek verfügbar.
The approved original version of this doctoral thesis is available in print at TU Wien Bibliothek.



TECHNISCHE
UNIVERSITÄT
WIEN
Vienna | Austria

Generation of squeezed light with nanofiber-trapped atoms

DISSERTATION

submitted in partial fulfillment of the requirements for the degree of

Doktor der Naturwissenschaften

by

Jakob Gillespie Hinney

Registration Number 1429330

Badhausgasse 1-3, 1070 Wien

to the Faculty of Physics
at the Vienna University of Technology

Advisor: Prof. Dr. Arno Rauschenbeutel, E141 – Atominstitut / Humboldt Universität Berlin

The dissertation has been reviewed by:

(Assoc. Prof. Jörg Helge
Müller)

(Prof. Philipp Treutlein)

Wien, 11.11.2019

(Jakob Gillespie Hinney)



Die approbierte gedruckte Originalversion dieser Dissertation ist an der TU Wien Bibliothek verfügbar.
The approved original version of this doctoral thesis is available in print at TU Wien Bibliothek.

Erklärung zur Verfassung der Arbeit

Jakob Gillespie Hinney
Badhausgasse 1-3, 1070 Wien

Hiermit erkläre ich, dass ich diese Arbeit selbständig verfasst habe, dass ich die verwendeten Quellen und Hilfsmittel vollständig angegeben habe und dass ich die Stellen der Arbeit - einschließlich Tabellen, Karten und Abbildungen -, die anderen Werken oder dem Internet im Wortlaut oder dem Sinn nach entnommen sind, auf jeden Fall unter Angabe der Quelle als Entlehnung kenntlich gemacht habe.

(Ort, Datum)

(Unterschrift Verfasserin)



Die approbierte gedruckte Originalversion dieser Dissertation ist an der TU Wien Bibliothek verfügbar.
The approved original version of this doctoral thesis is available in print at TU Wien Bibliothek.

Abstract

Ultra-thin tapered optical fibers have emerged as a versatile light-matter interface in recent years that combine a rich set of nano-optical features with good experimental accessibility. In this context an evanescent field dipole trap for laser cooled atoms was demonstrated for the first time in 2010 and since then a great set of experimental techniques was developed to control and study the trapped atom ensemble. Specifically, such interfaces can access the optical non-linearity of the ensemble that extends down to the single photon level. This sparked the question of realising non-classical states of light such as squeezed light.

In this context we constructed an experimental apparatus that realises an optical dipole trap for laser cooled Cesium atoms in the evanescent field of a nanofiber. In the first part of this thesis I describe the design and construction of the experiment and prove that atoms are trapped. The setup contains a number of technical improvements compared to previous realisations of nanofiber-based dipole traps. These include the use of magic wavelengths that reduce spectral broadening of the trapped ensemble, improved optical access through placing the nanofiber in a glass cell, and a transversally translateable fiber holder to optimize overlap between fiber waist and atom cloud. The second part of the thesis describes the experimental observation of squeezed light generated from a nanofiber-trapped ensemble of atoms. I demonstrate the squeezing and study the scaling with respect to the probe detuning and intensity. Our apparatus also allows us to study the spectrum of the optical field exiting the nanofiber and I show that this spectrum differs qualitatively for different sizes of the atomic ensemble. Specifically, I show that sidebands appear in the spectrum for sufficiently large ensembles.

Typically, the generation of squeezed light requires very strong non-linearities which are usually achieved through optical cavities or non-linear crystals. In this work I show that squeezed light can also be obtained from an ensemble of weakly coupled emitters. This suggests new perspectives for non-linear light-matter interfaces that are an essential building block for future optical quantum networks.



Die approbierte gedruckte Originalversion dieser Dissertation ist an der TU Wien Bibliothek verfügbar.
The approved original version of this doctoral thesis is available in print at TU Wien Bibliothek.

Kurzfassung

Ultra-dünne Glasfasern haben sich in den vergangenen Jahren als eine vielseitige Licht-Materie Schnittstelle erwiesen, bei der sich eine Fülle an nano-optischen Phänomenen mit guter experimenteller Handhabung verbinden. In diesem Zusammenhang wurde 2010 erstmals eine Dipolfalle für lasergekühlte Atome demonstriert, basierend auf dem evaneszenten Feld einer solchen Nanofaser. Seitdem wurde ein reichhaltiger Werkzeugkasten zur Kontrolle und Manipulation dieser faser-gefangenen Ensembles entwickelt. Insbesondere ermöglicht diese Schnittstelle Zugang zu optischen Nichtlinearitäten welche sich auch noch auf dem Level einzelner Photonen auswirken. Dies warf die Frage nach der Realisierung nicht-klassischer Zustände auf, etwa von gequetschtem Licht.

Vor diesem Hintergrund wurde im Rahmen der vorliegenden Arbeit ein neuer experimenteller Aufbau zum Fangen von laser-gekühlten Cäsium-Atomen im evaneszenten Feld einer Nanofaser geschaffen. Im ersten Teil der Arbeit beschreibe ich die Planung und Konstruktion des Experimentes und weise experimentell nach, dass Atome gefangen werden. Der Aufbau beinhaltet eine Reihe technischer Verbesserungen im Vergleich zu bisherigen nanofaser-basierten Dipolfallen. Dazu zählen die Verwendung sogenannter magischer Wellenlängen, welche die spektrale Verbreiterung des gefangenen Ensembles reduzieren, verbesserter optischer Zugang dank der Verwendung einer Glass-Vakuumkuvette, sowie ein transversal beweglicher Faserhalter zur Optimierung des Überlapps zwischen Atomwolke und der Taille der Nanofaser. Der zweite Teil der Arbeit beschreibt die experimentelle Beobachtung von gequetschtem Licht, welches durch ein Ensemble von schwach gekoppelten Emittlern realisiert wird. Dazu weise ich das Squeezing nach und untersuche die Skalierung desselben bezüglich Leistung und Verstimmung des Testfeldes. Zudem wird gezeigt, wie sich das Spektrum des aus der Faser austretenden Feldes qualitativ mit der Anzahl der gefangenen Atome ändert. Insbesondere wird nachgewiesen, dass bei ausreichender Atomzahl Seitenbänder im Spektrum erzeugt werden.

Die Erzeugung von gequetschtem Licht beruht in den meisten Fällen auf einer starken Nichtlinearität, welche durch optische Resonatoren oder nicht-lineare Kristalle gewährleistet wird. Die vorliegende Arbeit weißt jedoch nach, dass gequetschtes Licht auch durch ein Ensemble von schwach gekoppelten Emittlern erzeugt werden kann. Dadurch eröffnen sich neue Perspektiven für nicht-lineare Licht-Materie Schnittstellen, welche einen elementaren Baustein für zukünftige Quantennetzwerke darstellen.



Die approbierte gedruckte Originalversion dieser Dissertation ist an der TU Wien Bibliothek verfügbar.
The approved original version of this doctoral thesis is available in print at TU Wien Bibliothek.

List of Publications

The following articles will be published soon as a result of the work described in this thesis:

- A. Prasad, J. Hinney, S. Mahmoodian, K. Hammerer, S. Rind, P. Schneeweiss, A. S. Sørensen, J. Volz, and A. Rauschenbeutel. *Generation of correlated photons using non-interacting atoms weakly coupled to a guided optical mode. (in preparation)*
- J. Hinney, M. Schemmer, A. Prasad, S. Mahmoodian, K. Hammerer, S. Rind, P. Schneeweiss, A. S. Sørensen, J. Volz, and A. Rauschenbeutel. *Observation of squeezed light from an ensemble of weakly coupled emitters. (in preparation)*



Die approbierte gedruckte Originalversion dieser Dissertation ist an der TU Wien Bibliothek verfügbar.
The approved original version of this doctoral thesis is available in print at TU Wien Bibliothek.

*Stronger
Than Yesterday*

Britney Spears



Die approbierte gedruckte Originalversion dieser Dissertation ist an der TU Wien Bibliothek verfügbar.
The approved original version of this doctoral thesis is available in print at TU Wien Bibliothek.

Contents

1	Introduction	1
1.1	Light transmission through an ensemble of atoms	2
1.2	Studying light with optical nanofibers	3
1.3	Thesis structure overview	4
2	Properties of ultra-thin optical fibers	5
2.1	Electric field and intensity distributions	5
2.2	Principle of nanofiber-based dipole trapping	9
2.2.1	Atomic polarizability	9
2.2.2	Trapping potentials	10
2.2.3	Magic wavelength traps	12
2.2.4	Tensor polarizability at the magic wavelengths	14
2.3	Mechanical properties	14
2.4	Manufacturing of ultra-thin optical fibers	16
2.5	Summary	17
3	Squeezed light from non-linear photon transport	19
3.1	Squeezed light	19
3.1.1	Number states, coherent states, electric field	20
3.1.2	Quadratures	21
3.1.3	Squeezed vacuum	22
3.1.4	Phase-space portraits	24
3.1.5	Bright squeezed states	24
3.2	Detecting squeezed light	28
3.2.1	Losses	30
3.3	Non-linear photon transport	30
3.3.1	Strongly correlated photons	30
3.3.2	Transmission properties of the ensemble	32
3.3.3	From correlated photons to squeezed light	33
3.3.4	Detuned input field	35
3.4	Comparing measurement and theory	36
3.5	Summary	37

4	Construction of a nanofiber-based dipole trap	39
4.1	Vacuum chamber	39
4.1.1	Vacuum Pumps	41
4.1.2	Cesium sources	41
4.1.3	Glass cell	42
4.1.4	Translatable fiber mount	44
4.1.5	Placing a nanofiber in vacuum	44
4.2	Magnetic coil construction	46
4.3	Magneto-optical trapping of Cesium	48
4.3.1	Optical setup	48
4.3.2	Trap loading	50
4.3.3	Absorption imaging experiments	50
4.3.4	Microwave spectroscopy for bias coil calibration	53
4.4	Optical setup for interfacing the nanofiber	56
4.4.1	Polarization alignment	56
4.4.2	Ti:Sa probe laser	58
4.5	Experiment control	58
4.6	Realisation of dipole trapping in the evanescent field	59
4.6.1	Trap loading	59
4.6.2	Measuring optical depth	59
4.6.3	Trap optimization	61
4.6.4	Trap Lifetime	62
4.6.5	Measuring atom number and coupling strength	63
4.7	Optimizing the optical depth	65
4.8	Summary	67
5	Observation of Squeezed Light	69
5.1	Experimental Setup	69
5.1.1	Probing Setup	69
5.1.2	Homodyne Detection Setup	70
5.1.3	Detection losses	71
5.2	Balanced Detector Calibration	72
5.3	Experimental sequence and data acquisition	73
5.3.1	Stages of the sequence	73
5.3.2	Atom number estimate	73
5.4	Trace analysis	74
5.4.1	Detector spectra	75
5.4.2	Phase extraction	76
5.4.3	Variance extraction	76
5.4.4	Signal field amplitude	77
5.5	Observation of squeezed light	78
5.6	Detuned probing	79
5.7	Probe power dependence	80

5.8	The spectrum of squeezing	82
5.9	Squeezing from a free space ensemble	84
5.10	Possible experimental improvements	85
5.10.1	Reduce detection losses	85
5.10.2	Improve power balance	85
5.10.3	Reduce heating	86
5.11	Summary	87
6	Outlook and Conclusion	89
6.1	Further experiments	89
6.2	Squeezed light as a signature of non-linear interaction	90
	Appendices	91
A	Supplementary plots of squeezed states	93
A.1	Evolution of a coherent state with increasing squeezing	93
A.2	Phase dependence of squeezed states	93
B	Fiber analysis after removal from the vacuum	97
B.1	SEM images	97
B.2	Electron Energy Loss Spetroscopy	98
C	Supplementary material on Ch. 5	101
C.1	Oscilloscope setup	101
C.1.1	Sampling rate	101
C.1.2	Low-pass filter	101
C.2	The Wiener-Khinchin-Theorem	102
C.3	Comparing squeezed and coherent light	102
C.4	Detuning measurement	103
C.5	Power measurement	104
C.6	Squeezing spectra	104
C.7	Squeezing from a MOT cloud	104
	Bibliography	109



Die approbierte gedruckte Originalversion dieser Dissertation ist an der TU Wien Bibliothek verfügbar.
The approved original version of this doctoral thesis is available in print at TU Wien Bibliothek.

Introduction

The nature of light has puzzled minds for centuries. Simple observations like the refraction of white light in a prism and the subsequent colorful rainbow were the subject of intense debate. According to the German poet Johann Wolfgang von Goethe, for example, Isaac Newton had misunderstood the concept of color completely. In fact, Goethe himself considered his treatise *Zur Farbenlehre* (Theory of Color) [1] his most relevant contribution to mankind. He was confident enough to declare that he was the only one who had understood the subject. In his view the colors that the prism made visible were in fact created through the prism and did not exist before the interaction. They were rather a property of the prism than the incident light. Newton, on the other side, had argued, already more than a century before Goethe, that the white light contained all the colors and that the prism simply split them into separate directions [2]. As we know today, Newton's description was correct. Nevertheless, the argument reflected their fundamentally different idea of science: Goethe's approach of understanding the world was guided by subjective experience, from a modern perspective almost esoteric. Indeed, the more than 400 pages of the *Farbenlehre* contain not a single formula. Newton, on the other hand, postulated some of the most overarching principles in physics as equations. Considering this, it is maybe not too surprising that today Newton is seen as one of the greatest scientists in history while Goethe is remembered as a poet, a writer, a philosopher, but not so much as a scientist.

But is it not actually mind-boggling that a white light beam forms a rainbow after transmitting through a prism? Newton claimed that the color was contained in the white light but somehow revealed itself only through appropriate measurement devices. That white light has 'hidden' properties which can be missed if we don't unfold them carefully. Fifty years after Goethe, James Maxwell published his theory of the electro-magnetic field, which finally seemed to provide a complete description of light [3]. Here, color was in fact the wavelength of an electro-magnetic wave. The theory provided a good explanation for the rainbow emerging from the prism, consistent with Newton's understanding. For a while, light seemed to be solved. But then, again, 'hidden' properties were discovered: Although to our eyes seemingly an infinite number of brightness levels exist, light comes in discrete quanta of energy just like discrete

particles. And these particles still interfere like waves. And neither the particle nor the wave description seem intuitive from our daily experiences with rays of light.

Great progress regarding these observations was made since then and the early 20th century saw the development of a sophisticated quantum theory of light. This theory reconciles the apparent contradiction between the particle and the wave description. The theory states that the most classic state of light, a coherent state, has a well defined phase and, more importantly, finite electric field uncertainty. It even has the very same uncertainty as the vacuum electric field. And it was discovered that light can exhibit another quite peculiar feature: The electric field uncertainty can vary as a function of phase and cut below the minimum uncertainty of the vacuum. It has, so to speak, less noise than darkness. One can only wonder what Goethe would have made of this.

Such squeezed light is a non-classical phenomenon that can only be explained within the theory of quantum mechanics. A range of methods exist to generate non-classical states of light and in this thesis we present a novel and surprisingly simple way to create squeezed light.

1.1 Light transmission through an ensemble of atoms

We examine a very simple scenario: Resonant light propagates through an ensemble of atoms and is partially absorbed by them. Let us consider the light as a stream of photons and whenever a photon encounters an atom there is a certain probability of absorption, otherwise the photon propagates past. In the case of absorption the atom is transferred into an excited state that usually decays within a short time and the photon is emitted into a random direction. A simple depiction of this process is shown in Fig. 1.1a. This scattering reduces the intensity of the light as it propagates through an ensemble of atoms which is well described by Beer-Lambert's law that predicts an exponential reduction of intensity.

This description is usually perfectly sufficient to calculate how much light will exit the ensemble. But the applicability of Beer-Lambert's law is restricted to the limit of low intensity compared to the saturation intensity of an atom. The restriction originates from the fact that atoms are non-linear absorbers: Once a first photon is absorbed and the atom is excited it cannot absorb another photon as long as it stays in the excited state. This is the starting point of the field of non-linear light-matter interaction. But what happens actually when a pair of photons encounters an atom? The simplest process is that one photon is absorbed and the other transmitted. But another process is possible where the atom absorbs one photon, emits it a slightly different frequency, simultaneously absorbs the other photon and emits it again at a different frequency, just shifted with opposite sign. This two-photon process preserves energy because the total energy of the frequency shifted photons equals that of the initial two photons. Since a total of four photons are involved such processes are called four-wave mixing, although no more than two photons exist at any time. The optical non-linearity of atoms is well explained by quantum mechanics but incompatible with the classical picture that only knows linear absorbers. Therefore, light generated via this two-photon process is called non-classical light. A depiction of this two-photon process and the corresponding level scheme is shown in Fig. 1.1b.

So the simple scenario of classical light propagating through an ensemble can lead to non-classical light in the output. In this thesis we demonstrate this experimentally. As signature of

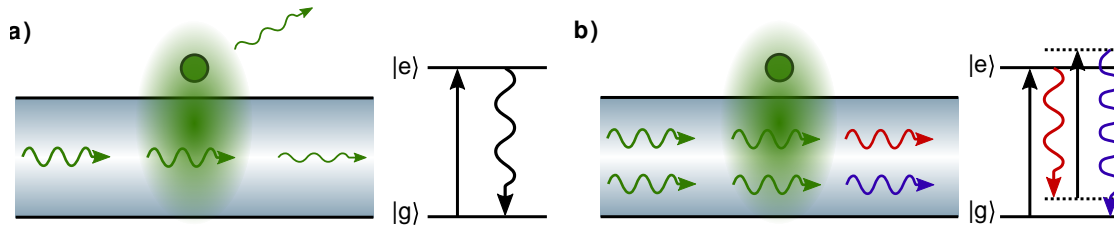


Figure 1.1: a) Interaction of single photons with an atom. The reduced amplitude of the arrows past interaction indicates that some photons are absorbed while others transmit. The photons belong to a guided mode of a nanofiber and interact with the atom via the evanescent field of that mode. b) Interaction of a pair of photons with an atom. If both photons interact within the lifetime of the excited state the process depicted in the level scheme can occur. The consequence are two energy-time entangled photons that are detuned with respect to the atomic transition.

non-classical light we examine the quadrature uncertainty of the output light and show that it exhibits squeezing.

1.2 Studying light with optical nanofibers

Our platform of choice to study light-matter interaction are tapered optical fibers with diameters below the wavelength of the guided light, called nanofibers [4]. Interest in this system arose because they allow to interface fiber guided light with an emitter via the evanescent field at the nanofiber waist without releasing the light from the guided mode. Moreover, they achieve a strong focussing effect throughout the entire waist whereas strongly focussed free space beams diverge rapidly away from the focal point. This makes nanofibers a promising component for future fiber networks. Another application is to use nanofibers to study light-matter interaction at the most fundamental level. Here, the possibility to interface laser-cooled atoms with a nanofiber has received increasing interest in recent years. While initial studies interfaced simply a Cesium vapour present at the nanofiber waist it was soon proposed to trap the atoms in the evanescent field [5, 6]. Indeed, only a few years later successful trapping was demonstrated [7]. Shortly after, another trap realisation was reported that utilised magic-wavelengths to reduce spectral broadening from the trap [8]. Since then, nanofiber based dipole traps have been developed into a versatile tools to study light-matter interaction. For example, nanofibers have been employed to demonstrate spin-momentum locking and thus contributed to the emergence of the field of chiral quantum optics [9–11]. This spin-momentum locking was employed to demonstrate an optical diode [12]. Storage of light was demonstrated, opening the perspective of a nanofiber-based quantum memory [13, 14]. To this end, the first step of the celebrated DLCZ protocol was realised on a nanofiber platform [15, 16]. It was reported, how the periodicity of the trap potential can lead to collective reflection from the trapped ensemble [17, 18]. The range of this selection of results illustrates the versatility of nanofibers for studying light-matter interaction.

1.3 Thesis structure overview

This thesis is structured as follows: The theoretical concepts of nanofiber-based atom trapping are presented in chapter 2. The guided modes are discussed and the principle of the evanescent field trap is explained. Chapter 3 provides the theoretical concepts to understand squeezed light and how it is generated from non-linear photon transport. Chapter 4 describes the construction of the experimental apparatus from empty tables to an operational light-matter interface. Lastly, chapter 5 presents the experimental observation of squeezed light from an ensemble of weakly coupled Cesium atoms and studies the squeezing dependence on power and detuning. Chapter 6 gives an outlook on possible future experiments.

Properties of ultra-thin optical fibers

Optical fibers with diameters below the wavelength of the guided light are at the heart of the experiments presented in this work. Such fibers have received increased attention in recent years because of their intriguing optical features such as spin-momentum locking of light, linking polarization and propagation direction, and azimuthal symmetry breaking of its guided modes. One field of applications consists of fundamental research in quantum optics such as interfacing of laser-cooled atoms and molecules sensing [7, 8, 19, 20]. This chapter introduces a description of the optical modes in sub-wavelength-diameter optical fibers and details the principle of a dipole trap for atoms in the evanescent field. Moreover, the vibrational modes of nanofibers are discussed and the manufacturing via a heat-and-pull technique is sketched.

2.1 Electric field and intensity distributions

Optical fibers are a common technology in the modern world, used for telecommunication and sensing in a great range of contexts. Usually, these fibers consist of a Fluorine or Germanium doped, few micrometer thick silica (SiO_2) core with a $60\mu\text{m}$ thick silica cladding. The doping increases the refractive index of silica by less than 1% such that light is confined to the core but its evanescent field reaches far into the cladding which is why we speak of weakly-guided modes. These are described well by linearly polarized (LP) modes which are approximated and superpositioned solutions of Maxwell's equations. The situation changes starkly for air-clad fibers with diameters on the order of the wavelength of the guided light. Here, the doped core has disappeared and the cladding turns into the core while the surrounding vacuum acts as cladding. For such small radii the approximations underlying the LP solutions become invalid. Instead, one has to return to the exact solutions of the fundamental linearly polarized HE modes (Hybrid Electric) which feature interesting properties for sub-wavelength-diameters:

- Strong evanescent field: A considerable part of the guided light propagates above the fiber surface in the evanescent field where it can be interfaced with emitters or optical components.

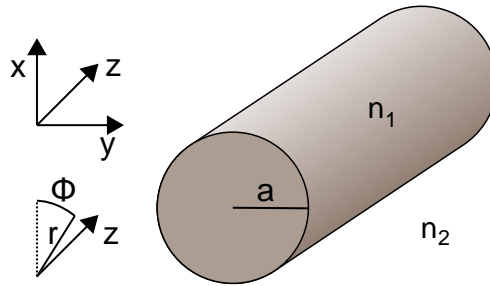


Figure 2.1: Fiber geometry and coordinate systems throughout this thesis. For air-clad nanofibers the contrast of the refractive indices $n_1 \sim 1.55$ and $n_2 = 1$ is large and the modes are strongly guided, unlike in weakly-guiding standard optical fibers with permille refractive index contrasts.

- **Broken symmetry in azimuthal direction:** Whereas the LP modes mentioned above exhibit intensity distributions that are rotationally symmetric about the fiber axis linearly polarized HE modes can exhibit strong intensity variations along the azimuthal direction, giving rise to a strong and weak axis of the mode.
- **Strong longitudinal electric field component:** The strong gradient of the evanescent field above the fiber surface gives rise to an electric field component in the direction of propagation. This component is $\pi/2$ out of phase with the major transverse electric field component such that elliptical polarization can be observed close to the fiber surface and lying in plane spanned by fiber and strong axis. Moreover, the sign of the relative phase and thus the orientation of the elliptical polarization is linked to the propagation direction, a feature that has attracted considerable attention recently under the banner of 'chiral quantum optics' [11].

A detailed derivation of the HE modes from Maxwell's equations is found in several texts, for example [21], here only the solution of the quasi-linearly polarized HE_{11} mode is given. The geometry of the problem is shown in Fig.2.1 where two coordinate systems used throughout this thesis are indicated. The symmetry of the fiber suggests the use of cylindrical coordinates and therefore the field solutions will be given in them. In the context of the experimental setup and for orientation of the mode axis cartesian coordinates can be more practical and will be used accordingly.

In cylindrical coordinates the complex valued electric field components of the HE_{11} mode inside the fiber, i.e. $r < a$, can be expressed as

$$E_x = -iA \frac{\beta}{2h} [(1-s)J_0(hr) \cos \phi_0 - (1+s)J_2(hr) \cos(2\phi - \phi_0)] e^{i(\omega t - \beta z)}, \quad (2.1)$$

$$E_y = -iA \frac{\beta}{2h} [(1-s)J_0(hr) \sin \phi_0 - (1+s)J_2(hr) \sin(2\phi - \phi_0)] e^{i(\omega t - \beta z)}, \quad (2.2)$$

$$E_z = AJ_1(hr) \cos(\phi - \phi_0) e^{i(\omega t - \beta z)}, \quad (2.3)$$

$$(2.4)$$

and outside the fiber ($r > a$) as

$$E_x = -iA \frac{\beta}{2q} \frac{J_1(ha)}{K_1(qa)} [(1-s)K_0(qr) \cos \phi_0 + (1+s)K_2(qr) \cos(2\phi - \phi_0)] e^{i(\omega t - \beta z)}, \quad (2.5)$$

$$E_y = -iA \frac{\beta}{2q} \frac{J_1(ha)}{K_1(qa)} [(1-s)K_0(qr) \sin \phi_0 + (1+s)K_2(qr) \sin(2\phi - \phi_0)] e^{i(\omega t - \beta z)}, \quad (2.6)$$

$$E_z = A \frac{J_1(ha)}{K_1(qa)} K_1(qr) \cos(\phi - \phi_0) e^{i(\omega t - \beta z)}, \quad (2.7)$$

with

$$s = [(qa)^{-2} + (ha)^{-2}] / [J_1'(ha)/haJ_1(ha) + K_1'(qa)/qaK_1(qa)], \quad (2.8)$$

where $h = \sqrt{n_1^2 k^2 - \beta^2}$ and $q = \sqrt{\beta^2 - n_2^2 k^2}$ characterize the fields inside and outside the fiber and J_n and K_n stand for the n -th order Bessel functions of the first kind and the modified Bessel functions of the second kind, respectively. The coefficient A relates to the power P in the mode via $A = \sqrt{8\mu_0\omega P/\pi a^2\beta}$. Here, J_1' and K_1' denote the first derivative of the respective functions. The angle ϕ_0 determines the orientation of the strong axis of the mode and $\phi_0 = 0$ and $\pi/2$ align it to the x and y axis, respectively. The propagation constant β is determined through the following eigenvalue equation

$$\begin{aligned} \frac{J_0(ha)}{haJ_1(ha)} = & -\frac{n_1^2 + n_2^2}{2n_1^2} \frac{K_1'(qa)}{qaK_1'(qa)} + \frac{1}{h^2 a^2} \\ & - \left(\left[\frac{n_1^2 + n_2^2}{2n_1^2} \frac{K_1'(qa)}{qaK_1'(qa)} \right]^2 + \frac{\beta}{n_1^2 k^2} \left(\frac{1}{q^2 a^2} + \frac{1}{h^2 a^2} \right)^2 \right). \end{aligned} \quad (2.9)$$

This parameter β is an effective refractive index for the propagating light and reflects that the field partly propagates in the fiber bulk ($n \approx 1.55$ for silica) and partly in the surrounding vacuum ($n = 1$), i.e. its value is between the two refractive indices.

In many instances the intensity of the electric field is required which can be calculated from the above expressions via

$$I = \frac{1}{2} \epsilon_0 c n (E_x^2 + E_y^2 + E_z^2), \quad (2.10)$$

where c is the speed of light, ϵ_0 is the electric permittivity of the vacuum, and n is the local refractive index.

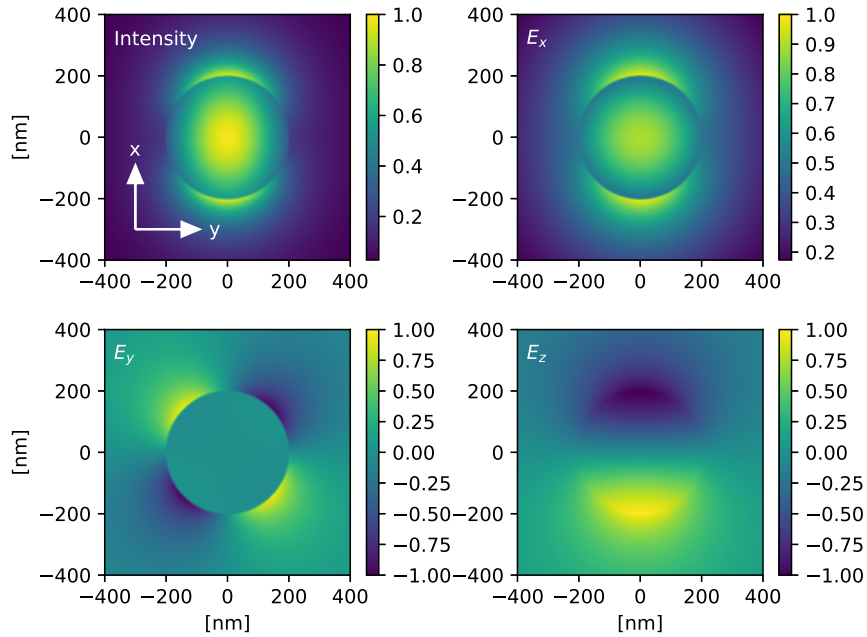


Figure 2.2: Spatial structure of the quasi-linearly polarized HE_{11} mode with the strong axis aligned along x . Shown are the intensity distribution (top left) and the real value of the spatial components, i.e. $\text{Re}(E_{x,y,z})$, normalised to the maximum value of the respective plot. The field energy is stored mostly in E_x and E_z while the field along the y -axis is approximately an order of magnitude weaker than the field along the x -axis. E_z is pointing in opposite direction above and below the fiber, which in combination with the $\pi/2$ -out of phase x -component results in elliptical polarizations with opposite orientations.

The strength of the total intensity and the respective field components of a mode with the strong axis aligned along y are shown in Fig. 2.2 where both the structure of the evanescent field and the breaking of azimuthal symmetry becomes apparent. Note that, in addition to the $\pi/2$ phase difference with respect to E_x , E_z has opposite phase above and below the fiber giving rise to counter-rotating elliptical polarizations in the respective regions. Moreover, the relative phase between E_x and E_z switches sign if the propagation direction is reversed which flips the orientation of the polarization ellipse. This has been labelled as spin-momentum locking or chirality [9, 11]. Note that the approximately exponential decay of the evanescent field in radial direction is wavelength dependent, with shorter wavelengths decaying more rapidly. This is the fundamental principle behind the evanescent field dipole trap, as will be illustrated in the next section.

2.2 Principle of nanofiber-based dipole trapping

Light fields can be used to trap neutral atoms: The force acting on the atoms originates from the fact that the oscillating electric field displaces the electrons from the atomic nucleus of an atom and induces an electric dipole. The potential energy of this dipole in the oscillating electric field is called the AC-Stark shift. Depending on the amplitude of the electric field it can become comparable to the kinetic energy of laser-cooled atoms and therefore it can form a trap potential for such atoms [22]. The potential energy of the induced dipole in the external field is given by

$$U = -1/2\langle \mathbf{d} \cdot \mathbf{E} \rangle, \quad (2.11)$$

where $\mathbf{d} = \alpha(\omega)\mathbf{E}$ is the induced dipole, \mathbf{E} is the external electric field, and the brackets indicate the time average. $\alpha(\omega)$ is the dynamical atomic polarizability. The induced dipole is in or π out of phase with the external electric field if the driving frequency is below or above the resonance frequency, respectively. The energy is lowered if the induced dipole is in phase with the drive field, i.e. \mathbf{d} and \mathbf{E} have the same sign, and raised if it is out of phase and \mathbf{d} and \mathbf{E} have opposite signs. This means that spatially varying laser fields form an attractive potential if their frequency is red detuned with respect to a nearby atomic transition because then the induced atomic dipole oscillates in phase with the driving field. Vice versa, for a blue detuned drive field the atomic dipole oscillates out of phase and raises its energy. Using the expression for the induced dipole we arrive at $U = -1/2\alpha(\omega)\mathbf{E}^2 \propto \alpha(\omega)I$, i.e. the potential is proportional to the light field intensity I . Thus a red detuned focused laser beam can act as a trap at the focal point and a blue detuned field can present a potential barrier. Such free space dipole traps have been used widely and with great success in many quantum optics experiments, for example as optical tweezers for single atoms [23–25] or as periodic potentials in optical lattices [26, 27]. More recently, dipole traps close to the surface of structures have received increased interest because they enable rich interactions between trapped atoms and the structure [6, 28, 29]. These include using the evanescent field of an optical nanofiber as an atomic dipole trap.

2.2.1 Atomic polarizability

The strength of the induced dipole is given by the frequency- and polarization-dependent atomic polarizability $\alpha(\omega)$ that relates the inducing field strength to the dipole strength via $\mathbf{d} = \alpha(\omega)\mathbf{E}$. The total polarizability α can be expressed via three terms, corresponding to the dynamical scalar, vector, and tensor polarizability which gives [30]

$$\alpha = \alpha_{nJF}^s - i\alpha_{nJF}^v \frac{[\mathbf{u}^* \times \mathbf{u}] \cdot \mathbf{F}}{2F} + \alpha_{nJF}^T \frac{3[(\mathbf{u}^* \cdot \mathbf{F})(\mathbf{u} \cdot \mathbf{F}) + (\mathbf{u} \cdot \mathbf{F})(\mathbf{u}^* \cdot \mathbf{F})] - 2\mathbf{F}^2}{2F(2F - 1)}, \quad (2.12)$$

where nJF denotes the atomic fine-structure level, \mathbf{u} is a complex unit vector pointing along the local electric field, \mathbf{u}^* denotes the complex conjugate, and \mathbf{F} is the total angular momentum operator of the atom. J is the total electron angular momentum and I is the nuclear angular momentum. The above notation is legitimate far off resonance where the Stark shift is small compared to the hyperfine-structure splitting and thus the level mixing of atomic states with different quantum numbers F can be neglected. This formula illustrates the dependence of

the total polarizability on the polarization of the light field which is examined more closely in Sec.2.4. The coefficients α_{nJF}^s , α_{nJF}^v , and α_{nJF}^T are calculated via [30]

$$\alpha_{nJF}^s = \alpha_{nJ}^s = \frac{1}{\sqrt{3(2J+1)}} \alpha_{nJ}^{(0)}, \quad (2.13)$$

$$\alpha_{nJF}^v = -\sqrt{\frac{2F(2F+1)}{F+1}} \begin{pmatrix} F & 1 & F \\ J & I & J \end{pmatrix} \alpha_{nJ}^{(1)}, \quad (2.14)$$

$$\alpha_{nJF}^T = -(-1)^{J+I+F} \sqrt{\frac{2F(2F-1)(2F+1)}{3(F+1)(2F+3)}} \begin{pmatrix} F & 2 & F \\ J & I & J \end{pmatrix} \alpha_{nJ}^{(2)}, \quad (2.15)$$

where α_{nJ}^K denotes the reduced dynamical polarizability where $K = 0, 1, 2$ corresponds to the scalar, vector, and tensor contributions. The reduced dynamical polarizability can be calculated from [30]

$$\begin{aligned} \alpha_{nJ}^{(K)} = & (-1)^{K+J+1} \sqrt{2K+1} \times \sum_{n',J'} (-1)^{J'} \begin{pmatrix} 1 & F & 1 \\ J & J' & J \end{pmatrix} |\langle n'J' | \mathbf{d} | nJ \rangle|^2 \\ & \times \frac{1}{\hbar} \text{Re} \left(\frac{1}{\omega_{n'J'nJ} - \omega - i\gamma_{n'J'nJ}/2} + \frac{(-1)^K}{\omega_{n'J'nJ} + \omega + i\gamma_{n'J'nJ}/2} \right), \end{aligned} \quad (2.16)$$

where $\begin{pmatrix} 1 & K & 1 \\ J & J' & J \end{pmatrix}$ is the $6j$ -Wigner symbol. The expression sums over all allowed transitions between the atomic fine-structure levels nJ and $n'J'$. The terms in the denominators correspond to the frequency of the respective transition, i.e. $\omega_{n'J'nJ} = \omega_{n'J'} - \omega_{nJ}$, and the transition linewidth $\gamma_{n'J'nJ}$. A collection of the reduced matrix elements $\langle n'J' | \mathbf{d} | nJ \rangle$ for Cesium is given in Ref. [30] and is the underlying data set for the dipole potential calculations presented here.

2.2.2 Trapping potentials

Trapping atoms in the evanescent field of a nanofiber was first proposed by LeKien *et al.* in 2004 [31] and realized for the first time in 2010 in our group [7]. The core idea relies on the wavelength-dependent decay of the evanescent field around a tapered optical fiber with sub-wavelength diameter. A blue-detuned and thus repulsive light field has a shorter wavelength than a red-detuned and thus attractive light field and consequently decays more rapidly in radial direction. Therefore, the combination of a repulsive and an attractive field can form a potential minimum above the fiber surface and thus confine atoms in the radial dimension. This is depicted in Fig.2.3a where the potential energy of the ^{133}Cs ground state is plotted as a function of distance to the fiber surface. The potential is calculated using the mode intensity calculated from the analytic solutions presented previously and the atomic polarizabilities following Ref. [32]. The y -axis has the unit of micro-Kelvin, obtained by normalizing the potential energy to the Boltzmann-constant, which is practical in order to compare trap depths and temperatures achieved through laser-cooling. Note the asymmetry of the trap in radial direction which has the consequence that atoms in higher vibrational trap levels are on average further away from

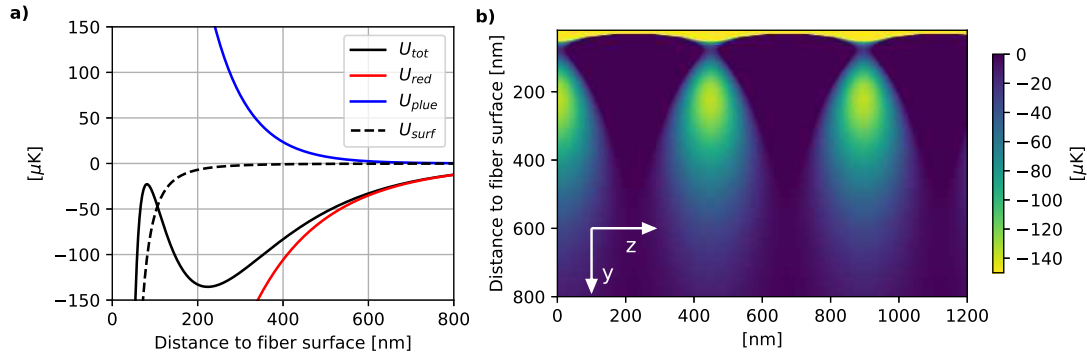


Figure 2.3: (a) Trapping potential as function of distance to the nanofiber surface for a fiber radius of 200 nm, created from the combination of two counter-propagating fields at 935 nm with $195 \mu\text{W}$ power each and field at 685 nm with 13 mW power. Close to the fiber surface attractive Van-der-Waals forces occur, modifying the dipole potential with U_{surf} [31]. (b) Trapping potential in the yz -plane, illustrating the confinement along z due to the red-detuned standing wave.

the fiber surface than atoms in lower vibrational states. This means that heating the atoms, by which we mean that their vibrational quantum number increases, leads to weaker coupling to fiber-guided probing fields which decay on similar length scales above the fiber surface as the trap fields. Both the red and the blue detuned trap field are quasi-linearly polarized with the blue trap polarization aligned orthogonally to the red trap polarization. In our trap configuration, the blue trap mode is polarised orthogonally to the trapping plane which is defined by the polarisation of the red trap mode. Therefore, the blue trap intensity increases in azimuthal direction away from the trap center, thus confining the movement of atoms in azimuthal direction. In addition, the intensity of the red trap field is at a maximum in azimuthal direction at the trap center, providing further confinement in this direction. Finally, 3D confinement can be achieved by counter-propagating red trap fields that form a standing wave. The result are two 1D arrays of micro-traps on opposite sides of the nanofiber, as depicted for one side of the nanofiber in Fig.2.3b where the potential energy in the y - z -plane is shown. Many different trap configurations are possible with different trap polarizations. We choose a linearly polarized trap configuration because linear polarization is easiest to realise experimentally. Moreover, it provides efficient coupling between the trapped atoms and a linearly polarised probe field due to its increased azimuthal confinement compared to trap configurations based on circular light. This can be understood as follows: Strongest coupling occurs generally when the probe field intensity at the position of the potential minimum is maximized. To this end the atom should be confined to the strong axis of the probe field as good as possible since the probe field intensity reduces for angles off the strong axis. Strongest azimuthal confinement is achieved via linearly polarised trap fields due to their azimuthal symmetry breaking.

In our experiment we accumulate atoms in a magneto-optical trap around the nanofiber and subsequently transfer them into an optical molasses where atoms experience friction as they

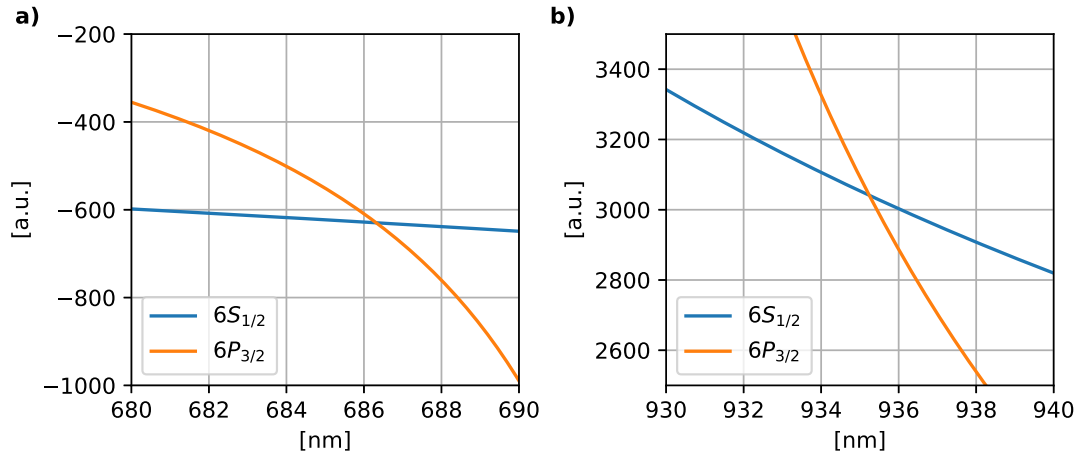


Figure 2.4: Scalar polarizabilities of the Cesium $S_{1/2}$ and the $6P_{3/2}$ manifolds in the range of the blue trap wavelength (a) and the red trap wavelength (b), given in atomic units. The magic wavelength occurs at the crossing of the blue and orange curves where ground and excited state experience the same shift, rendering the transition frequency significantly less dependent on trap field intensity. Data reproduced from [30].

move through space. When atoms are attracted towards a trap minimum they accelerate, converting potential energy into kinetic energy. The molasses cooling dissipates this energy such that they lack the kinetic energy to escape the trap. At the same time, the molasses gives rise to light-assisted collisions between two atoms in the same micro-trap which release enough kinetic energy to evict both atoms from the trap, commonly referred to as collisional blockade [33]. The consequence is that one micro-trap can hold either zero or one atoms and the average trap filling factor cannot exceed 0.5 unless more sophisticated schemes are employed, such as a gray molasses using blue detuned cooling light [34]. With our standard molasses cooling technique we typically trap arrays ranging from ten to hundreds of atoms along the nanofiber. Note that with molasses cooling the energy of the trapped atoms is still well described by a thermal ensemble, i.e. occupation of vibrational levels in the trap follows a Boltzmann distribution. Different cooling schemes for fiber-trapped atoms have been demonstrated to cool the atoms almost completely to the vibrational ground state but these were not implemented in our experiment [35,36].

2.2.3 Magic wavelength traps

Dipole traps rely on the energy shift of the atomic ground state energy in the presence of a light field detuned with respect to a dipole transition between the ground state and an excited state. This excited state energy is generally also shifted by the presence of the light field and therefore the transition frequency between ground and excited state can be shifted, too. The magnitude of the shift depends on the strength of the light field and if this light field has spatially varying intensity the transition frequency is also spatially varying. This is detrimental for an atom-light interface for the following reason: As a thermal ensemble the trapped atoms occupy a range

of different vibrational states which have different spatial extent. This means that overlap between the spatial wave-function of the atom and the trapping field depends on the vibrational state. This overlap determines the energy shift of the electronic ground and excited state. Generally, these states do not experience the same energy shift through the trap field. The consequence is that the transition frequency between electronic ground and excited state depends on the vibrational state. Considering the thermal occupation of vibrational states it becomes clear that this translates into a broadened absorption profile for the whole ensemble. But it is possible to reduce this broadening by ensuring that the excited state light shift is similar to the shift of the ground state. This is achieved by so called 'magic wavelengths' for which the electronic ground and excited state experience precisely the same scalar AC-stark shift, i.e. both states have the same value for $\alpha_{n,J}^s$, and their transition frequency is thus less affected by the trap fields [30]. Note that these magic-wavelengths still give rise to vector and tensor light shifts, i.e. $\alpha_{n,J}^v$ and $\alpha_{n,J}^T$ can still differ for ground and excited state. In our trap configuration, vector light shifts vanish since atoms at the trap minimum are exposed only to linear polarization. Generally, linearly polarised modes of a nanofiber can be elliptically polarised in the evanescent field due to the π -out of phase longitudinal electric field component. However, the spatial distribution of the longitudinal component, as depicted in Fig. 2.2, vanishes on the weak axis of the mode. In our trap configuration the trapping plane is along the weak axis of the blue trap field, therefore atoms are exposed to linearly polarised blue trap light at the trap minimum. This is different for the red trap field since its strong axis lies in the trapping plane. However, due to the counter-propagating red trap modes the longitudinal field component interfere destructively, leaving the red trap field linearly polarised at every position in the evanescent field. Therefore, atoms at the trap minimum are only exposed to linearly polarised trap light and experience vanishing vector light shifts since these exist only for elliptical and circular polarisation as is apparent from Eq. 2.12. Tensor light shifts, however, are still possible. These vanish for $J = 1/2$ and therefore the Cesium ground state is unaffected. But the excited state of our probing transition is energy shifted due to tensor light shift which we discuss later.

Besides reducing the spectral broadening of trapped atoms magic wavelengths also reduce heating from scattering because they present the same trapping potential to ground and excited state. More specifically, off-resonant absorption of a trap photon or excitation via a probe light field can excite the atom for a finite time in which its potential energy depends on the AC-stark shift of the excited state and which typically differs from the ground state light shift. Therefore, the atom experiences a different trap potential during the time spent in the excited state which effectively provides a momentum kick for the atom and thus increases its kinetic energy. The consequence is that the heating of an atom when scattering light from a probe field is increased. The benefits of magic-wavelengths are therefore twofold: reduced broadening of fiber trapped ensembles and reduced heating from probing the ensemble resonantly.

Magic-wavelengths exist for only some of the transitions of elements used in laser-cooling experiments. Fortunately, the $6S_{1/2} \rightarrow 6P_{3/2}$ transition in Cesium, referred to as the D2 line, features both a blue detuned magic wavelength at 685 nm and a red detuned magic wavelength at 935 nm which determines the wavelengths chosen for our experiment [30]. The scalar polarisability of the ground and excited state used in the probing schemes of this thesis are shown in Fig. 2.4, reproduced from [30]. The figure illustrates that the light shift change with wave-

length is modest compared to typical drifts of freely running diode lasers that are usually below 100 MHz which corresponds to 0.1 nm shift in wavelength at 935 nm and even less at 685 nm. Therefore, none of the trap lasers in our experiment require frequency stabilisation.

2.2.4 Tensor polarizability at the magic wavelengths

The tensor polarizability of the ground state is zero and thus has no effect on the trapping potential. However, the excited state tensor shift is finite. The dynamical tensor polarizability generally depends on the polarization of the trap field and the angular momentum of the atom, as is apparent from (2.12). From the complete expression for the atomic polarizability in Eq. (2.12) we see that the tensor light shift depends on the relative orientation of the atomic angular momentum \mathbf{F} and the complex polarization vector \mathbf{u} . The product of these two vectors therefore depends on the magnetic quantum number m_F that quantifies the z -component of the total angular momentum. In the following we estimate an upper boundary of this m_F -dependent energy shift. We assume a weak magnetic field along the z -direction that provides the quantization axis. Next we assume that the trap field is linearly polarised along this direction because this leads to the strongest energy shift. Then, the splitting of the excited state due to tensor light shifts is given by [30]

$$\Delta E = \frac{1}{4} |\mathcal{E}|^2 (1 - 3|u_z|^2) \alpha_{nJF}^T \frac{3m_F^2 - F(F+1)}{2F(2F-1)}, \quad (2.17)$$

where u_z is the z -component of the polarization vector, and \mathcal{E} is the electric field amplitude. In Fig. 2.5 we calculate this splitting using the tensor polarizabilities at the red and blue trap wavelength, assuming the field intensities at the center of the trap that result from the trap powers used in our experiment, i.e. $P_{\text{red}} = 195 \mu\text{W}$ and $P_{\text{blue}} = 13 \text{mW}$. Note that the center-of-mass of the splitting is zero, i.e. the average of the F -manifold is unshifted. The figure shows that the total tensor light shift of the excited state in our trap configuration can be on the order of a few MHz. Note that in our trap configuration these energy shifts cannot be added up because they originate from trap fields with orthogonal polarisation. Generally, the outermost m_F states that are the excited state of the cycling transition are most energy shifted due to tensor light shifts. This means that the cycling transition frequency depends on the trap field intensity and thus changes for different positions of an atom in the trap.

2.3 Mechanical properties

The extremely small diameter of nanofibers not only leads to interesting optical properties but also entails mechanical aspects. A nanofiber with a diameter of half a micrometer and a waist length of a few millimeters is a glass cylinder with extreme aspect ratio and can vibrate in several modes that can be grouped into three classes:

- Torsional modes: The fiber is displaced in azimuthal direction with fixed points at the tapers.
- Transverse modes / Flexural modes: The fiber is displaced transverse to its axis, similar to a guitar string.

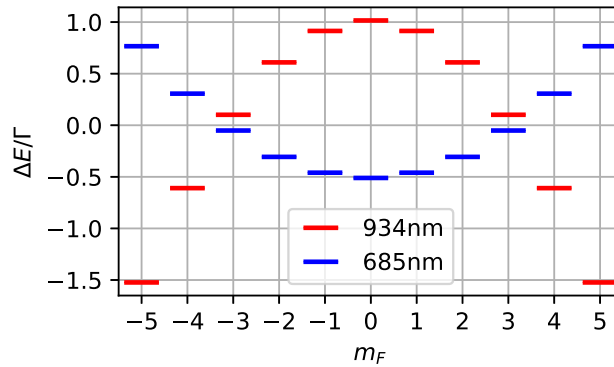


Figure 2.5: Upper boundary of the energy shift for different m_F states due to the tensor light shift in our trap configuration, using orthogonally linearly polarised trap fields with $P_{\text{red}} = 195 \mu\text{W}$ and $P_{\text{blue}} = 13 \text{ mW}$. Energy shifts are normalised to the D2-transition linewidth of $\Gamma = 5.2 \text{ MHz}$.

- Longitudinal modes: The fiber is displaced along its axis with a very small displacement in radial direction.

Among these, torsional modes have received increased attention as they initially seemed a promising explanation for the strong heating observed in nanofiber-based dipole traps. For a nanofiber with a 10 μm waist the fundamental torsional mode, where $\lambda/2$ is equal to the waist length, has a frequency of $\sim 90 \text{ kHz}$. Note that this does not depend on longitudinal strain of the fiber but is determined entirely by the waist length, fiber radius and the material stiffness. Azimuthal strain induces circular birefringence in the fiber waist such that circularly polarized optical modes experience different refractive indices depending on the light's handedness. This also affects linearly polarized modes which can be understood as follows: Linearly polarized modes can be described as a superposition of the two orthogonal circular polarizations. The relative phases of these modes shift due to circular birefringence and the result is a tilt of the linearly polarized mode's axis. Thus, the orientation of the linearly polarized modes can vibrate at the frequency of the torsional modes. Recently, however, more in depth analysis of the mechanical spectrum of nanofibers suggest that flexural modes provide a better explanation of the heating in nanofiber traps and that heating contributions from other vibration modes are small [37].

In practice, we found that transverse modes can have fundamental frequencies as low as a few hundred Hertz which means they can be excited by acoustic noise in the lab. Driving these modes acoustically via a function generator and a speaker reliably reduced the number of trapped atoms but no systematic study was carried out and it remained unclear whether this was due to poor atom loading or due to increased heating. Similarly, vibrations on the optical table can excite fiber vibrations resulting in poor atom trapping until the induced vibrations have decayed.

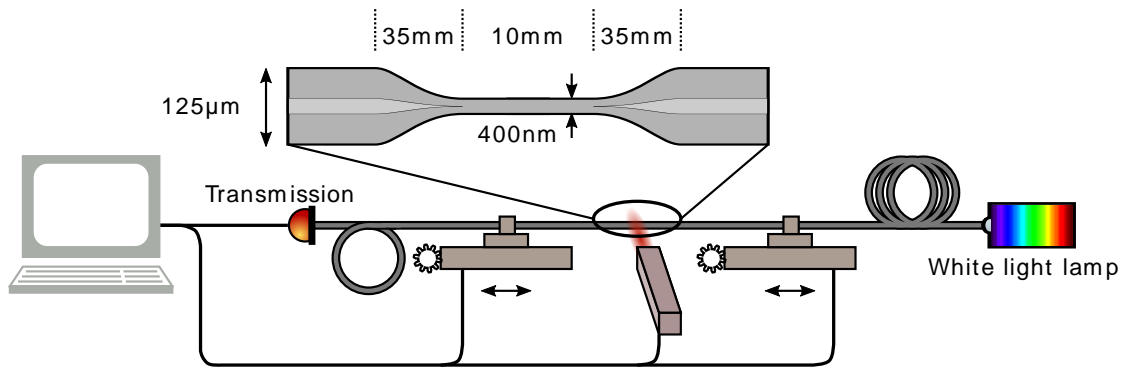


Figure 2.6: Schematic depiction of the pulling rig with magnified view of the tapered fiber. A control computer steers translation stages while monitoring spectral transmission through the fiber. The taper sections are optimized for minimum losses while keeping them as short as possible. The lengths indicated on the fiber are typical values and can be altered, in particular the waist can be up to 35 mm long in the pulling rig of our group.

Vibrational nanofiber modes can be excited thermally and thus their elimination is difficult. This is especially true since the optical fields required for evanescent field dipole trapping, with powers on the order of milli-Watt, can heat the fiber to considerable temperatures of more than 1000 K which was observed experimentally in a dedicated setup in our group [38]. This can be detrimental for the lifetime of the atom ensemble in the trap, discussed in more detail in the experimental trap characterization in Sec.4.6.

2.4 Manufacturing of ultra-thin optical fibers

Ultra-thin optical fibers can be obtained from commercially available optical fibers via a controlled heat and pull process. To this end our group operates two pulling rigs where a highly pure 2 : 1 mixture of hydrogen and oxygen is burned, leading to a very clean flame that heats the fiber locally. A schematic overview of the pulling rig is given in Fig.2.6. The fiber is mounted on translation stages that move it through the flame at a controlled speed and with a well defined time profile while gradually stretching the fiber causing it to taper at the heated spot. This has enabled the precise and reproducible pulling of pre-defined radius profiles and thus to optimize the transmission of the taper section where the fiber modes are transformed adiabatically from the weakly guided modes in the standard optical fiber section to the ultra-thin fiber waist. Careful calibration and design of the pulling rig and the pulling sequence has enabled our group to pull nanofibers with transmission of more than 99% across a broad range of wavelengths and typically in the near-infrared. A more detailed account of the pulling rig is given in [39].

The nanofibers used in the experiments presented in this work are commercially available SM800 fibers (Fibercore, SM800) that were selected to still act as single-mode fibers at a wavelength of 685 nm, that is we specifically requested fiber from a badge with the cut-off wavelength below this value. Such fibers can be available due to the large variations in the fiber manufactur-

ing process.

2.5 Summary

The tapered optical fibers described in this chapter form the heart of the experiments in this thesis. We described their guided modes and showed their electric field distributions. The principle of dipole trapping was reviewed and the potential of the evanescent field dipole trap above the nanofiber surface was shown. The concept of magic-wavelengths was introduced and we showed that the scalar AC-stark shift is the same for ground and excited state at the trapping wavelengths of 685 nm and 935 nm. Although the ground state experiences no tensor light shift the transition frequency can shift since the excited state is energetically shifted due to tensor light shifts for which we presented an upper boundary to estimate their magnitude. Finally, we reviewed mechanical properties of optical nanofibers and described the process of nanofiber pulling.



Die approbierte gedruckte Originalversion dieser Dissertation ist an der TU Wien Bibliothek verfügbar.
The approved original version of this doctoral thesis is available in print at TU Wien Bibliothek.

Squeezed light from non-linear photon transport

The experiments reported in this work study how resonant interaction of coherent light with an ensemble of atoms leads to non-classical states of light. This chapter touches on the relevant theoretical concepts to interpret the measurements. In the first half, the fundamental description of light is presented, connecting the seemingly contradictory pictures of light as a particle and as a wave. In particular, the framework is developed to understand why this wave has uncertainty in its amplitude and that this uncertainty can be modified within the Heisenberg uncertainty principle. The second half of the chapter reviews a theoretical framework published recently by Mahmoodian et al. [40] that describes non-linear photon transport by means of scattering matrices. Specifically, correlated photon pairs emerge, transforming the weak, coherent input state of light into squeezed light with a characteristic spectrum. But before discussing these atom-induced photon correlations we go back one step and consider just photons on their own.

3.1 Squeezed light

Describing light at the most fundamental level can be complicated: It should explain experiments that clearly suggest a particle nature of light but it should also explain experiments that suggest the opposite interpretation of a wave nature. The quantum optics community tends to think in the particle picture because this is intuitive when we think of a single photon interacting with a single atom or another single photon entangled with its counterpart. But in our macroscopic world this particle nature is barely observable. Here, we think of an electro-magnetic wave that interferes and therefore has a well-defined phase. Since there is only one version of physics there must be a link between these two descriptions. And indeed, previous generations of physicists have built an excellent framework that is consistent with both pictures. The experiments in this thesis are in fact linking these two aspects, at least in our view of photon pair interaction (particles) that lead to squeezed light (wave). This chapter introduces the formalism that connects these two worlds

and points at the relevant observables for our experiment. The reviewed theory of squeezed light is mostly based on the book by Gerry and Knight [41] while the non-linear transport section essentially reviews the study by Mahmoodian et al. [40].

3.1.1 Number states, coherent states, electric field

We start on the particle side and with the very basic picture of a harmonic oscillator that accommodates anywhere from zero to infinite excitations. Such an excitation is called a photon. Its energy oscillates between the electric and magnetic field since according to Maxwell's equations the change of one causes the other. In the case of zero excitations we have the vacuum state and denote it by $|0\rangle$. Formally, an excitation enters and exits the world via the creation and annihilation operators that act on a harmonic oscillator with n excitations via

$$\hat{a}^\dagger |n\rangle = \sqrt{n+1} |n+1\rangle \quad (3.1)$$

$$\hat{a} |n\rangle = \sqrt{n} |n-1\rangle \quad (3.2)$$

These states $|n\rangle$ are called *number states* or *Fock states* and generally look like

$$|n\rangle = \frac{(\hat{a}^\dagger)^n}{\sqrt{n!}} |0\rangle \quad (3.3)$$

Since they are eigenstates of the the harmonic oscillator they are static, much unlike the oscillating electric field that we need to describe. However, the phases of different eigen-states of a harmonic oscillator evolve at different frequencies. A superposition of harmonic oscillator states can therefore lead to oscillating amplitudes. This insight lead Roy Glauber to introduce the *coherent state* [42]. These states are characterized by a complex amplitude α and have the form

$$|\alpha\rangle = e^{-|\alpha|^2/2} \sum_{n=0}^{\infty} \frac{\alpha^n}{\sqrt{n!}} |n\rangle \quad (3.4)$$

It is common and practical to express α in a polar form as $\alpha = |\alpha|e^{i\theta}$. The creation and annihilation operators are eigen-operators and we find $\hat{a} |\alpha\rangle = \alpha |\alpha\rangle$ and $\langle\alpha| \hat{a}^\dagger = \langle\alpha| \alpha^*$. Next, we define an electric field operator as

$$\hat{E}(t) = i\sqrt{\frac{\hbar\omega}{2\epsilon_0 V}} (\hat{a}_k e^{-i\omega_k t} - \hat{a}_k^\dagger e^{i\omega_k t}), \quad (3.5)$$

with the wavenumber $k = 2\pi/\lambda$. The prefactor can be interpreted as the electric field of a single photon with energy $\hbar\omega_k$. The expectation value of this operator acting on a coherent state is then

$$\langle\alpha| \hat{E} |\alpha\rangle = i\sqrt{\frac{\hbar\omega_k}{2\epsilon_0 V}} (\alpha e^{-i\omega_k t} - \alpha^* e^{i\omega_k t}) \quad (3.6)$$

and using the polar form of α we get

$$\langle E \rangle_\alpha = 2|\alpha| \sqrt{\frac{\hbar\omega_k}{2\epsilon_0 V}} \sin(\omega_k t - \theta) \quad (3.7)$$

So the electric field expectation value for a coherent state is indeed oscillating like we know it from the classical world. In contrast, for a Fock state we find $\langle n | \hat{E} | n \rangle = 0$. This illustrates the usefulness of coherent states to consistently connect the quantum world to the classical world. The vanishing electric field expectation value also shows that Fock states are very non-classical. They have a well defined energy but this energy is only noise, that is

$$(\Delta E)^2 = \frac{\hbar\omega_k}{2\epsilon_0 V} (2n + 1) \quad (3.8)$$

We can also calculate $\langle \alpha | \hat{E}^2 | \alpha \rangle$ and find for the variance of \hat{E}

$$(\Delta E)^2 = \langle \hat{E}^2 \rangle - \langle \hat{E} \rangle^2 = \frac{\hbar\omega_k}{2\epsilon_0 V}. \quad (3.9)$$

This is an important result because it shows that the electric field of a coherent state has uncertainty but it does not depend on α . This also means it does not depend on the phase θ , i.e. any phase of the electric field has the same noise.

Before we continue with we change the formalism slightly to stick to common theoretical frameworks.

3.1.2 Quadratures

We introduce the quadrature operators as

$$\hat{X}_1 = \hat{a} + \hat{a}^\dagger \quad (3.10)$$

$$\hat{X}_2 = i(\hat{a} - \hat{a}^\dagger) \quad (3.11)$$

They look similar to the electric field operator and indeed we can interpret \hat{X}_1 as the electric field at phase $\theta = \pi/2$ and \hat{X}_2 as the field at phase $\theta = 0$.

Another interpretation is that \hat{X}_1 describes the electric and \hat{X}_2 the magnetic field. Therefore, it is not surprising that the Hamiltonian of the harmonic oscillator from the beginning of the chapter expressed via quadratures has the form

$$\hat{H} = \frac{\hbar\omega}{4} (\hat{X}_1^2 + \hat{X}_2^2) \quad (3.12)$$

and that they satisfy the uncertainty relation

$$(\Delta \hat{X}_1)^2 (\Delta \hat{X}_2)^2 \geq 1. \quad (3.13)$$

It is also common to express the quadratures in an angle-dependent form as

$$\hat{X}_\theta = \hat{a} e^{-i\theta} + \hat{a}^\dagger e^{i\theta}, \quad (3.14)$$

such that $\hat{X}_{\theta=0} = \hat{X}_1$ and $\hat{X}_{\theta=\pi/2} = \hat{X}_2$. These will be used in the chapter reporting on experimental observation of squeezing. For the discussion in this chapter we stick to \hat{X}_1 and \hat{X}_2 . The uncertainty relation originates from the fact that \hat{X}_1 and \hat{X}_2 do not commute, i.e.

we have $[\hat{X}_1, \hat{X}_2] = 2i$, just like position and momentum do not commute in the quantum-mechanical description of the mechanical harmonic oscillator. Note that the right hand side of the inequality is a consequence of our definition of \hat{X}_1 and \hat{X}_2 . Some authors preface the quadrature operators with $1/\sqrt{2}$ and then the right hand side becomes $1/4$. Also note that another form of expressing the above Hamiltonian is $\hat{H} = \hbar\omega(\hat{n} + 1/2)$ where $\hat{n} = \hat{a}^\dagger\hat{a}$ is the number operator with $\hat{n}|n\rangle = n|n\rangle$, i.e. it relates back to the initial picture of this section of a harmonic oscillator with n excitations. Interestingly, the above uncertainty relation holds with equality for coherent states and the vacuum state. The coherent state and the vacuum state have the same, minimum quadrature uncertainty. Just like in the calculation of the electric field variance, $\Delta\hat{X}_{1,2}$ are independent of the coherent state phase θ . More precisely, with our definitions of quadratures, we find $(\Delta X_1)^2 = (\Delta X_2)^2 = 1$ for a coherent state. There are, however, states where this is not the case, treated in the following section.

3.1.3 Squeezed vacuum

Squeezed light, or more specifically, quadrature squeezed light describes the situation where the electric field variance is not constant with respect to phase and even falls below the vacuum variance that, as mentioned above, is the same as the variance of a coherent state. This is achieved by exceeding the vacuum variance at other phases, i.e. the other (conjugate) quadrature, such that the the inequality of (3.13) still holds.

We start the discussion of squeezed states by formally introducing a squeezing operator that generates a squeezed state from a coherent state. The strength of squeezing is characterized by the complex number $\epsilon = r e^{i\phi}$ and the operator has the form

$$\hat{S}(\epsilon) = \exp\left(\frac{1}{2}\epsilon^*\hat{a}^2 - \frac{1}{2}\epsilon(\hat{a}^\dagger)^2\right). \quad (3.15)$$

For the squeezing parameter r we have $0 \leq r < \infty$. The angle ϕ indicates that the squeezing has its own angle and determines how the squeezing is distributed between the two quadratures. The shape of the squeezing operator is already very instructive because it features \hat{a}^2 , i.e. the creation and destruction of photon pairs. Therefore, some authors describe it as a two-photon displacement operator [41]. In fact, an outdated term for squeezed light is *two-photon coherent states* [43]. This is a hint that squeezed vacuum is related to photon-pairs and more generally to the photon parity of a state, i.e. its composition from odd and even number states.

We illustrate this by applying weak squeezing to the vacuum. Weak squeezing, i.e. $r \ll 1$ means that we can approximate $e^x \approx 1 + x$ and the weakly squeezed vacuum, denoted $|\epsilon\rangle$, approximates

$$\hat{S}(\epsilon)|0\rangle \approx \left[1 + \frac{1}{2}\epsilon^*\hat{a}^2 - \frac{1}{2}\epsilon(\hat{a}^\dagger)^2\right]|0\rangle = |0\rangle - \frac{\epsilon}{\sqrt{2}}|2\rangle = |\epsilon\rangle. \quad (3.16)$$

We calculate the quadrature variance $(\Delta X)^2 = \langle X^2 \rangle - \langle X \rangle^2$ for the squeezed vacuum and

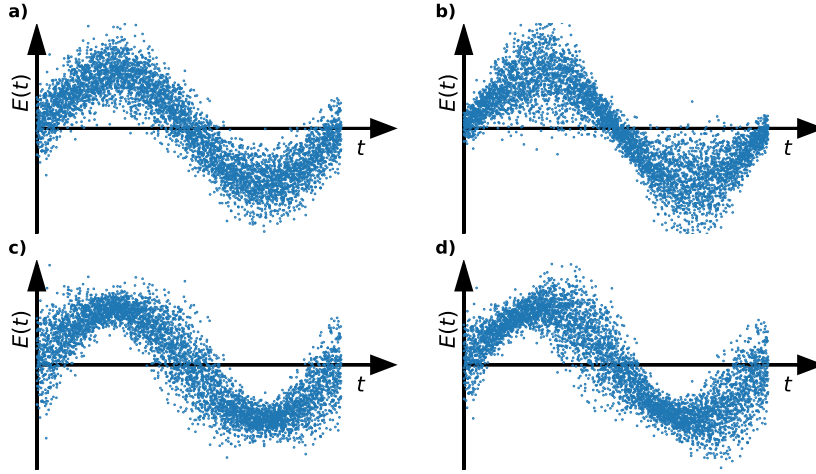


Figure 3.1: Electric field evolution for different states. a) a coherent state has the same electric field uncertainty at any phase. b) A phase squeezed state is obtained through application of the squeezing operator to a coherent state, such that $\theta - \phi = \pi/2$. It has minimum uncertainty in \hat{X}_2 , i.e. at the zero-crossing of the electric field, and vice versa maximum uncertainty when the field amplitude is maximum. c) Amplitude squeezed states are obtained for $\theta - \phi = 0$ and have the lowest field uncertainty for maximum electric field. d) Squeezed states can exist for any $0 \leq \phi \leq 2\pi$. The plot shows minimum electric field uncertainty for $0.7\pi/2$ und maximum uncertainty for $0.7\pi/2 + \pi$

obtain

$$(\Delta \hat{X}_1)^2 = 1 - \frac{5}{\sqrt{2}}\epsilon = 1 - \frac{5}{\sqrt{2}}re^{i\phi} \quad (3.17)$$

$$(\Delta \hat{X}_2)^2 = 1 + \frac{5}{\sqrt{2}}\epsilon = 1 + \frac{5}{\sqrt{2}}re^{i\phi} \quad (3.18)$$

So the squeezing operator has affected the uncertainty of the vacuum variance. For $\phi = 0$ we arrive at $(\Delta \hat{X}_1)^2 < 1$ and we call this *amplitude squeezing*. It means that the electric field amplitude at $\theta = \pi/2$ is less noisy than in a coherent state. This is afforded at the expense of a more noisy electric field field or, to relate to our formalism, a more noisy $(\Delta \hat{X}_2)^2$, at $\theta = 0$. A reduced uncertainty $(\Delta \hat{X}_2)^2$ is called *phase squeezing*. Note that generally ϕ can be anywhere between 0 and 2π , leading to the rotated quadrature operators $\hat{Y}_1 = \hat{a}e^{-i\phi} + \hat{a}^\dagger e^{i\phi}$ and $\hat{Y}_2 = i(\hat{a}^\dagger e^{i\phi} - \hat{a}e^{-i\phi})$. Electric field evolutions with different noise amplitudes at different phases are illustrated in Fig.3.1 to provide physical intuition for the consequences of squeezing. A deeper analysis of squeezed states will be given later in this chapter. For simplicity, we assume $\phi = 0$ in the following.

Note that applying the squeezing operator to the vacuum in fact adds photons to the vacuum, i.e. the term vacuum becomes a bit misleading but it has become common throughout the

literature nevertheless. One can make sense of it though by noting that, although it has finite, above-vacuum energy, the electric field expectazio value is zero.

3.1.4 Phase-space portraits

The states of light described here can be visualized well if we plot the two quadratures against each other together with their uncertainty, as shown in Fig.3.2. The vacuum state (red circle) is at the origin and shows finite and equal uncertainty in both quadratures. The displacement operator creates a coherent state from the vacuum (blue circle) which has the same uncertainty as the vacuum state. Squeezed vacuum (green) ellipse, has reduced uncertainty in one quadrature at the expense of the other quadrature and is obtained by applying the squeezing operator to the vacuum state. Note that this depiction assumes $\phi = 0$ for the squeezing operator. For different values of ϕ we obtain a rotated ellipse. If we apply both the squeezing and the displacement operator we arrive at a bright squeezed state (pink ellipse). The pink ellipse is reproduced for a finite angle θ as it appears in $\alpha = |\alpha|e^{i\theta}$ to illustrate that the states rotate about this origin with optical frequency.

In a homodyne detection measurement we measure the projection of the ellipses onto an axis, for example the X_1 -axis. Thus, the pink state will exhibit minimum fluctuations at $\theta = 0, \pi$ and maximum fluctuations at $\theta = \pm\pi/2$. Again, this is because we assume squeezing with $\phi = 0$ but the periodicity of the fluctuations holds for any value. Generally, the variance is modulated proportional to $\cos(2\theta)$.

3.1.5 Bright squeezed states

Next, we expand the initial squeezing analysis to the general case of arbitrary squeezing strength and to coherent states, following [41]. To this end we introduce the displacement operator $\hat{D}(\alpha)$, given by

$$D(\alpha) = \exp\left(\alpha^* \hat{a} + \alpha \hat{a}^\dagger\right), \quad (3.19)$$

which satisfies $|\alpha\rangle = D(\alpha)|0\rangle$ contributes to a bright squeezed state $|\alpha, \epsilon\rangle = \hat{D}(\alpha)\hat{S}(\epsilon)|0\rangle$. To calculate this, we will use the Baker-Campbell-Hausdorff lemma that, applied in our context, states

$$\hat{S}^\dagger(\epsilon)\hat{a}\hat{S}(\epsilon) = \hat{a} \cosh r - \hat{a}^\dagger e^{i\phi} \sinh r \quad (3.20)$$

$$\hat{S}^\dagger(\epsilon)\hat{a}^\dagger\hat{S}(\epsilon) = \hat{a}^\dagger \cosh r - \hat{a} e^{-i\phi} \sinh r \quad (3.21)$$

with $\hat{S}^\dagger(\epsilon) = \hat{S}(-\epsilon)$. Similarly, for the displacement operator we find

$$\hat{D}^\dagger(\alpha)\hat{a}\hat{D}(\alpha) = \hat{a} + \alpha \quad (3.22)$$

$$\hat{D}^\dagger(\alpha)\hat{a}^\dagger\hat{D}(\alpha) = \hat{a}^\dagger + \alpha \quad (3.23)$$

Equipped with these relations we consider the vacuum state $|0\rangle$ that satisfies

$$\hat{a}|0\rangle = 0, \quad (3.24)$$

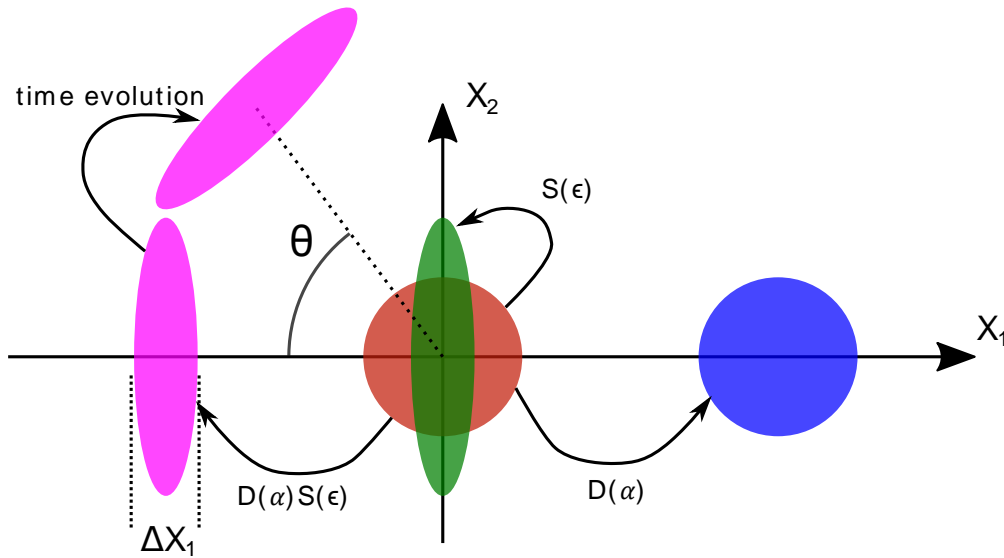


Figure 3.2: Uncertainty plots for various states of light. The red circle corresponds to the vacuum state $|0\rangle$. By applying the squeezing operator onto the vacuum state we obtain squeezed vacuum (red ellipse). Applying the displacement operator to the vacuum state gives a coherent state (blue circle), whereas applying it to the squeezed vacuum gives a bright squeezed state (pink ellipse). The angled ellipse illustrates that the ellipse rotates about the origin, captured in the complex coherent state amplitude $\alpha = |\alpha|e^{i\theta}$. In homodyne detection we measure the projection of the ellipse onto the x -axis and therefore observe a modulation of the variance proportional to $\cos 2\theta$ for squeezed states.

i.e. the vacuum state is an eigenvector of the lowering operator with eigenvalue 0. We apply the squeezing operator from the left and, using its unitarity, insert the factor 1 to obtain

$$\hat{S}(\epsilon)\hat{a}\hat{S}^\dagger(\epsilon)\hat{S}(\epsilon)|0\rangle = 0 \quad (3.25)$$

which is equivalent to

$$\hat{S}(\epsilon)\hat{a}\hat{S}^\dagger(\epsilon)|\epsilon\rangle = 0 \quad (3.26)$$

Now we can make the same eigenvector argument and state that the squeezed vacuum state is an eigenvector of the operator $\hat{S}(\epsilon)\hat{a}\hat{S}^\dagger(\epsilon)$. Using Baker-Hausdorff we can write this as

$$(\hat{a}\mu + \hat{a}^\dagger\nu)|\epsilon\rangle = 0 \quad (3.27)$$

where $\mu = \cosh r$ and $\nu = e^{i\theta} \sinh r$. Similarly, we can approach the bright squeezed state $|\alpha, \epsilon\rangle$ by writing

$$\hat{D}(\alpha)\hat{S}(\epsilon)\hat{a}\hat{S}^\dagger(\epsilon)\hat{D}^\dagger(\alpha)\hat{D}(\alpha)\hat{S}(\epsilon)|0\rangle = 0. \quad (3.28)$$

In successive steps we apply the Baker-Campbell-Hausdorff lemma for the squeezing and the displacement operator, recall $\hat{D}(\alpha)\hat{S}(\epsilon)|0\rangle = |\alpha, \epsilon\rangle$, and after rearranging we obtain another eigenvalue equation

$$(\hat{a}\mu + \hat{a}^\dagger\nu)|\alpha, \epsilon\rangle = \gamma|\alpha, \epsilon\rangle \quad (3.29)$$

with $\gamma = \alpha \cosh r + \alpha e^{i\theta} \sinh r$, and μ and ν as above.

These calculations can be utilized to analyse these arbitrarily squeezed states in the Fock basis. First, we consider the squeezed vacuum, which we want to describe via

$$|\epsilon\rangle = \sum_{n=0}^{\infty} C_n |n\rangle \quad (3.30)$$

Using the eigen-value equation given in Eq.(3.27), or the general eigenvalue equation in Eq.(3.29) with $\alpha = 0$, one can extract the recursive relation [41]

$$C_{n+1} = -\frac{\nu}{\mu} \sqrt{\frac{n}{n+1}} C_{n-1} \quad (3.31)$$

This relation leads to two distinct solutions because it connects only odd n or only even n . We are interested in the even solution because otherwise the vacuum state is not included. Then, the solution of the recursion relation is

$$C_{2m} = (-1)^m (e^{i\phi} \tanh r)^m \sqrt{\frac{(2m-1)!!}{(2m)!!}} C_0 \quad (3.32)$$

Through normalization and use of a mathematical identity one can obtain $C_0 = \sqrt{\cosh r}$ [41]. Using further identities the coefficients can be expressed as

$$C_{2m} = (-1)^m \frac{\sqrt{(2m)!}}{2^m m!} \frac{(e^{i\phi} \tanh r)^m}{\sqrt{\cosh r}} \quad (3.33)$$

Therefore, the squeezed vacuum written in the Fock basis is given by

$$|\epsilon\rangle = \frac{1}{\sqrt{\cosh r}} \sum_{n=0}^{\infty} (-1)^m \frac{\sqrt{(2m)!}}{2^m m!} (e^{i\phi} \tanh r)^m |2m\rangle \quad (3.34)$$

The probability of detecting $2m$ photons is

$$P_{2m} = |\langle 2m|\epsilon\rangle|^2 = \frac{(2m)!}{2^{2m} (m!)^2} \frac{(\tanh r)^{2m}}{\cosh r} \quad (3.35)$$

and for detecting an odd photon number we have $P_{2m+1} = 0$. These probabilities are shown in Fig.3.3a for two different strengths of squeezing, that is $r = 0.3$ and 1 . Only the Fock states with even photon number are populated and their population increases with squeezing strength.

Next we treat the effect of squeezing on coherent states, i.e. $\hat{D}(\alpha)\hat{S}(\epsilon)|0\rangle = |\alpha, \epsilon\rangle$. The strategy is the same as for the vacuum but the calculation a bit more involved. Starting with the general eigenvalue equation Eq.3.29 one can make the Ansatz [41]

$$C_n = \mathfrak{N} \sqrt{\cosh r} \left[\frac{1}{2} e^{i\phi} \tanh r \right]^{n/2} f_n(x) \quad (3.36)$$

with the normalization factor \mathfrak{N} and the initially unknown function $f_n(x)$. Substituting this expression into the eigenvalue equation we obtain the recursion relation

$$\sqrt{n+1}f_{n+1}(x) - 2\gamma\sqrt{e^{i\phi}\sinh(2r)}f_n(x) + s\sqrt{n}f_{n-1}(x) = 0 \quad (3.37)$$

where $\gamma = \alpha \cosh r + \alpha^* e^{i\phi} \sinh r$. This can be solved using the recursion relation for the Hermite polynomials H_n and we obtain $f_n(x) = H_n(x)/\sqrt{n!}$ with $x = \gamma(e^{i\phi} \sinh(2r))$. For the Fock state coefficients we thus get

$$C_n = \mathfrak{N}\sqrt{n! \cosh r} \left[\frac{1}{2} e^{i\phi} \tanh r \right]^{n/2} H_n(x) \quad (3.38)$$

Again, \mathfrak{N} is obtained from normalization and one finds [41]

$$\mathfrak{N} = \exp \left[-\frac{1}{2} |\alpha|^2 - \frac{1}{2} \alpha^{*2} e^{i\phi} \tanh r \right]. \quad (3.39)$$

Now we can express the squeezed bright state in the number basis as

$$|\alpha, \epsilon\rangle = \frac{1}{\sqrt{\cosh r}} \exp \left[-\frac{1}{2} |\alpha|^2 - \frac{1}{2} \alpha^{*2} e^{i\phi} \tanh r \right] \times \sum_{n=0}^{\infty} \frac{\left[\frac{1}{2} e^{i\phi} \tanh r \right]^{n/2}}{\sqrt{n!}} H_n \left[\gamma / \sqrt{e^{i\phi} \sinh(2r)} \right] |n\rangle. \quad (3.40)$$

Finally, the probability to detect n photons is given by

$$P_n = |\langle n | \alpha, \epsilon \rangle|^2 = \frac{\left(\frac{1}{2} \tanh r \right)^n}{n! \cosh r} \exp \left[-|\alpha|^2 - \frac{1}{2} (\alpha^{*2} e^{i\phi} + \alpha^2 e^{-i\phi}) \tanh r \right] \times |H_n \left[\gamma / \sqrt{e^{i\phi} \sinh(2r)} \right]|^2 \quad (3.41)$$

To develop a better understanding of this formula we plot it in Fig.3.3b and c for two different values of r and the same amplitude and angle of α . The angle is chosen such that α is fully real. Both plots have $\phi = 0$, i.e. the state is only squeezed along one quadrature. For weak squeezing the photon number distribution looks similar to that of a coherent state with small modifications at high n . These stem from the photon pairs introduced by the squeezing operator. For stronger squeezing (Fig.3.3c) these added photons become more pronounced. This is also apparent from the highest probability in the two plots that is lowered by a factor of two in the case of strong squeezing to accommodate population at higher n . The development of the spectrum of P_n due to different squeezing operators with increasing r is plotted in more detail in the appendix A.1. Note that the brightness, i.e. the average number of photons detected per time, is the same in both plots of Fig.3.3b and c. To a human eye both states would appear equally bright, only more sophisticated measurement apparatuses can detect the substantially different character of the light. We also note the dependence on the squeezing angle ϕ . This means that

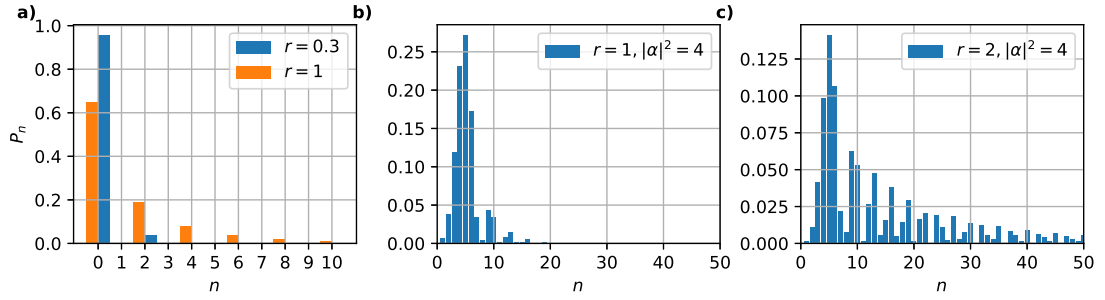


Figure 3.3: a) Probability of detecting m photons in a squeezed vacuum state for two different squeezing strengths r . The odd photon numbers have zero probability. b) The squeezing operator applied to a coherent state with $\alpha = 2$ (i.e. α real) with $r = 1$ and the angle of squeezing $\phi = 0$. Modifications at higher photon numbers start to become apparent but the state still looks similar to a coherent state. c) The squeezing operator applied to the same coherent state as in b) but with $r = 2$. This state bears little resemblance to a coherent state, i.e. the Poissonian profile is strongly altered.

the coefficients depend on the relative angle between the coherent state and the squeezing angle. This is illustrated in the appendix where states for different squeezing angles are shown (A.2).

We conclude this subsection by connecting the above discussion to the subject of number-phase squeezing which refers to sub-Poissonian photon number distributions. In particular, confusion often arises as to whether quadrature squeezing and number squeezing are the same phenomenon. The previously discussed plots, however, illustrate the significant difference between a number squeezed state, for example a Fock state with $n = 5$, and a squeezed state with $|\alpha|^2 = 5$ and thus the same (average) number of photons. A weakly squeezed coherent state approximates a sub-Poissonian distribution in n only for some squeezing angles while it is, so to speak, super-Poissonian or simply neither for other angles. In summary, quadrature squeezed light squeezes one quadrature at the expense of the other (or electric field at the expense of the magnetic field or vice versa) which can lead to sub-Poissonian statistics but also to a larger spread in Fock space.

3.2 Detecting squeezed light

Phase resolving the electric field, or quadratures for that matter, and their noise is technically challenging due to the high electric field frequencies. These are on the order of hundreds of Terahertz while electronic components do not extend far beyond the Gigahertz range. An elegant way to circumvent the problem is the technique of balanced homodyne detection, schematically depicted in Fig. 3.4a. The core idea is to mix the signal field down to accessible frequencies through beating it with a phase-stable reference field at the same optical frequency.

Formally, we express the local oscillator field as a coherent state and therefore write it as

$$\hat{E}_{\text{LO}} = \alpha e^{-i\omega t} + \alpha^* e^{i\omega t}, \quad (3.42)$$

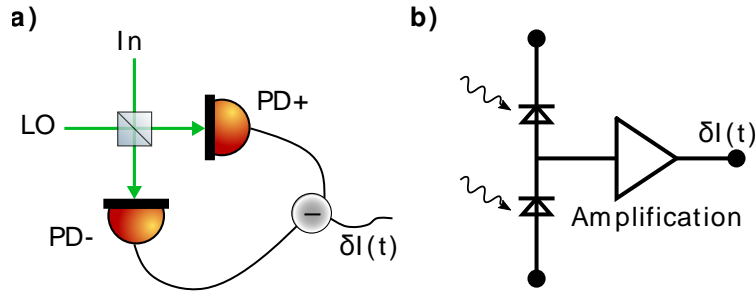


Figure 3.4: a) Principle of a homodyne detector: A signal field interferes with a local oscillator (LO) on a 50:50 non-polarizing beam splitter and the output is detected in both arms. b) The difference of the induced photo diode currents can be extracted by connecting the diodes in series and amplifying the difference current with a low-noise operational amplifier.

In the following we assume α to be real, i.e. the LO oscillator angle is assumed to be zero, since we are only interested in the relative phase between signal and local oscillator. Therefore, we express the signal field as

$$\hat{E}_{\text{in}} = \hat{a}e^{-i\omega t - i\theta} + \hat{a}^\dagger e^{i\omega t + i\theta} \quad (3.43)$$

where θ is the relative phase between signal and local oscillator. Now these fields interfere on a 50:50 non-polarizing beam splitter and the electric fields in the two output arms are given by

$$\hat{E}_1 = \frac{1}{\sqrt{2}}(\hat{E}_{\text{LO}} + \hat{E}_{\text{in}}) \quad (3.44)$$

$$\hat{E}_2 = \frac{1}{\sqrt{2}}(\hat{E}_{\text{LO}} - \hat{E}_{\text{in}}) \quad (3.45)$$

It follows from that the power in each arm has the following proportionality

$$P_1 \propto \langle \hat{E}_1^2 \rangle = \frac{1}{2}(\langle \hat{E}_{\text{LO}}^2 \rangle + \langle \hat{E}_{\text{in}}^2 \rangle + 2\langle \hat{E}_{\text{in}}\hat{E}_{\text{LO}} \rangle) \quad (3.46)$$

$$P_2 \propto \langle \hat{E}_2^2 \rangle = \frac{1}{2}(\langle \hat{E}_{\text{LO}}^2 \rangle + \langle \hat{E}_{\text{in}}^2 \rangle - 2\langle \hat{E}_{\text{in}}\hat{E}_{\text{LO}} \rangle) \quad (3.47)$$

Each beam splitter output is detected on a photo diode leading to a current proportional to the incident power. The difference between the two currents, accessed through a circuit sketched in Fig.3.4b, thus gives

$$\begin{aligned} \delta I &\propto \langle E_{\text{in}}E_{\text{LO}} \rangle \quad (3.48) \\ &= \langle (\hat{a}e^{-i\omega t - i\theta} + \hat{a}^\dagger e^{i\omega t + i\theta})\alpha (e^{-i\omega t} + e^{i\omega t}) \rangle \\ &= \alpha \langle \hat{a}e^{-i\theta} + \hat{a}^\dagger e^{i\theta} + \hat{a}e^{-2i\omega t + i\theta} + \hat{a}^\dagger e^{2i\omega t - i\theta} \rangle \end{aligned}$$

For the time average the terms oscillating at ω average to zero and we arrive at

$$\delta \hat{I}_\theta \propto \alpha [\hat{a}e^{-i\theta} + \hat{a}^\dagger e^{i\theta}] = \alpha \hat{X}_\theta \quad (3.49)$$

This means we can directly measure the quadrature via homodyne detection. Therefore, we can also measure its variance and compare it to the vacuum or a coherent state to show squeezing.

3.2.1 Losses

To complete this section we briefly discuss the role of the inevitable losses in detection, stemming from lossy transmissions, imperfect mode matching and imperfect detectors. The losses can be modelled via a beam splitter with transmission T where the vacuum state is incident on the other input, i.e. the squeezed state interferes with a vacuum state. The output mode creation operator for the beam splitter can be described as $\hat{a}' = \tau\hat{a} + \rho\hat{v}$, with $\tau^2 = T$ and $\rho^2 = 1 - T$ [44]. For the angle dependent quadrature this leads to

$$\hat{X}_{\theta,\text{out}} = \tau\hat{X}_{\theta,\text{in}} + \rho\hat{X}_{\text{vac}}. \quad (3.50)$$

The quadratures variances of the beam splitter input and the vacuum are uncorrelated, therefore

$$\langle(\Delta X_{\theta,\text{out}})^2\rangle = T\langle(\Delta X_{\theta,\text{in}})^2\rangle + (1 - T)\langle(\Delta X_{\text{vac}})^2\rangle. \quad (3.51)$$

This shows that losses reduce the observed amplitude of squeezing. Usually, the losses can be quantified and it is common in the squeezed light community to report both the observed squeezing amplitude and the squeezing amplitude corrected for losses.

3.3 Non-linear photon transport

Having reviewed the basic concepts such as coherent and squeezed states of light we now turn to the phenomenon of non-linear photon transport that generate such states. As mentioned in the chapter introduction, our experiment was sparked by recent work by Mahmoodian and collaborators [40] and this section reviews that work and the supplementary material with additional input from private communications. The purpose is to present the framework and develop insight into the spectra of the induced photon correlations.

3.3.1 Strongly correlated photons

We consider a system of N two level emitters that are weakly coupled to a waveguide. They are driven continuously with a resonant, coherent field. The input field is weak and therefore can be approximated as

$$|\alpha_{\text{in}}\rangle = e^{|\alpha|^2/2} \left[1 + \alpha\hat{a}_{k_0}^\dagger + (\alpha^2/2)\hat{a}_{k_0}^\dagger\hat{a}_{k_0}^\dagger \right] |0\rangle \quad (3.52)$$

For this framework the waveguide is rescaled and linearized, such that wave number k and frequency ω , as well as distance x and time t , have the same units. Resonant photons correspond to k_0 , and $\hat{a}_{k_0}^\dagger$ creates a photon with detuning k_0 . We assume a chiral system, i.e. photons emitted by an emitter into the waveguide can only be emitted in forward direction, which occurs at a rate of Γ_{wg} . Alternatively, photons can be scattered into free space i.e. they are lost to the reservoir. The ratio between these two rates defines the coupling strength $\beta = \Gamma_{\text{wg}}/\Gamma_{\text{tot}}$, where Γ_{tot} is the total decay rate into all channels.

To calculate the dynamics of the system we consider the scattering matrices for all components of the input state. Interaction with N atoms is taken into account by raising the scattering

matrices to the N th power. The full scattering matrix reads

$$\hat{S}^N = \hat{S}_{11}^N + \hat{S}_{22}^N + \sum_{M=0}^{N-1} \hat{S}_{11}^{N-M-1} \hat{S}_{12} \hat{S}_{22}^M \quad (3.53)$$

where \hat{S}_{11} and \hat{S}_{22} are the one- and two-photon scattering matrices, and \hat{S}_{12} corresponds to scattering of a two-photon input where one photon is lost and one is transmitted. The output state is calculated by projecting the scattering matrix onto the input state

$$\hat{S}^N |\alpha_{\text{in}}\rangle = |\text{out}\rangle_1 + |\text{out}\rangle_2 + |\text{out}\rangle_{21} \quad (3.54)$$

The projection of the two-photon input state onto the N -emitter two-photon scattering matrix is based on the Bethe ansatz technique as described in Ref. [45] and leads to

$$\frac{|\text{out}\rangle_2}{A} = \hat{S}_{22}^N |\alpha_{\text{in}}\rangle = \tilde{t}_{2k_0}^N c_1 |B_{2k_0}\rangle - \int d\Delta \frac{t_{k_0+\Delta}^N t_{k_0-\Delta}^N}{\Delta \sqrt{1 + 4\frac{\Delta^2}{\Gamma^2}}} |W_{2k_0,\Delta}\rangle, \quad (3.55)$$

where $c_1 = \sqrt{8\pi/\Gamma}$, $\tilde{t}_E = 1 - 4\beta/(1 + \beta - iE/\Gamma_{\text{tot}})$, and $A = (\alpha^2/L)e^{-|\alpha|^2/2} \propto P_{\text{in}}$ with the input power $P_{\text{in}} = \alpha^2/L$. L is a quantization length and α is assumed to be real. The integral is carried out over \mathbb{R} . The states $|W_{E,\Delta}\rangle$ and $|B_E\rangle$ are extended states and bound states, respectively, given in position space representation by [46]

$$W_{E,\Delta}(x_c, x) = \sqrt{2} e^{iEx_c} \frac{[2\Delta \cos \Delta x - \Gamma_{\text{tot}} \text{sgn}(x) \sin \Delta x]}{2\pi \sqrt{4\Delta^2 + \Gamma_{\text{tot}}^2}} \quad (3.56)$$

$$B_E(x_c, x) = \sqrt{\frac{\Gamma_{\text{tot}}}{4\pi}} e^{iEx_c} e^{-\Gamma/2|x|}, \quad (3.57)$$

where x_1 and x_2 are the two photon positions, $x_c = (x_1 + x_2)/2$ is the center-of-mass coordinate, and $x = x_1 - x_2$ is the difference coordinate, following the formalism in Ref. [45]. $E = k + p$ is the two-photon detuning and $\Delta = (k - p)/2$ is the frequency difference of the two photons with frequency k and p .

Carrying out the integration in Eq.3.55 leads to the full two-photon output of [40]

$$|\text{out}\rangle_2 = \frac{A}{2} \int dx_1 dx_2 \hat{a}^\dagger(x_1) \hat{a}^\dagger(x_2) |0\rangle \Psi_N(x_c, x), \quad (3.58)$$

with $\Psi_N(x_c, x) = e^{2ik_0x_c} [t_{k_0}^{2N} - \phi_N(x)]$. The term with $t_{k_0}^{2N}$ corresponds to photons pairs that simply transmitted past N emitters. The second term is a spectrum of correlated photons containing $\phi_N(x)$ due to the non-linear interaction. The complete analytical solution is extensive and is given in the supplementary material of Ref. [40]. Therefore, to develop an understanding of these correlated photons we numerically calculate $\phi_N(\omega)$ for different N and a coupling strength of 1% which is close to our experimental scenario. The result is shown in Fig. 3.5.

We can understand the plot as follows: The rate at which correlated photons are created is always highest on or close to resonance. For low optical depth, e.g. $N = 25$ in the plot, there

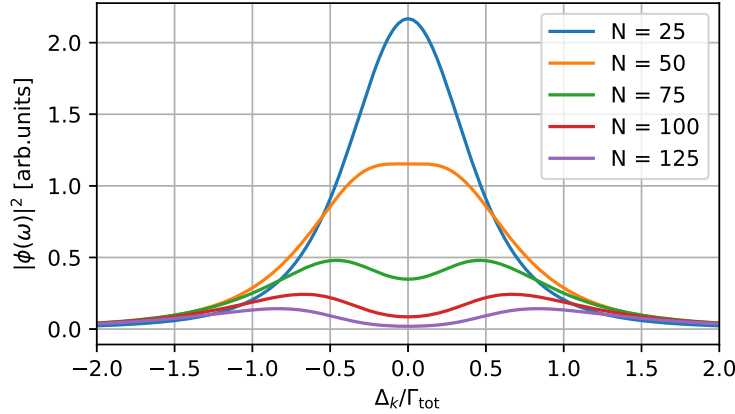


Figure 3.5: Spectrum of $\phi_N(\omega)$ for $\beta = 0.01$ and different N . As the inout state propagates through the ensemble, correlations build up in the form up sidebands. Due to absorption the correlated photons closer to resonance are absorbed more strongly and for large enough N only sidebands survive. This corresponds to the cartoon in Fig. 3.6b.

is a low probability to be absorbed and thus the output spectrum peaks on resonance. As the light continues to propagate through the ensemble, i.e. N increases, absorption becomes more pronounced and increasingly removes the correlated photons closer to resonance. Eventually, for high optical depth, all photons on resonance and close to resonance are absorbed and only the detuned components survive. In this limit the remaining output of the ensemble is highly non-classical since it consists essentially only of photon pairs that populate red- and blue-detuned sidebands. It appears as if these sidebands move outwards with increasing N but this is almost entirely due to the fact that photons closer to resonance are absorbed more strongly. This is apparent from Fig. 3.5 where $|\phi_N(\omega)|^2$ is, except for in the far-detuned wings, strictly smaller for larger N . This illustrates also a limitation of this process to generate non-classical light: The stronger the correlations the less light actually exits the ensemble. Therefore, in order to observe this effect experimentally one has to strike the right balance in the number of atoms N where notable correlations exist and the output still exceeds the detection noise.

3.3.2 Transmission properties of the ensemble

The previous section shows that the non-classical output from the ensemble has clear signatures in the photon statistics, for example it can be bunched. But in this section we show that in principle an even simpler experimental signature exists, namely the transmission scaling.

In order to calculate the transmission in the above framework it is necessary to compute the other terms in Eq.3.54. This is straightforward for the single-photon case where one simply multiplies the the creation operator by a transmission coefficient, such that $\hat{a}_k^\dagger \rightarrow t_k^N \hat{a}_k^\dagger$ with $t_k = 1 - 2\beta/(1 - 2ik/\Gamma_{tot})$ ([40] and ref. 54 [47] therein) to obtain

$$|\text{out}\rangle_1 = e^{-|\alpha|^2/2} \alpha t_{k_0}^N \hat{a}_k^\dagger |0\rangle. \quad (3.59)$$

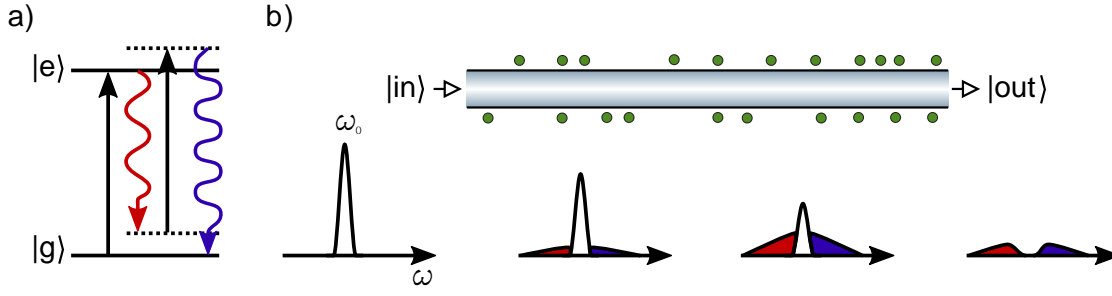


Figure 3.6: a) Two-photon atom-light interaction leading to energy-time entangled off-resonant photon pairs. b) Drive field spectrum as it propagates through the ensemble. For a large enough number of atoms the carrier is completely extinguished and only correlated photons remain.

For the single-photon transmission this means

$$\langle \hat{a}^\dagger \hat{a} \rangle_1 = \frac{|t_{k_0}|^{2N} |\alpha|^2}{L}. \quad (3.60)$$

This entails exponential decay of the one-photon input, consistent with the Beer-Lambert-law.

The last term to compute is $|\text{out}\rangle_{21}$, accounting for the loss of one photon in a two-photon state. To this end the chiral scattering picture is transformed to a transmission and reflection description [40, 47]. A complete calculation of this is given in the supplementary material of [40]. There, the result is given by

$$T_N = \frac{\langle \hat{a}^\dagger \hat{a} \rangle}{P_{in}} \sim (1 - 2\beta)^{2N} + \frac{P_{in}}{P_{sat}} \frac{\beta}{4\sqrt{\pi}\xi_N^3} \frac{3 - 2\beta(1 - \beta)}{1 - 2\beta(1 - \beta)}, \quad (3.61)$$

where $\xi_N = \sqrt{N\beta(1 - \beta)}$. This is plotted in Fig. 3.7 for $P_{in}/P_{sat} = 0.1$ and $\beta = 0.01$ and compared to the transmission predicted by Beer-Lambert's law.

The second term scales with $1/N^{3/2}$ such that for sufficiently large N the transmission deviates from the usual exponential decay. This stems from the fact that for large N the output is dominated by correlated and detuned photons since these experience lower losses than the resonant uncorrelated photons. Note that, for a coupling strength that is realistic in our experiment, deviations from Beer-Lambert's law occur below $T \sim 10^{-4}$. This makes it challenging to detect the deviation because it requires an extremely frequency pure input field. Another experimental complication is that the input power has to be low enough to make saturation effects negligible and thus the output is extremely weak and hard to detect with good signal-to-noise ratio.

3.3.3 From correlated photons to squeezed light

We reviewed the concept of squeezed light and introduced a theoretical framework to describe non-linear photon transport that leads to correlated photon output. In this section we establish a connection between these two frameworks. The core question is, if (and how) the photon correlations lead to squeezed light. We already know that the correlations occur in a finite

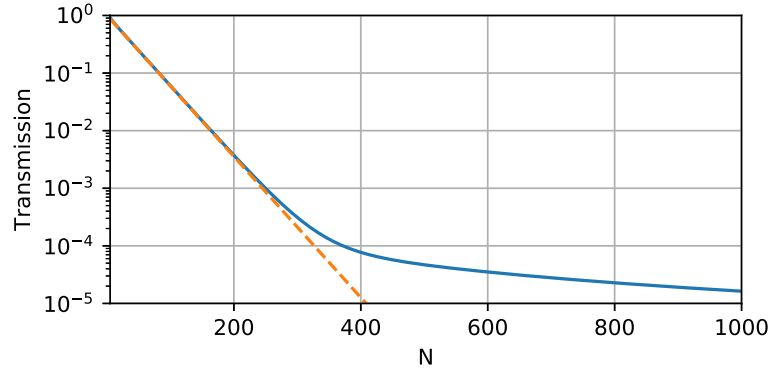


Figure 3.7: Transmission versus number of atoms for a saturation parameter of $S_0 = P_{in}/P_{sat} = 0.1$ and $\beta = 0.007$ (blue). Below 10^{-4} the transmission deviates notably from the exponential decay predicted by the Beer-Lambert law (orange, dashed) and scales proportionally to $1/N^{3/2}$

spectral range around the resonance so it seems intuitive to consider the squeezing in the spectral domain which is given by [48]

$$S_{\theta}(\omega) = \int_{-\infty}^{\infty} d\tau \langle : \Delta \hat{X}_{\theta}(0) \Delta \hat{X}_{\theta}(\tau) : \rangle e^{i\omega\tau} \quad (3.62)$$

where $\Delta \hat{X}_{\theta} = \hat{X}_{\theta} - \langle \hat{X}_{\theta} \rangle$. Underlying the above equality is the Wiener-Khinchin theorem that provides a direct relationship exists between the power spectral density of a variable and its auto-correlation function. This theorem is useful because it may occur that a process is easier to treat theoretically considering correlations in the time domain while it is easier to measure in the spectral domain. The theorem is explicitly stated in App.C.2. The above equality is the core connection between the theoretical framework and the measurement because the auto-correlation can be calculated well from the formalism. Using $\hat{X}_{\theta} = \hat{a}e^{i\theta} + \hat{a}^{\dagger}e^{-i\theta}$ we write for the auto-correlation

$$\begin{aligned} \langle : \Delta \hat{X}_{\theta}(0) \Delta \hat{X}_{\theta}(\tau) : \rangle &= \left(e^{2i\theta} \langle \hat{a}(\tau) \hat{a}(0) \rangle - \langle \hat{a}(\tau) \rangle \langle \hat{a}(0) \rangle \right) + c.c. \\ &+ \left(\langle \hat{a}^{\dagger}(\tau) \hat{a}(0) \rangle - \langle \hat{a}^{\dagger}(\tau) \rangle \langle \hat{a}(0) \rangle \right) + c.c. \end{aligned} \quad (3.63)$$

The terms of the right-hand side can be calculated for the output state $|\text{out}\rangle$ to order P_{in}/P_{sat} . For the first term we find

$$\begin{aligned} \langle \text{out} | \hat{a}(x) \hat{a}(0) | \text{out} \rangle &= e^{-\frac{|\alpha|^2}{2}} \langle 0 | \hat{a}(x) \hat{a}(0) | \text{out} \rangle_2 \\ &= e^{-|\alpha|^2} \frac{\alpha^2}{L} \psi_N(0, x) \sim P_{in} \psi_N(0, x) \end{aligned} \quad (3.64)$$

The next term to first order only gives a contribution from the single-photon component and we get

$$\langle \hat{a} \rangle^2 \sim t_{k_0}^{2N} P_{in}. \quad (3.65)$$

For the remaining terms it can be shown that they only contribute a flat background in this first order approximation [46] and they are therefore omitted. This has the consequence that the calculated squeezing spectrum is centered around zero. This has to be considered for the comparison with experimental data as is described below. Therefore, we obtain for the auto-correlation function

$$\langle : \Delta \hat{X}_\theta(0) \Delta \hat{X}_\theta(x) : \rangle = \frac{1}{2} \cos(2\theta) P_{\text{in}} [\psi_N(0, x) - t_{k_0}^{2N}] = -\frac{\Gamma_{\text{tot}}}{2\beta} \cos(2\theta) \frac{P_{\text{in}}}{P_{\text{sat}}} \phi_N(x) \quad (3.66)$$

Finally, to obtain the squeezing spectrum we Fourier-transform the above expression and obtain

$$S_\theta(\omega) = \int dx e^{i\omega x} \langle : \Delta \hat{X}_\theta(0) \Delta \hat{X}_\theta(x) : \rangle = -\frac{\Gamma_{\text{tot}}}{2\beta} \cos(2\theta) \frac{P_{\text{in}}}{P_{\text{sat}}} \phi_N(\omega) \quad (3.67)$$

where $\phi_N(\omega)$ is already familiar from Fig.3.5 and the discussion of it. Therefore, we already have an understanding of its dependence on N . We also note the $\cos(2\theta)$ dependence of the squeezing parameter S_θ which we also noted for the depiction of squeezed states via the uncertainty plots in Fig.3.2.

Single- or two-mode squeezing

Strictly speaking, the non-linear process that we examine generates two-mode squeezing which is apparent from the expression for $|\text{out}\rangle$ in (3.58) where the two creation operators create photons in different modes. However, in our measurement these appear as the same mode. This stems from the fact that the finite bandwidth of the detector implies a finite time resolution which again entails a finite energy resolution due to energy-time-uncertainty. If the correlated photons are shifted by less than the energy resolution of the detector it will detect interference of these photons, although they are in different modes, and measure squeezing in the spectral range that includes the frequency-shifted photons.

3.3.4 Detuned input field

The above analysis assumes a resonant drive field. But the formalism is also suited to account for detuning. Qualitatively, a detuned drive field leads to complex value for the function ϕ_N that contains the correlations of the output state. The squeezing spectrum for a detuned drive, which is measurable and thus has to be real, is therefore a modification of Eq.3.67 and is given by [46]

$$S_\theta(\omega) = -\frac{\Gamma_{\text{tot}}}{2\beta} \frac{P_{\text{in}}}{P_{\text{sat}}} \text{Re} \left[e^{2i\theta} \phi_N(\omega - k_0) \right] \quad (3.68)$$

Since ϕ_N is complex we can assign it an angle that then adds or subtracts from θ . This means that the phase at which maximum squeezing appears shifts. The phase difference between θ and the phase of ϕ_N can be understood as the angle of the squeezing operator that was introduced earlier in (3.15). Figure 3.8a shows how ϕ_N varies in magnitude for different drive detunings and atom numbers for a coupling strength of $\beta = 0.007^1$. Strongest correlations in absolute

¹This numerical calculation was kindly made available to us from the main author of [40], S. Mahmoodian

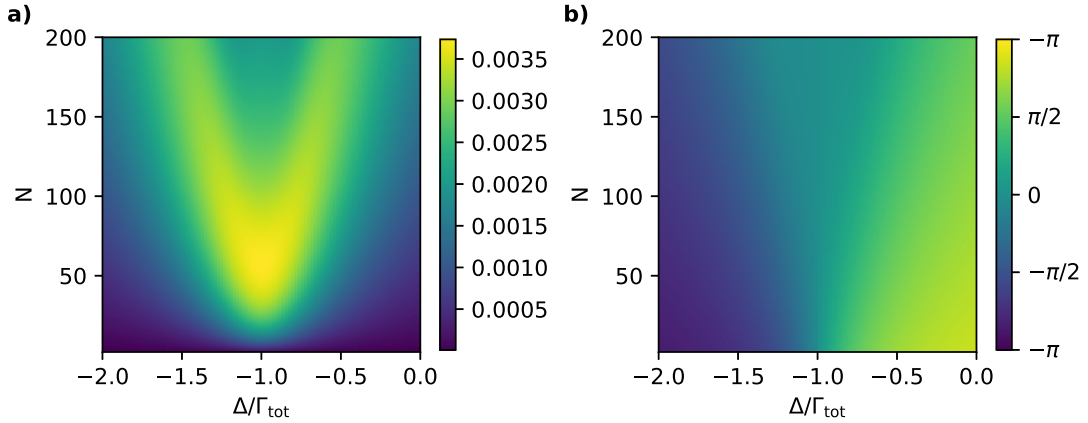


Figure 3.8: a) Magnitude of $|\phi_N|^2$ for $\beta = 0.007$ with respect to drive detuning Δ and atom number. For small N , squeezing, which is proportional to ϕ , is always strongest for resonant input fields whereas for higher atom numbers an off-resonant drive can increase the squeezing. Note that the global maximum of $|\phi|^2$ occurs on resonance. b) Angle of ϕ in polar form, indicating at which θ the coherent field is quadrature squeezed maximally. The angle approaches $\pm\pi$ for infinite detuning.

terms arise on resonance but for a large enough given N an off-resonant drive can actually induce stronger correlations. The phase of ϕ_N is shown in Fig 3.8b. For large detunings it approaches $\pm\pi$ asymptotically. This shows, that one cannot obtain perfectly phase squeezed light in the present framework because firstly, a phase shift of π is never reached and, secondly, the squeezing amplitude tends towards zero for larger detuning.

3.4 Comparing measurement and theory

We conclude the chapter by connecting the calculations here with the measured parameter that will be studied in chapter on the experimental observation of squeezing. There, we measure the relative spectrum between the nanofiber output and the vacuum, i.e. we reference the squeezed spectrum to an unsqueezed spectrum in a well defined frequency range from ω_{min} to ω_{max} . This means that the measured spectrum $\tilde{S}_\theta(\omega)$ is centered around 1. On the other hand the numerically calculated spectrum is centered around 0 and is calculated in a framework where $\hat{X}_\theta = 1/2(\hat{a}e^{i\theta} + \hat{a}^\dagger e^{-i\theta})$ so that the vacuum variance is $1/4$ rather than 1 as in this thesis. Therefore, the calculated spectrum relates to the measured spectrum via

$$\tilde{S}_\theta(\omega) = 4 \left[S_\theta(\omega) + \frac{1}{4} \right]. \quad (3.69)$$

For the the measured ratio Q we obtain

$$Q = \frac{\frac{1}{\Delta\omega} \int_{\Delta\omega} \tilde{S}_\theta(\omega)}{\frac{1}{\Delta\omega} \int_{\Delta\omega} 1} = 1 + 4 \frac{1}{\Delta\omega} \int_{\Delta\omega} d\omega S_\theta(\omega), \quad (3.70)$$

where $\Delta\omega = \omega_{\max} - \omega_{\min}$. Now we assume that our experimental integration bounds for ω_{\min} (ω_{\max}) are close enough to 0 (large enough) that S_θ is flat and the spectrum is contained within our limits. This allows us to compare Q to numerical results for $\langle : \Delta X(0) \Delta X(0) : \rangle / \Gamma_{\text{tot}}$, i.e. the auto-correlation integrated over the entire spectrum, via

$$Q = 2\pi \frac{1}{2} \frac{\Gamma_{\text{tot}}}{\Delta\omega} \frac{\langle : \Delta X(0) \Delta X(0) : \rangle}{\Gamma_{\text{tot}}} + 1 \quad (3.71)$$

where a factor of 1/2 accounts for the fact that experimentally we integrate only positive frequencies. This expression will be used for the theory comparison of the squeezing data for different input powers in Sec.5.7.

3.5 Summary

This chapter aimed at connecting the concept of squeezed light to recent theoretical work on non-linear photon transport through a nanofiber trapped atom ensemble. The fundamental description of light via quadratures was introduced and we showed the role of photon pairs in squeezed vacuum. The framework was then expanded to bright squeezed states and their Fock space distribution was discussed. In the second half we presented a theoretical framework to describe the generation of correlated photons from a weak, resonant drive in an atomic medium. Finally, we showed that these correlations can lead to squeezed light and we showed how the spectrum of squeezing is determined by the spectrum of the correlations. Finally, we discussed the consequences of a detuned drive field and showed from numerical calculations that the detuned drive field modifies the angle of squeezing.



Die approbierte gedruckte Originalversion dieser Dissertation ist an der TU Wien Bibliothek verfügbar.
The approved original version of this doctoral thesis is available in print at TU Wien Bibliothek.

Construction of a nanofiber-based dipole trap

The experiments reported in this thesis were performed on a newly-constructed apparatus starting in 2014 from empty optical tables. The basic scheme follows the nanofiber-based atom trap operating in our group for many years. However, several experimental aspects were reconsidered during the planning stage in order to achieve higher single atom coupling strength, reduce the linewidth of the trapped ensemble and achieve better optical access to the nanofiber. A key design idea was therefore to place the fiber in a glass cell. Improved alignment between MOT cloud and nanofiber is achieved through a translateable fiber mount. The nanofiber diameter is chosen to maximize coupling of the atoms to the guided modes. This chapter first details the construction of the apparatus and demonstrates and characterizes atom trapping.

4.1 Vacuum chamber

Magneto-optical traps and dipole traps operate under vacuum since collisions with background gas molecules otherwise kick atoms out of the trap. For our experimental requirements this means that the pressure in the vacuum chamber has to be low enough to reduce the number of collisions with hot background gas particles to be negligible during an experimental cycle, typically many milliseconds. To achieve a collision rate below $\sim 1/s$ this requires a background gas pressure below 10^{-9} mbar. This in turn determines the set of required vacuum pumps and UHV-proof vacuum seals, namely CF (Conflat) flanges, that achieve very low leakage rates.

The fundamental requirement of our vacuum chamber is to allow the creation of a magneto-optical trap around a nanofiber. The nanofiber needs to be interfaced from outside of the vacuum, thus requiring a fiber feedthrough from ambient pressure into the vacuum chamber. Our magneto-optical trap scheme requires optical access around the nanofiber for three mutually orthogonal beam pairs. An overview of the vacuum chamber designed for this experiment is shown in Fig.4.1. The main body is a cylinder with 246 mm inner diameter (CF250) in the hori-

4. CONSTRUCTION OF A NANOFIBER-BASED DIPOLE TRAP

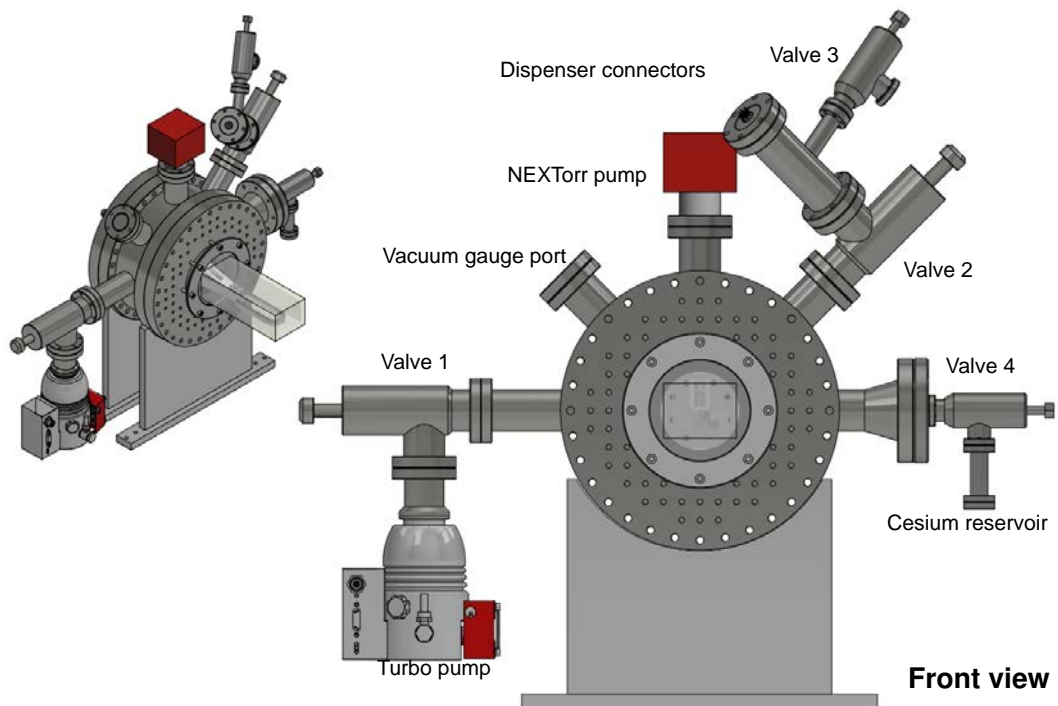


Figure 4.1: The complete vacuum chamber design rendered in Autodesk Inventor, in 3D and from the front. The back flange of the large, horizontally oriented vacuum cylinder holds a translateable fiber mount into a glass cell protruding from the front flange and connected via an indium wire seal. The tapered fiber is glued onto the frame at the fiber holder tip and aligned with the axis of the horizontal vacuum cylinder. Five smaller vacuum connections to the main chamber exist to connect (clockwise for the front view) a turbo pump via a UHV seal, a hybrid ion-getter pump, Cesium dispenser via a UHV seal, and a reservoir of elementary cesium via a UHV seal.

zontal plane with 5 radial connection tubes. One of the tubes is conically widened and serves as a backup option for attaching an ion pump with a CF60 connector. The other ports are used for the turbo pump, getter pump, cesium dispenser, and a vacuum gauge (not shown). The front of the vacuum chamber, where the glass cell connects, has a 25x25 mm grid of M6 threads to allow mounting optics to the chamber. The rear side of the vacuum chamber also has a few M6 threads which are used for mounting the back plate to the sledge used for inserting the nanofiber (see Sec. 4.1.5). Most importantly, the front flange also has a 86 mm diameter hole onto which the glass plate is connected and through which the nanofiber mount holds the fiber into the glass cell. The rear flange of the chamber has two CF35 flanges that are used for the fiber feedthrough and an electric feedthrough. It also has two CF16 flanges used for the mechanical feedthroughs for positioning the fiber mount in the chamber.

4.1.1 Vacuum Pumps

We use three consecutive pumping stages to reach high vacuum. The first stage employs a scroll pump (Leybold, SC15D) that is capable of pumping atmospheric pressure down to about 1 mbar. The scroll pump is connected to the exhaust of the turbo pump (Pfeiffer Vacuum, HiPace60). Once the pressure in the main chamber has dropped to 1 mbar the turbo pump is can be switched on. After several hours up to a few days of pumping, depending on the cleanliness of the chamber interior, the pressure has dropped to the order of 10^{-8} mbar. This means it is low enough switch on the last pump (SAES Getters, NEX Torr D 100) which is a combination of a getter pump and an ion pump. The former is activated by heating the getter plates up to 500° for about an hour. During this time, the pump body heats up notably but the main chamber warms up only slightly since the thermal contact via the CF-seal is weak. Then the heating is switched off and the getter material starts to absorb most gases except for the noble gases. These are pumped by a small ion pump element. During the activation of the getter pump the valve connecting the turbo pump to the chamber is kept open and the turbo pump continues to pump as the pressure in the main chamber rises due to the outgassing of the getter elements. Once the getter activation is finished and temperatures have dropped back to ambient levels the UHV-valve (Vacom, 4AVM-40CF-MM-S) connecting the turbo pump is closed by applying a well-defined torque with a torque meter. Typically the pressure, inferred from the ion pump current, drops further after this and the ion pump element converts the pump current into values around 10^{-9} mbar.

4.1.2 Cesium sources

Cesium dispensers

Loading a magneto-optical trap of Cesium from the vacuum background requires a Cesium background gas in the vacuum. In our experiment this can be achieved in two different ways. Firstly, standard Cesium dispensers (SAES, CS/NF/12.8/40 FT10+10) are placed in a T-piece that is connected via a UHV-valve to the main chamber. The T-piece is connected via a valve to allow for dispenser exchange without breaking the main chamber vacuum. There are five dispensers in the T-piece, connected electrically via an electric vacuum feed through. All dispensers have the same ground and are connected to separate feed through connectors on the other end for individual operation. A dispenser is activated by running the threshold current of about 5 A through it. This heats up the dispenser and a chemical reaction takes place in it which releases gaseous, atomic Cesium. The activation is accompanied by a peak in the vacuum pressure but it drops back to the original level within hours if the dispenser is operated at moderate currents. We found that after activation a current of 3-4 A was often sufficient to obtain $\sim 10^8$ atoms in the MOT which was usually sufficient for our experiment. Depending on the current and total operation time a dispenser can be used for many months with variations from dispenser to dispenser. When first activating a dispenser in a vacuum chamber that was recently under ambient pressure the chamber walls act as getter surfaces, i.e. they adsorb Cesium and thus reduce the Cesium background pressure until they are saturated. During this time higher dispenser currents are necessary to quickly reach this regime. Once the chamber is essentially coated with Cesium on the inside they dispenser current could sometimes be reduced substantially without reducing the number of atoms in the MOT notably.

Elementary cesium

The other way of generating a Cesium background pressure is by placing elementary Cesium in the vacuum chamber and heating it to increase the vapor pressure in the vacuum chamber. In principle, this is the cleanest way of creating a Cesium background pressure because it does not involve any other elements as is the case for the dispensers with their chemical compounds from which Cesium is released. The downside, however, is that Cesium is very reactive and cannot be exposed to air. Elementary cesium is thus purchased in glass ampoules that have to be broken under vacuum to prevent the strongly exothermal reaction of Cesium and Oxygen that takes place in air. Due to persistent problems with stable atom trapping, described in Sec.4.7, we had the hypothesis that the fiber might be contaminated with Cesium dispenser byproducts and we installed a Cesium reservoir in our vacuum chamber. One gram of Cesium in a glass ampoule was placed in a CF16 bellow that connected to the CF60 outlet of the main vacuum chamber via another valve. Before connecting it to the main chamber we pumped the bellow separately and broke the glass ampoule inside by bending the bellow until the glass cracked. Then the valve was connected to the main chamber while the main chamber was pumped with the turbo pump and the CF16 UHV valve was opened, thus exposing the elementary Cesium to the vacuum in the main chamber. A current-carrying wire was spun around the bellow to heat up the Cesium and increase evaporation. The CF gaskets around the Cesium reservoir are silver coated to prevent the elementary Cesium from reacting with the copper CF gaskets which can damage the seal.

The results of obtaining a background pressure from elementary Cesium were mixed. After exposing the elementary Cesium to the main vacuum for a few days, thus coating the inside of the chamber with a thin layer of elementary Cesium, the background pressure of Cesium was sufficient to generate a MOT with 10^7 atoms. Almost-closing the CF16 valve by tightening it handtight shrunk the MOT size immediately, proving that the MOT atoms were mostly evaporating from the Cesium reservoir. However, this atom number was still an order of magnitude below what we achieved with the Cesium dispensers. We attempted to increase the atom number in the reservoir-generated MOT by installing UHV LEDs around the glass cell such that light-induced desorption of Cesium from the glass surfaces temporarily increases the Cesium background pressure in the region around the MOT. This led to a $\sim 10\%$ increase of atom number in the MOT and thus fell short of our expectations. The conclusion for the Cesium reservoir was that it works in principle but not well enough for our purposes. This may be explained through the small vacuum cross-section due to the valve via which the reservoir is connected to the main chamber. Another explanation may be a too little heating of the reservoir. Since the suspicion of dispenser by-products harming the nanofiber did not solidify (see Appendix B) we returned to using the dispensers as Cesium source.

4.1.3 Glass cell

A key design goal of our nanofiber trap setup compared to the first generation fiber trap operated in our group was better optical access to the nanofiber. To this end the fiber mount is placed in a glass cell protruding from the steel vacuum chamber that allows to interface the fiber from various angles. Connecting glass parts to steel vacuum chambers, however, comes with the

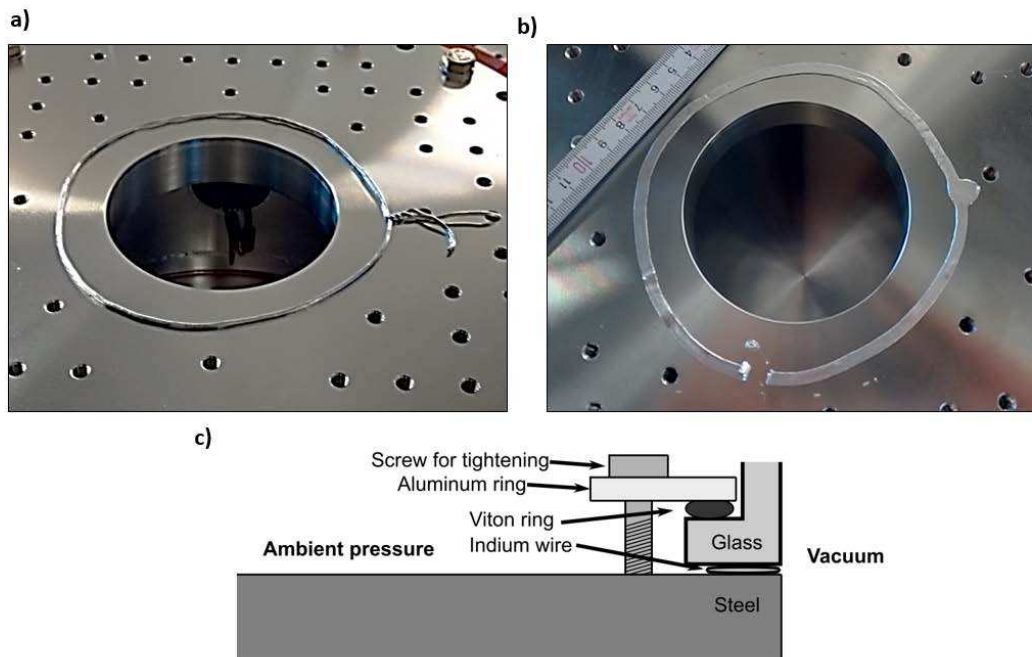


Figure 4.2: Indium wire seal between the glass cell and the steel chamber. a) Indium wire loop before flanging the glass cell onto it. The section of twisted wire turned out to leak. The wire loop for the final indium seal had therefore no twisted section and the wire ends were instead melted together with a heat gun. b) The squeezed wire after breaking the seal. c) Sketch of the steel-to-glass vacuum seal achieved via the Indium wire.

technical challenge of achieving a seal between glass and steel. A common solution is a metal-to-glass transition but these have the disadvantage of extending over long sections of more than 10 cm. This would render the glass cell protrusion so long that a nanofiber mount would have to be held into the glass cell via a long and sleek arm, a mechanically unstable solution. To circumvent this problem the glass cell is connected directly to the flange via an indium wire seal. Here, a glass surface is contacted to a steel surface via a wire of elementary indium of about 1 mm thickness. Indium has a melting temperature of 156°C and is malleable at room temperature. Therefore, when pushing the glass surface onto the steel surface the indium wire in between flattens and forms a UHV-proof seal between the steel and the glass, as depicted in Fig.4.2. The downside is that the vacuum chamber can not be heated above the indium melting point any more. The glass cell in our experiment (Hellma Optics, custom design) has a box shape (60 x 80 x 200 mm outer dimensions) with one end of the box connected to a glass flange of 135 mm diameter. The glass (Silica) is 15 mm thick and anti-reflex coated for 852 nm on the outer surface. According to the specifications of the manufacturer the AR coating reduces the reflection from about 4% to less than 0.5% for normal incidence. The steel front flange of the main chamber has a circular cut-out of 86 mm diameter over which the glass cell is positioned with a loop of indium wire in between the glass and the steel surface. The glass flange is pushed

onto the steel flange with an Aluminum ring together with a Viton ring (normally used as KF vacuum seal) between Aluminum and glass to avoid high local contact pressures that could crack the glass. We use a feeler gauge to ensure that the space between glass flange and steel flange is uniform around the seal while we tighten the Aluminum ring until the glass-steel separation is reduced to $300\ \mu\text{m}$. Leak tests were performed on the assembled vacuum system and no increased leakage was measurable at the indium seal.

4.1.4 Translatable fiber mount

The position of the magneto-optical trap is governed by the shape of the magnetic field created with the magnetic coils around the glass cell. The exact position of the trap center thus depends on the magnetic coil position which is difficult to adjust once the cage with the coils has been positioned around the glass cell. Therefore, rather than shifting the trap we move the fiber to the center of the cloud¹. To this end the fiber mount position has to be adjustable when the chamber is under vacuum. Our solution is to connect the fiber holder to the rear flange of the main chamber via a tiltable mount where mechanical feed throughs (Pfeiffer Vacuum, 420MZF016-010) allow tilting of the fiber holder in the vertical and horizontal direction, similar to the functioning of a mirror mount. An Autodesk Inventor depiction of the mount is shown in Fig. 4.3. The arm holding the fiber mount is screwed onto a plate with several holes through which springs pull the plate onto a holder base which is in turn screwed with vented vacuum screws onto the rear flange of the main chamber. One corner of the arm back plate is pulled onto the holder base with a 10 mm diameter steel ball between the two such that the ball acts as a joint about which the fiber holder can rotate in the horizontal and vertical direction. The holder arm has a pyramidal shape to increase stability with cut-outs that reduce its weight while maintaining rigidity. The fiber mount is detachable to remove it from the chamber for the nanofiber pulling process where the nanofiber is glued onto the holder in the fiber pulling rig. The mechanical feedthroughs push onto the fiber holder back plate with micrometer screws that can exert sufficient force to counter the screws pulling. Overall, the fiber mount can be shifted several centimeter and thus makes it easy to overlap fiber waist and MOT in the fiber-transverse directions.

4.1.5 Placing a nanofiber in vacuum

Transferring a nanofiber from the pulling rig to the vacuum chamber is a delicate task during which the nanofiber has to stay absolutely clean. Any dirt particles in the evanescent field lead to increased absorption which can fuse the fiber when the relatively strong trapping fields are switched on. Already a single dust particle on the nanofiber waist is sufficient to render it useless for our experimental scheme. Fiber cleanliness is therefore the most important aspect during nanofiber transport.

After pulling the nanofiber in the clean environment of the fiber pulling rig, it is glued onto the fiber mount and placed inside a tupper ware box that is cleaned carefully beforehand. The box has a small cut-out at one end where the tails of the nanofiber reach out from the box.

¹c.f. Francis Bacon, 'If the mountain won't come to Muhammad, then Muhammad must go to the mountain', Essays, 1625

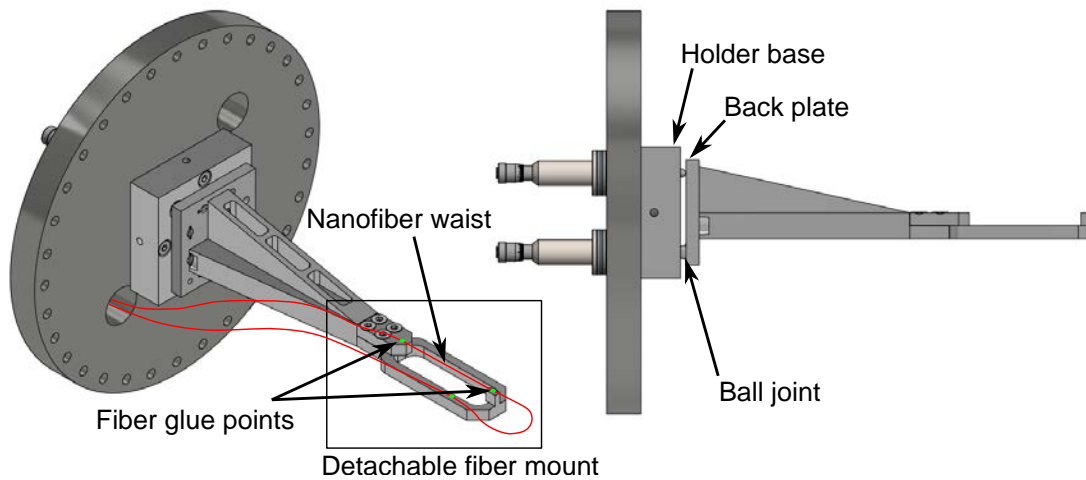


Figure 4.3: Assembly of the translateable fiber mount: Mechanical vacuum feedthroughs push onto the fiber mount back plate which in turn is pulled onto the holder base via springs. The arm can move about a ball joint between holder base and back plate, allowing to tilt the fiber holder in two directions similar to a mirror mount. The fiber mount can be unscrewed from the arm to be placed inside the fiber pulling rig where the pulled fiber is glued onto it after fiber pulling (green marks).

After closing the box with the cleaned lid we carry it from the pulling rig lab to the lab of our experiment where the vacuum chamber has been prepared and is ready to have the fiber placed inside. A small flow box is created over the vacuum chamber by mounting a HEPA filter above it with a fan that generates a laminar flow of filtered air around the nanofiber mount. This achieves a clean environment during mounting of the fiber holder onto the fiber arm. Once the fiber is mounted the tails are fed through the swagelok connector on the rear flange of the vacuum chamber and the whole rear flange is pushed carefully onto the vacuum chamber while ensuring that the fiber mount moves forward into the glass cell section without touching the side walls or bending the optical fiber at any point. A fiber check is coupled to the fiber during the whole procedure such that the nanofiber waist is visible and dust particles settling on it are noted immediately. In that case the whole procedure is stopped since the fiber cannot be used for trapping anymore. If the fiber waist appears clean up to this point the rear flange of the main chamber is tightened and we can start to evacuate the chamber. The key objective during evacuation is to prevent any major air flow inside the vacuum chamber during pumping to not stir up dust from the chamber bottom that can settle on the nanofiber waist. Thus we start to pump the chamber slowly by connecting the scroll pump used for the first pumping stage via a needle valve that can be opened slowly thus avoiding sudden pressure drops inside the chamber. From here on we pump the chamber down to high vacuum as described in Sec. 4.1.1.

4.2 Magnetic coil construction

Magnetic field control is required for the magneto-optical trap and for creating or offsetting magnetic background fields. Detailed considerations and simulations for the number of wire loops and resulting magnetic fields can be found in another PhD thesis that describes this experimental setup [49]. Our original design for the metal frame on which the wire was wound is shown in Fig. 4.4a with a coordinate system for orientation. The following coil pairs were crafted and calibrated with a magnetic field sensor (Sypris, Model 6010):

- **Quadrupole coils for magneto-optical trap:** Two race-track shaped coils, 225 windings, oriented along the x-axis, are designed to create magnetic field gradients of a few G/cm when operated with mutually counter-propagating current. For a current of 1 A, the gradient at the trap center was measured with 1.3 G/cm along the z-axis, 3.5 G/cm along the x-axis, and 2.7 G/cm along the y-axis. The elongated shape stretches the MOT cloud along the nanofiber axis to achieve better overlap and trap more atoms.
- **Bias coils:** Two rectangular coils, 140 windings, oriented along the y-axis, to create homogeneous offset fields in Helmholtz-like configuration. Here, the design consideration was to be able to create energy shifts between adjacent Zeeman states corresponding to five times the Cesium D2 linewidth of 5.2 MHz which requires a magnetic field of around 120 G. In hindsight this splitting is unnecessarily high for optically resolving Zeeman-sublevels. The field was measured to be 16 G at the position of the nanofiber with a magnetic field probe for a current of $I = 0.5$ A. It follows that for the maximum current of 10 A available through the current driver the offset field is 320 G, i.e. the coil pair is capable of producing the intended magnetic fields. However, most of the time this coil pair was operated in anti-Helmholtz configuration to create a quadrupole field that combines advantageously with the quadrupole field from the main MOT coils if the relative current direction between bias coil pair and MOT coil pair is correct. In this case, it reduces the field gradient along the nanofiber axis and increases it transverse to the nanofiber. This stretches out the MOT-cloud along the nanofiber up to several centimeters. The quadrupole field generated by 1 A anti-parallel current through the Bias coil pair was measured to have a gradient of 0.5 G/cm along the z-axis, 0.85 G/cm along the x-axis and 1.4 G/cm along the y-axis.
- **Axial compensation coils:** 100 windings, oriented along the z-axis, are designed to create a homogeneous background field at the trap center in order to move the MOT position along the nanofiber, the only direction along which the nanofiber cannot be moved via the fiber mount. Indeed, without shifting the quadrupole field center the MOT-position was not centered on the nanofiber waist in z-direction and thus was shifted via the axial compensation coils to achieve optimum overlap between cloud and fiber waist. The separation between the two coils is chosen so as to not block any of the horizontal MOT beams or the horizontal imaging axis.

Heat-conducting glue was applied after every layer of wire loops to make the coil mechanically rigid and to improve thermal conduction. The coil frame, milled in the institute metal

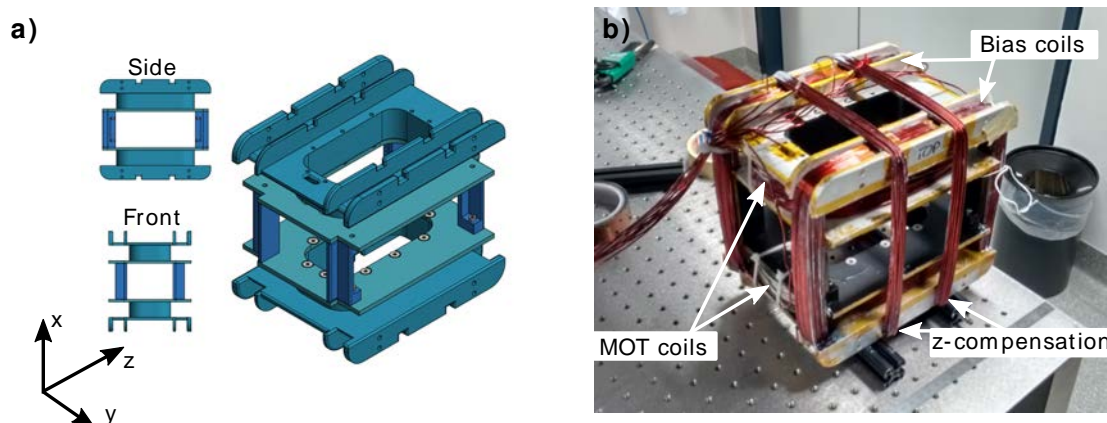


Figure 4.4: a) 3D drawing of the frame design with a side and front view on the left. The frame allows to combine three coil pairs into one rigid holder. The design was milled in several pieces and then screwed together into the final shape. b) Realization of the magnetic coil frame with the coils spun onto it. The points of contact between coil and frame were covered with isolating tape to prevent short-circuits. The frame inside was painted black to reduce spurious reflections of the MOT beams.

workshop, was spanned onto a motorized rotation stage and rotated with the wire spinning off its spool under reasonable tension to make a sturdy coil. The whole coil frame is screwed onto two aluminium bars resting on the bread boards for the horizontal MOT optics which hold the coil frame at the right height around the glass cell.

The original frame design considered only three coil pairs since in principle one can switch respective current orientations dynamically and apply different currents in the coils of one coil pair. This can create both gradient- and offset-fields in any desired direction and combination. In practice this was found to be impractical. For example, in order to create both the MOT quadrupole field and an offset field in the vertical direction the MOT coils have to be operated at slightly different currents. The MOT coils are designed for fairly strong gradients, however, a magnetic background field such as earth's magnetic field is weak such that the field to compensate it has to be weak. This required a very small current difference in the coils since they consist of a large number of windings which turned out to be on the order of the current resolution achievable via the current drivers and our Adwin control system. Therefore, it was decided at a later stage to add additional compensation coils to the coil frame. This was technically challenging since at this point the coil frame was already placed around the glass cell and the optical elements for the MOT were in place such that it was poorly accessible. Eventually, one separate wire loop was added to each transverse bias coil ('Bias Compensation Coil') while three separate loops were added to the MOT coils ('Vertical Compensation Coil'). From then on, the experiment was operated with three separately controllable compensation coils that allowed for accurate cancellation of background fields. The compensation coils were calibrated via microwave spectroscopy as detailed in 4.3.4.

4.3 Magneto-optical trapping of Cesium

The technique of laser cooling and trapping of atoms is a common and well established tool in contemporary quantum optics experiments that can provide clouds of atoms of up to 10^9 atoms at a few Microkelvin that can be trapped in the fairly shallow potentials of optical dipole traps [50]. In essence, it requires a quadrupole-shaped magnetic field and red-detuned laser beams intersecting at the absolute magnetic field minimum with correct polarization relative to the magnetic field orientation. The magnetic field is provided by the MOT coils detailed in the previous section, the optical setup is described in the following paragraphs. Once a MOT-cloud is trapped it is further cooled via polarization-gradient cooling, also called an optical molasses or sisyphus cooling [51, 52]. This is a powerful technique that can cool the cloud down to the recoil-temperature which corresponds to the kinetic energy of the recoil from a single-photon. During the optical molasses the cloud is not trapped so that it expands and falls freely while the atoms experience a force from the molasses that is equivalent to friction and causes the cooling.

4.3.1 Optical setup

Our MOT design requires three counter-propagating beam pairs along the three spatial dimensions. Two beam pairs lay in the horizontal plane and intersect each other under an angle of 90° . The third beam is along the vertical axis. An overview of the optical setup is presented in Fig. 4.5. Our MOT scheme consists of a strong light field (referred to as 'Cooler') red detuned to the $6S_{1/2}, F = 4 \rightarrow 6P_{3/2}, F' = 5$ transition on the D2-line of Cesium and a weaker field on resonance to the $6S_{1/2}, F = 3 \rightarrow 6P_{1/2}, F' = 4$ transition on the D1 line (referred to as 'Repumper'). The former transition is required for the cooling and generating the trapping force. The transition is almost closed, meaning that via a dipole transition an atom can only decay to the original $F = 4$ state when excited on this transition due to angular momentum conservation. However, off-resonant excitation to the $6P_{3/2}, F' = 4$ state is still possible from where an atom can decay to $6S_{1/2}, F = 3$ and where it is off-resonant to the cooler. The repumper's purpose is to prevent atoms from accumulating in this state by pumping them via the state $6P_{1/2}, F' = 4$ back to the $6S_{1/2}, F = 4$ ground state and thus close the cooling cycle. Cooler and repumper are transferred from the laser table to the experiment optical table via optical fibers and have output powers of 300 mW and 130 mW, respectively. They are collimated with $f = 50$ mm lenses to achieve an initial beam diameter of 6 mm (here, diameter defines the diameter of the circle at which the intensity has dropped to 13.5% of the maximum intensity at the beam center). Next, they are spatially overlapped on polarizing beam splitter (PBS) and split equally on a subsequent PBS where one arm is sent to the vertical MOT axis and the other to the two horizontal MOT axes. Thus, the power in the vertical beam is double the power of the horizontal pairs, in line with the fact that in a quadrupole field the magnetic field gradient in the vertical direction is twice the horizontal gradient. The vertical pair output of the second PBS is split on another subsequent PBS for the upward and downward oriented beam. The $\lambda/2$ -waveplate before this last PBS controls the power balance between the two beams and offers a practical way of balancing their radiation pressure onto the MOT cloud. The downward MOT beam is sent to a small breadboard on top of the glass cell, widened up to a diameter of 18 mm via a 3:1 telescope ($f_1 = -50$ mm, $f_2 = 150$ mm) and then sent through the glass cell. Similarly, the upward MOT

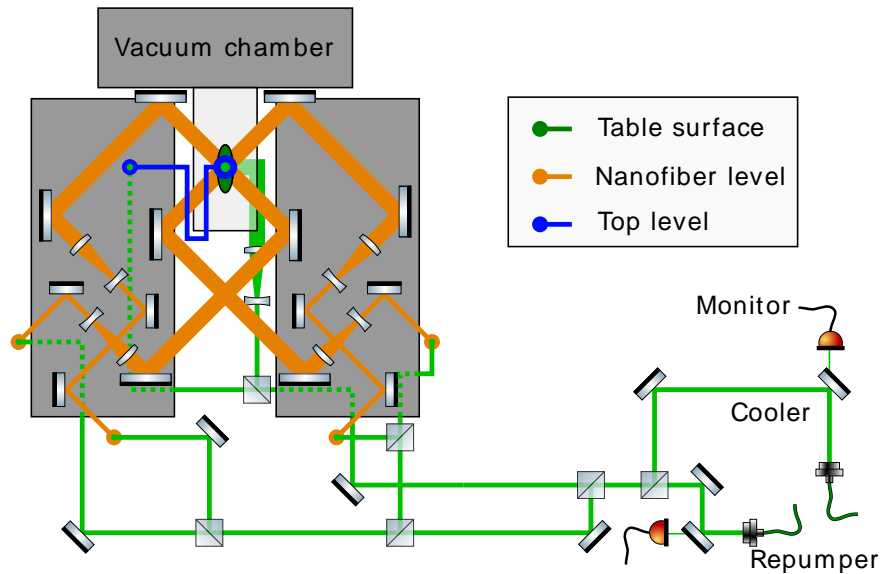


Figure 4.5: The beam path of the optical setup for the magneto-optical trap, following the actual layout on the table closely. $\lambda/2$ -waveplates are positioned before every polarizing beam splitter to adjust the splitting ratio but for clarity they are not depicted. All six MOT beams are widened up to a final diameter of 18 mm via telescopes. $\lambda/4$ -waveplates (not depicted) are placed before the telescopes to achieve circular polarization for the MOT beams inside the glass cell. Different height levels (table surface, first level at the height of the nanofiber indicated by the grey breadboards left and right of the glass cell, and the setup on top of the glass cell) of the beams are indicated by different colors and the circles indicate a vertical beam. Cooler and repumper are combined on a polarizing beam splitter and co-propagate through the rest of the setup. Dotted lines indicate beam paths below the optical breadboards. The telescope widening the beam in the top setup was omitted for overall clarity.

beam is widened to the same diameter and sent through the glass cell. The horizontal beam pairs are obtained from additional PBS, sent upward to a breadboard at the height of the glass cell where they are sent through 3:1 telescopes before propagating through the glass cell. After the last PBS each beam's polarization is turned to circular polarization via $\lambda/4$ -waveplates. Initially, the necessary waveplate angles were determined by placing a free space polarization analyser after each telescope and optimizing the polarization circularity measured at this position. Once a MOT is achieved the waveplate angles is optimized further by minimizing the overall movement of the MOT-cloud during the optical molasses which implies radiation pressure balance.

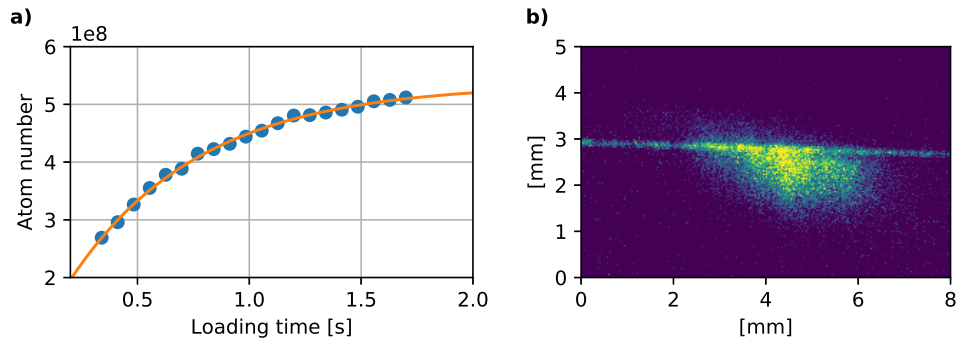


Figure 4.6: a) Loading curve of the MOT: Number of atoms in the MOT as a function of loading time. The exponential loading curve has a time constant of 0.6 s. b) Absorption image of the MOT cloud after 4.5 ms molasses cooling, superposed with a fluorescence image of the nanofiber.

4.3.2 Trap loading

The magneto-optical trap is realised by combining the optical fields of the cooling laser and the repumper laser with the quadrupole magnetic field generated by the magnetic coils. The cooler detuning from the cooling transition is 15 MHz, roughly three linewidths of the cooling transition, and the repumper is on resonance. The MOT coil current is typically 1 A, such that the magnetic field gradient at the trap center is between 1.3 and 3.5 G/cm, depending on the axis. Once the MOT configuration is switched on, atoms start to accumulate at the trap center which we observe via fluorescence detection on a camera. Figure 4.6 shows a loading curve where we plot the number of atoms in the MOT, obtained via absorption imaging, as a function of the loading time. The loading from the background decreases exponentially with a time constant of 0.6 s and saturates after approximately two seconds. Generally, these values strongly depend on the power of the cooling beams, cooler detuning and Cesium background pressure.

4.3.3 Absorption imaging experiments

In order to achieve good overlap between the nanofiber and the MOT cloud, and to measure the size and temperature of the cloud, two absorption imaging setups were included in the optical setup around the glass cell. The horizontal imaging setup is depicted in Fig. 4.7. Resonant light is coupled out from an optical fiber via a large-beam fiber collimator (Thorlabs, F810APC-842) and subsequently the 8 mm beam diameter is increased to 26 mm via a telescope such that MOT clouds up to a few mm diameter are illuminated evenly. For absorption imaging a resonant pulse is shone at the cloud and the shadow is imaged onto a CCD camera (Matrix Vision, mvBlueFOX3-1013GE). The vertical absorption setup follows the same principle with the major difference being that the resonant beam co-propagates with the upward MOT beam. This is achieved by superposing the two beams on a PBS where they exit with orthogonal polarizations which allows to separate the imaging beam from the MOT beam on another PBS after transmitting through the glass cell. The magnification of the image is 0.54 in the horizontal direction

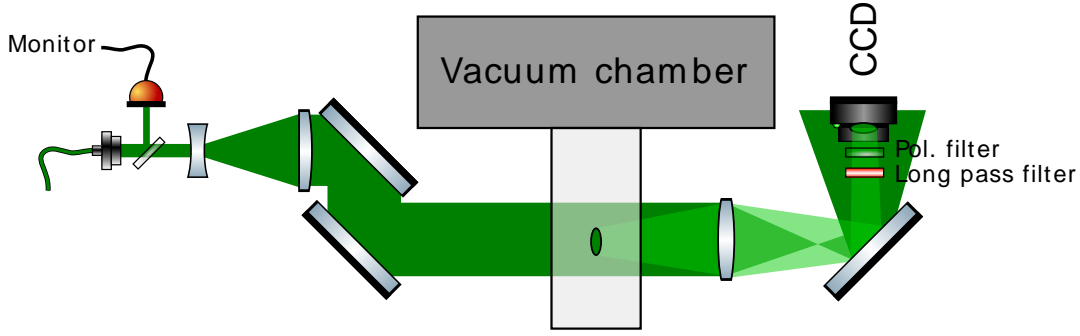


Figure 4.7: Optical setup for absorption imaging of the MOT cloud in the horizontal plane. The telescope widens up the beam to 8 mm before it illuminates the cloud to image the shadow onto the CCD camera. The linear polarization filter is required for aligning the polarization at the nanofiber waist (see 4.4.1) while the long pass filter at the camera can be used to block the bright scattering from the blue trap field to be able to align the red trap and probe field polarizations which scatter less light. Additionally, the filter prevents image distortion due to stray light.

with pixel-size limited resolution of $9.8 \mu\text{m}$ and a $12.5 \times 10 \text{ mm}$ field of view. For the vertical axis these values are 0.36 , $14.8 \mu\text{m}$, and $14 \times 10 \text{ mm}$. The smaller magnification of the vertical axis stems from the larger distance between imaging lens and cloud since the former can only be placed beyond the PBS separating imaging light from MOT light.

For an absorption image of the atom cloud we record three images. The first two by shining resonant light at the cloud and at the camera from the illumination fiber outcoupler. The first one is taken with the atomic cloud present, the second as a reference after it has fallen down, and a third dark image is recorded without any light to record the CCD chip background. Then we calculate an optical depth (OD) map from the transmission for the field of view via

$$-\ln T = -\ln \left(\frac{\text{image} - \text{dark}}{\text{reference} - \text{dark}} \right) \equiv OD. \quad (4.1)$$

From this optical depth we then calculate the column density of atoms in the MOT.

Atom number estimate

For such transmission maps one can calculate the number of atoms in the cloud provided that the cloud is dilute enough such that the lowest transmission on the shadow image was within the dynamic range of the CCD. This means that for a 10-bit CCD chip, the lowest transmission that can be recorded is $1/1024$, corresponding to an optical depth of ~ 7 . If the transmission is high enough we calculate the total atom number in the cloud by integrating the transmission map along both image axes. The total number N of absorbers with scattering cross-section σ is calculated via

$$N = \frac{1}{\sigma} \int_x \int_y OD = \frac{A_{\text{pixel}}}{\sigma} \sum_{x,y} OD_{x,y}. \quad (4.2)$$

4. CONSTRUCTION OF A NANOFIBER-BASED DIPOLE TRAP

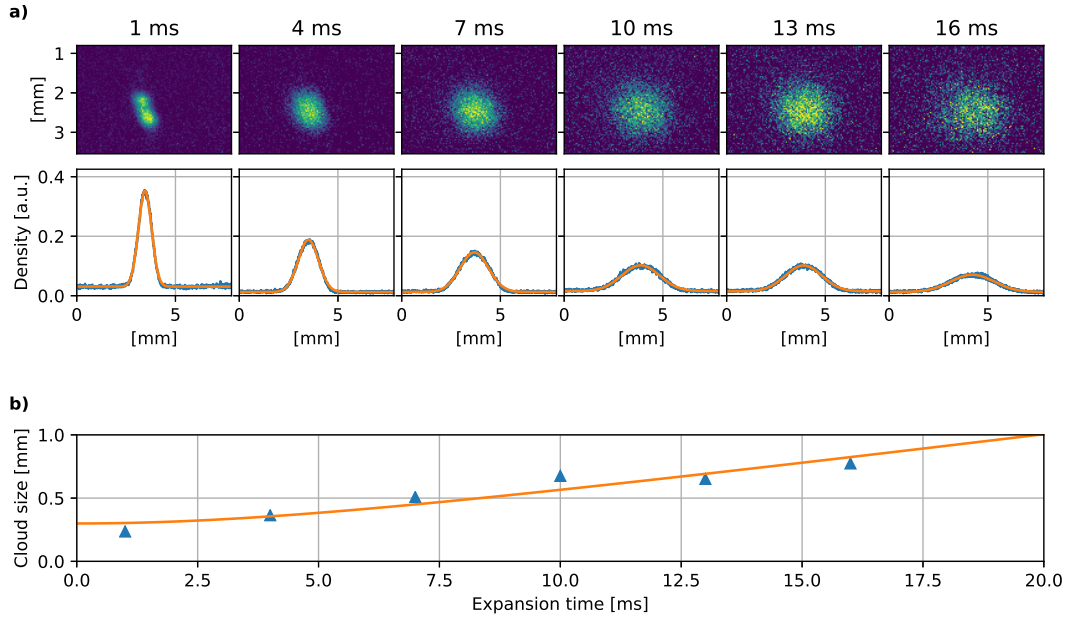


Figure 4.8: a) Upper row: Absorption images of the cloud after 1 ms of molasses cooling and varying expansion time. Lower row: Cloud density averaged along the y-axis of the upper row with Gaussian fits to extract the cloud width. The colorbar of the images is optimized for contrast and thus different for each image. b) Cloud width extracted from a) versus expansion time. The linear fit according to Eq. 4.4 yields a temperature of $37 \mu\text{K}$.

The scattering cross-section σ can be obtained from literature [53]. The expression with sums is the experimental adaptation of the physical formula where A_{pixel} is the area in the object plane mapped onto one pixel of the CCD chip.

Temperature measurement

Imaging the atom cloud as described above also allows to extract the cloud temperature. To this end, the cloud expands freely during free fall and the cloud size is measured at different stages of expansion. The free expansion effectively maps the initial velocity distribution of the cloud onto the shape we observe. Obtaining this velocity distribution provides a measure of the cloud temperature since in an ideal thermal gas the velocity distribution follows the probability distribution [54]

$$f(v_z) = \sqrt{\frac{M}{2\pi k_B T}} \exp\left(-\frac{Mv_z^2}{2k_B T}\right), \quad (4.3)$$

where M is the atomic mass, v_z is the atom velocity in z -direction, and T the temperature of the atomic gas. This expression is a Gaussian with a width given by $\sigma = \sqrt{k_B T / M}$, i.e. the cloud size we measure after expansion is directly linked to its temperature. To measure the expansion speed, i.e. v , the cloud has to be imaged after different expansion times and the size $L(t)$ is extracted. In the simplest case, this size is a convolution between its initial spatial distribution

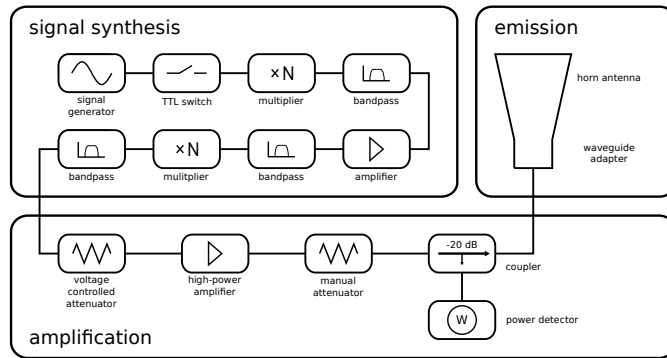


Figure 4.9: Signal chain for generating the 9.2 GHz MW signal (depiction from [56]). The signal originates from a programmable MW vector generator that outputs a stable signal at 2.3 GHz. The final frequency for the Cesium hyperfine ground state transition is reached through two frequency doublers. After amplification the MW field is directed at the atom cloud via a horn antenna. The MW pulse length is controlled via a digital MW switch while the power is controlled both via a manual attenuator (coarse) and a voltage controlled attenuator (fine).

and the velocity distribution mapped onto real space. Therefore, the cloud size measured after time t is described by

$$L(t) = \sqrt{L_{\text{init}}^2 + \frac{k_B T}{M} t^2} \quad (4.4)$$

Figure 4.8a shows the diameter of the cloud as observed through the horizontal imaging system and cloud density, averaged along the y -axis, as a function of flight time t . We fit Eq. 4.4 to the cloud width over time, shown in Fig. 4.8b and obtain a temperature of $37 \mu\text{K}$ after 1 ms of molasses cooling, well below the Doppler temperature of $126 \mu\text{K}$ for Cesium and above the recoil temperature of $0.2 \mu\text{K}$ [53].

A more detailed account of the whole imaging system and its design consideration is provided in a Diploma thesis carried during construction of the experimental apparatus [55].

4.3.4 Microwave spectroscopy for bias coil calibration

Some experiments that we considered required the ability to drive Microwave transitions in Cesium between the $6S_{1/2}$ hyperfine ground states with $F = 3$ and $F = 4$. Therefore, a microwave setup was constructed that expose the atoms to a 9.2 GHz microwave-frequency (MW) field. The setup was constructed as a Bachelor thesis project and is documented and tested thoroughly in [56]. Here, only a brief summary is provided that is necessary for understanding the calibration measurements below.

Setup

Figure 4.9 shows the signal chain employed for generating and controlling the final 9.2 GHz MW signal. The signal originates from a programmable vector signal generator (Keysight Technolo-

gies, EXG N5172B) that offers external frequency control via a Python-coded USB interface and outputs a 2.3 GHz signal with a power of 12 dBm. A reference frequency of 10 MHz, derived from an atomic reference, was provided to the signal generator for absolute frequency accuracy. The 2.3 GHz output was frequency doubled twice (MiniCircuits, ZX90-2-36-S+ and ZX90-2-50-S+) to achieve the final frequency. This doubling technique was used because the signal generator's highest output frequency is 3 GHz. Bandpass filters and amplification are included in the setup to clean the signal and operate within the power limit of the component. A voltage controlled attenuator (VCA) is used to control the power of the final MW signal. The power is monitored using a directional coupler where 5% of the power are split off and sent to a power detector. Finally, the MW signal is connected to a microwave horn antenna (L3Harris Narda-ATM, 90-441-6 and 90-251A-6) that points at the atomic cloud.

Zeeman splitting of the hyperfine ground state transition

Hyperfine transitions are extremely narrow, making them useful tools for high precision spectroscopy. Thus, driving the $6S_{1/2}, F = 3 \rightarrow 6S_{1/2}, F' = 4$ transition in Cesium allows us to measure the magnetic-field dependent energy-splitting between different m_F states within each F -manifold and thus to calibrate our magnetic coils. In the limit that the energy shift due to the magnetic field is much smaller than the hyperfine splitting, which holds very well for fields below 100 G, the Zeeman energy shift for a given state $|F, m_F\rangle$ is given by [53]

$$\Delta E_{|F, m_F\rangle} = \mu_B g_F m_F B, \quad (4.5)$$

where μ_B denotes Bohr's magneton, g_F is the hyperfine Landé factor, m_F is the magnetic quantum number and B is the magnetic field. Within an F -manifold m_F can take values from $-F$ to $+F$, i.e. there are 9 m_F states within $6S_{1/2}, F = 4$ and 7 within $6S_{1/2}, F = 3$. Angular momentum conservation limits the number of possible magnetic dipole transitions that can be addressed via a MW field such that $\Delta m_F = 0, \pm 1$.

Sequence

The experimental procedure for MW spectroscopy is as follows: We load the magneto-topical trap and switch off the repumper a few ms before the cooler, thus pumping the ensemble into the $6S_{1/2}, F = 3$ manifold. Now a few μs MW pulse is applied with variable frequency and sufficiently low power such that the excitation probability is low. If the MW field is resonant with a $F = 3, m_F \rightarrow F' = 4, m'_F = (m_F, m_F \pm 1)$ transition we have a maximum probability to transfer the atomic population to F', m'_F which we detect via absorption imaging on the $6S_{1/2}, F = 4 \rightarrow 6P_{3/2}, F' = 5$ transition. Therefore, the atom number on the absorption image is directly linked to resonantly driving a MW transition. We scan the MW frequency and observe well defined peaks that correspond to the above described MW transitions.

Microwave spectrum

Since the cloud is not spin polarized by the end of the optical pumping, i.e. the whole $F = 4$ manifold is measured in absorption imaging, a total of 15 transitions are possible. Figure 4.10a

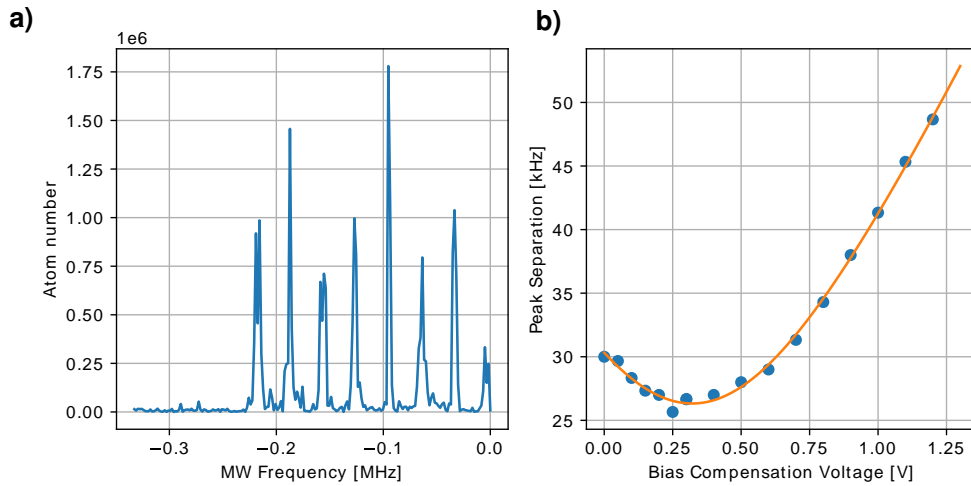


Figure 4.10: (a) Atom number in absorption image as function of MW detuning relative to 9.2 GHz indicating transitions between $F = 3$ and $F' = 4$ for different m_F states. (b) Averaged peak separation calculated from a) as function of Bias coil control voltage.

shows the observed atom number as a function of MW frequency. The spectrum covers only a frequency range with 7 peaks corresponding to 6 transitions with $F, m_F \rightarrow F', m'_F = m_F \pm 1$ transitions and the 'clock transition' (furthest to the right) $m_F = 0 \rightarrow m'_F = 0$ that, to first order, does not shift in a magnetic field. From the separation between the peaks we obtain the absolute magnetic field at the position of the atoms. We use this spectroscopy method to calibrate the fields generated by three pairs of compensation coils along the three dimensions. Calibration is done by varying the current through a given coil and recording the MW spectrum in order to extract the peak separation at this field. We repeat this for varying coil currents. Figure 4.10b exemplarily shows the recorded average peak separation as a function of the coil current control voltage. The splitting can be fitted by a hyperbola $\Delta_{\text{peak}}(f) = \sqrt{a^2(f - b)^2 + c}$, i.e. it scales approximately linearly with magnetic field in the region where the magnetic field of the respective bias coil is large compared to the magnetic field in the perpendicular directions. At the minimum it cancels the field along its axis and the splitting is given by the residual field in the other two spatial dimensions. Since we set the coil current via a control voltage the fit parameter a has the unit kHz/V. However, the current drivers in our experiment had a current output of $I = 2V_{\text{control}}$, i.e. we can directly infer the required current for a given magnetic field. Calibration is done for all three compensation coil pairs and we obtain $a_z = 4992$ kHz/V, $a_x = 198$ kHz/V, and $a_y = 47$ kHz/V for the z -, y - and x -axis compensation coils, respectively. The large differences in the values stem from the different number of coil windings where the axial coils are formed by 100 loops compared to one loop of the bias compensation coil. The three fits also determine the voltages for which the residual field at the MOT position is cancelled out. In this configuration, all hyperfine transitions occurred in a frequency range of 50 kHz, corresponding to a residual magnetic field of 0.02 G. This compensation coil configuration was used for all experiments in this thesis.

4.4 Optical setup for interfacing the nanofiber

Several fiber guided fields are required for trapping and probing atoms in the vicinity of the nanofiber with individual polarization control for each field. Recall from Sec. 2.2 that our trap configuration is based on a combination of a linearly polarized blue-detuned (and thus repulsive) running wave and a linearly polarized red-detuned (and thus attractive) standing wave at the waist of the nanofiber. The blue trap field polarization is orthogonal to the red trap field polarization to achieve stronger trap confinement in azimuthal direction. An overview of the optical setup to achieve this trap configuration and to probe the trapped ensemble is shown in Fig. 4.11. The depiction corresponds to the actual spatial layout on the optical table to make it more useful when aligning the setup. The layout couples red trap light to the nanofiber on both ends to achieve the standing wave. A $\lambda/2$ -waveplate controls the splitting ratio between both arms. A total of three automated shutters (Stanford Research Systems, SR470) are included in the setup to turn off both red trap fields and the blue trap field separately. Polarization control at the fiber waist is given through a $\lambda/4$ - and $\lambda/2$ -waveplate in each trap arm with the latter on an automated rotation mount. Probe light exiting the fiber is filtered from the trap fields with a Volume Bragg Grating (VBG), typically with 90% efficiency, and coupled to a fiber guiding it to one of the detection setups depending on the experiment. For squeezing experiments, for example, a homodyne detection setup was used. For previous second-order auto-correlation measurements single photon detection modules (SPCM) were used. A total of three probe light input ports are available, two for the D2-transition in Cesium at 852 nm and one for the D1 transition at 895 nm. For the photon transport experiments that are reported in this thesis only one port was used but there are several possible applications for additional resonant fiber guided fields, for example a fiber guided repumper or a control light field as is needed to realise λ -level schemes. The two 852 nm fields are superposed on a 50:50 beam splitter, and then superposed with the 895 nm field on a dichroic window which, at 8° incidence, reflects 852 nm light and transmits 895 nm light. The probe light propagates through the nanofiber in opposite direction to the blue trap light to reduce blue trap background in the probe field detection. The power of the red trap field is stabilised after the fiber outcoupler from the laser table using an AOM. The power of the blue trap field was stabilised similarly in earlier stages of the experiment until power limitations lead us to remove the AOM and rely on the inherent power stability of the blue trap laser. To check the power balance and fiber coupling stability of the two red trap fields their powers are monitored after transmission through the fiber by reflecting part of the beam onto a photo diode. We use an edged window for the beam sampling where the reflections from front and rear facet occur at different angles to avoid interference between them on the photo diode.

4.4.1 Polarization alignment

As the intensity distribution around the nanofiber depends strongly on polarization, the polarization of all three trap fields (two counter-propagating red-detuned trap fields and one blue-detuned trap field) has to be aligned at the nanofiber waist in order to form the desired trap potential. Our polarization alignment scheme relies on the fact that the nanofiber waist contains impurities that scatter light. In good approximation, this scattering is polarization maintaining and thus contains information on the polarization of the guided field at the waist. We collect the light scattered

coupling setup with linear polarization. The input polarization of every light field that is coupled into the nanofiber can be rotated via a $\lambda/2$ - and a $\lambda/4$ -waveplate. This also turns the polarization at the waist although it is generally modified due to birefringence of the fiber and taper section before the waist. This birefringence could be compensated in good approximation via the $\lambda/4$ -waveplate so that the field was linearly polarized at the waist. The $\lambda/4$ -waveplate angle was optimized for maximum contrast of the $\sin^2 \phi$ intensity pattern observed by the camera. Once compensation was achieved the $\lambda/2$ -waveplate was used to orient the angle of the linearly polarized mode at the waist to achieve the desired trap configuration. The procedure of measuring the contrast and aligning the polarization to the vertical or horizontal plane was automated in our experiment where a script reads out the camera and controls the $\lambda/2$ -waveplates via automated rotation mounts (Thorlabs, K10CR1/M). Contrast maximization via the $\lambda/4$ -waveplate is still done manually.

4.4.2 Ti:Sa probe laser

The D2 probe field in our experiment is derived from a Titanium:Sapphire (Ti:Sa) ring cavity laser, locked via a Cesium spectroscopy. Light in the spectroscopy arm is sent through an EOM that modulates side bands with a frequency difference of 10 MHz onto the field. The modulated field propagates through a Cesium vapour cell and is sent to a photo diode that is fast enough to observe the sidebands. The relative phase shift of the sidebands is extracted by mixing the phase-shifted photo diode signal with the 10 MHz RF signal that is sent to the EOM. This generates an error signal that is processed by the Ti:Sa control system that modulates elements in the Ti:Sa cavity to stabilise its output frequency. In the experiment, the laser is locked to the cross-over between the $6S_{1/2}, F = 4 \rightarrow 6P_{3/2}, F' = 3$ and $F' = 5$ transition that is 225 MHz red-detuned to the probing transition $6S_{1/2}, F = 4 \rightarrow 6P_{3/2}, F' = 5$. This offset is practical because a frequency shift of 225 MHz is easily achieved using an AOM in double pass configuration. While the Ti:Sa laser system requires more maintenance and table space compared to diode laser systems it comes with the advantage of high power output, large tunability and most importantly a significantly lower off-resonant background in the laser light compared, for example, to a diode laser. This means that our 852 nm probing field has very little frequency contamination which is important when investigating on-resonance transmission where the trapped ensemble renders the fiber almost opaque for the resonant probe field such that the fiber output has a substantial share of background light that distorts the measurement. Typically a few hundred microwatt are branched off from the Ti:Sa output for spectroscopy with the rest being fiber coupled and sent from the laser table to the experiment table. There, the light passes through a double-pass AOM configuration that shifts the frequency by 225 MHz and thus into resonance.

4.5 Experiment control

The various components of the experimental setup are controlled via a dedicated control computer (Jäger Messtechnik, ADwin Pro-II) featuring 3×8 analog and 32 digital output channels. The analog channels span voltages from -10 to 10 V with timing resolution of $3 \mu\text{s}$. Digital channels output 0 or 5 V with 10 ns timing resolution. The Python-based control software was

developed in our group and allows the timing of the experimental sequence. It is detailed in depth in the PhD thesis in Ref. [49]. The software also allows to interface additional devices in the lab if these can be accessed via a Python interface, for example signal generators or rotation mounts. An experimental sequence is started upon triggering from a 50 Hz trigger box, a device that outputs a trigger signal at a constant phase of the electric mains to improve reproducibility of the experiment.

4.6 Realisation of dipole trapping in the evanescent field

We discussed various aspects and requirements for a dipole trap in the evanescent field of the nanofiber. Before we detail the realisation we briefly summarize these aspects. The superposition of a repulsive, blue-detuned fiber guided field and an attractive, red-detuned field leads to a trapping potential approximately 200 nm above the surface of the nanofiber. The depth of the trap is on the order of $100 \mu\text{K}$, depending on the power of the trap fields. Atoms are accumulated at the nanofiber waist via a magneto-optical trap and then loaded into this the trap via an optical-molasses that dissipates the kinetic energy that atoms gain from the trap potential. In this section we explain the successive steps in more detail and demonstrate that atoms are trapped in the evanescent field of the nanofiber.

4.6.1 Trap loading

A experimental trapping sequence starts with loading the magneto-optical trap. The duration of the MOT phase is chosen depending on the desired optical depth of the trapped ensemble during the experiment. For the experiments in this thesis only a few hundred trapped atoms are necessary which was achieved already for 30 ms MOT loading duration. Reducing the loading time is beneficial as it allows for higher experiment repetition rates. MOT loading is followed by 40 ms of molasses cooling, where the MOT coil currents are switched off and the cooler detuning is increased to 70 MHz to minimize the final temperature of the atoms. The molasses duration and detuning are chosen to maximize the number of trapped atoms. The blue and red trap fields are switched on during the entire experimental sequence. Atoms accumulate in the dipole micro-traps during the molasses phase. At the end of the molasses cooling phase the cooler and repumper are switched off and the fiber-trapped atom ensemble can be probed.

4.6.2 Measuring optical depth

Detecting atoms in the evanescent field of the nanofiber can be done in several ways. The standard procedure in our experiment is detecting absorption of resonant, fiber guided probing light. Here, two different procedures were used with different advantages. The quickest way to detect atoms and extract the optical depth is to send a few ms long probing pulse through the fiber while scanning the frequency a few ten MHz around the transition frequency using an AOM. A single photon detection module (Excelitas, SPCM-AQRH-FC) measures the photon count rates at the nanofiber output. After the frequency sweep, the red trap power is switched off 1 ms to release the atoms from the trap in order to record a frequency sweep without absorption. Finally, the background count rate is measured and subtracted from the two pulses. In our

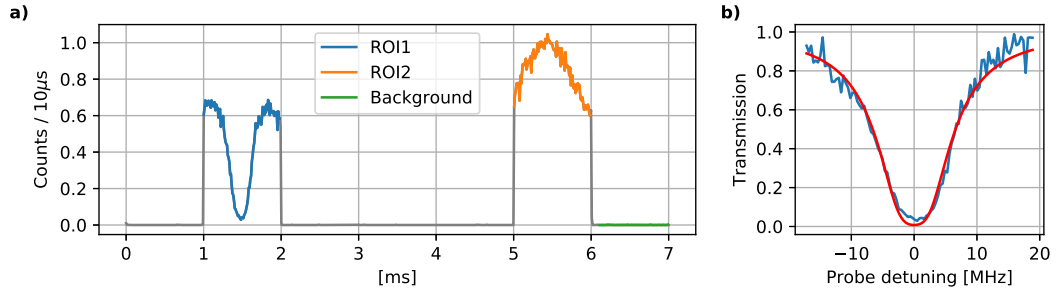


Figure 4.12: (a) SPCM clicks versus time as recorded by the FPGA, averaged for 500 runs. The probing frequency is swept over 36 MHz across resonance via an AOM. After the first probing pulse (ROI1), the red trap is switched off to release the atoms and we record a reference pulse (ROI2). The SPCM background is extracted from the end of the trace (b) Transmission versus AOM frequency, calculated from the ratio of ROI1 and ROI2. The fit function is given by Eq. 4.6 and yields an optical depth of 4.9 with a linewidth of 5.4 MHz.

experiment this is automated via a Python software ('SPCM Analyser') developed in our group. The software reads time stamps from the FPGA that record photon detection of the SPCM. A typical SPCM trace is shown in the left panel of Fig. 4.12. We extract the fiber transmission as a function of probe light frequency by calculating the ratio of the transmission during the two frequency sweeps. The result is fitted with the expected Lorentzian absorption profile to extract optical depth, center frequency and linewidth. The fit function is given by [7]

$$T(OD, \Delta) = \exp\left(\frac{-OD}{1 + \left(\frac{2\Delta}{\Gamma}\right)^2}\right), \quad (4.6)$$

where we assume the probe intensity to be far below saturation. Here, Γ is the atomic excited state linewidth, and $\Delta = \omega_0 - \omega$ is the detuning of the probe field with respect to the atomic transition with the center frequency ω_0 . In our experiment, we observe Cesium-characteristic absorption profiles at the expected frequency with a linewidth of 5.4 MHz, slightly above the free-space linewidth of Cesium (right panel of Fig.4.12). We attribute the linewidth broadening to trap induced light shifts of the transition frequency that vary from atom to atom depending on its position in the trap. Such light shifts occur despite our magic-wavelength trap configuration due to tensor light shifts of the excited state, as explained in Sec. 2.2.3.

The optical depth measurement described above is useful for most optimization procedures, for example when optimizing the trap powers or the overlap between MOT cloud and fiber because the extracted OD is reliably proportional to the number of interacting atoms. However, this procedure is not ideal for a precise measurement of the resonance frequency and the on-resonance optical depth for two reasons. Firstly, the frequency sweep has finite duration of typically 1 ms while the trap lifetime is on the order of 6 ms. The probing duration is determined by the requirement that the SPCM count rate is far above its background and the power in the fiber is far below saturation, meaning it cannot be shortened arbitrarily. This means that the OD changes due to atoms loss over the course of the frequency sweep. The result is an

asymmetric absorption profile, as is indeed apparent in the shown transmission curve. This shifts the center of the fit since the fit function is symmetric around resonance and thus leads to a shifted center frequency. Secondly, optical pumping during the frequency sweep changes the optical depth of the ensemble. For a probe field with circular polarization at the trap center, optical pumping transfers atoms to the outermost m_F states of the $F = 5$ hyperfine manifold where they scatter on the cycling transition, i.e. $F = 4, m_F = 4 \rightarrow F' = 5, m'_F = 5$ of the D2 line. This cycling transition is stronger than the transitions between other m_F states and thus the pumped ensemble has a higher optical depth. The consequence is that optical pumping changes the ensembles optical depth during the sweep, again leading to a change of absorption over the frequency sweep and thus to an asymmetric transmission profile. This could be solved by optically pumping the ensemble prior to the optical depth measurement. The drawback of this is that the optical pumping causes heating of the trapped ensemble.

In order to circumvent these limiting effects we typically probe the ensemble at a fixed frequency and only vary it from repetition to repetition. This allows to probe with shorter duration, such that probing occurs always at the same time during the sequence and the probe field always interacts with an ensemble with the same Zeeman state distribution and atom number for every pre-set frequency. The downside of this method is that many more experiment repetitions are necessary and it relies on the shot-to-shot stability of our experiment. Therefore, this method was only used when the exact frequency of the probing transition had to be determined whereas OD measurements, for example to maximize the number of trapped atoms, were carried out with the sweep technique.

4.6.3 Trap optimization

The probing techniques described above measure the optical depth from atoms in the evanescent field of the nanofiber. Since the MOT accumulates atoms around the nanofiber probe field absorption can originate both from atoms that freely propagate through the evanescent field and from atoms trapped in the micro-trap array above the fiber surface. Therefore, a Cesium-characteristic absorption profile is not a proof of trapped atoms. Such a proof can be obtained from varying the trap potential and showing that the optical depth reaches a maximum for the right choice of red and blue trap power. Generally, the trap potential depends on the intensity of the blue trap power. In the beginning of the experiment construction more blue trap power was available. At that time, we performed 2D scans of the blue and red trap power which showed a global OD maximum at blue trap powers around 20 mW. However, soon we suffered from limited blue trap laser power and from then on operated the trap at the maximum available blue trap power which stabilised at 13 mW coupled to the nanofiber. Therefore, we prove trapping by showing that the optical depth as function of the power of the red trap field has a well-defined peak. At too low red trap powers the repulsive blue trap field dominates and repels atoms from the fiber, thus preventing any atom trapping. If the red trap power is too high the repulsive potential barrier of the blue trap field is suppressed and atoms fall onto the fiber surface where they adsorb and lose the good spectral properties they possess in free space. This implies an optimum red trap power where the atom loading during the molasses phase is most effective. In Fig. 4.13a we plot the optical depth achieved after 100 ms of MOT loading, followed by 40 ms of

4. CONSTRUCTION OF A NANOFIBER-BASED DIPOLE TRAP

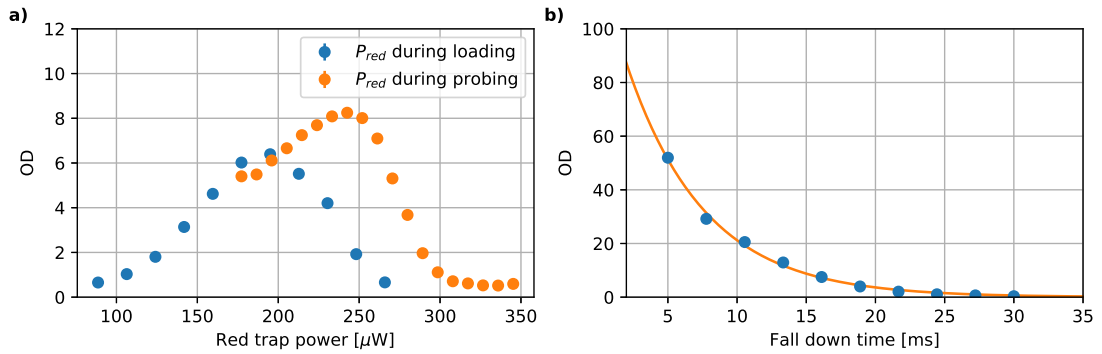


Figure 4.13: a) Optical depth from trapped atoms as function red trap power during loading (blue) and probing (orange) extracted via fitting the Lorentzian absorption profile with Eq. 4.6. The power is kept constant during probing and loading, respectively. The blue trap power was 13 mW for both curves. b) OD as function of delay between the end of the molasses phase and the probing stage. The exponential fit yields a trap lifetime of 5.6 ms.

molasses cooling as a function the power of the red trap field during loading from the molasses which peaks at $195 \mu\text{W}$ and thus proves that atoms are trapped by the nanofiber.

It can be beneficial to use different red trap powers for loading from the molasses and probing the atoms. The first red trap stage maximizes the loading efficiency into the trap and thus the number of trapped atoms. The second red trap stage reduces the distance from the trap minimum to the fiber surface and thus coupling strength to the probe field. This means that after loading the trap the red trap power is increased which pulls the atoms closer to the fiber. A plot of the optical depth as a function of the red trap power during probing is shown in Fig. 4.13a. The power change must be slow with respect to the trap frequencies of around 100 kHz such that the trap deformation is approximately adiabatic leading to negligible heating of the atom ensemble. In our experiment, the trap red trap power was thus ramped over the course of 1 ms. The power shifting allows us to disentangle the red trap effects on loading and coupling strength. The left panel of Fig. 4.13 shows both scans and illustrates that optimum loading occurs at a different red trap power than optimum coupling.

4.6.4 Trap Lifetime

A key figure that characterizes the nanofiber-based dipole trap is the trap lifetime, i.e. the time after which the atom number in the trap has decayed to $1/e \approx 0.3$. To this end, we measure OD for different delays between the molasses stage and the probing stage. Fig. 4.13 shows a typical lifetime measurement, fitted with an exponential decay $f(t) = f_0 \exp(-t/\tau)$. The fit yields a lifetime of $\tau = 5.6$ ms. The lifetimes measured in our experiment have varied both between different nanofibers installed in our vacuum chamber and over time for a given nanofiber. Trap lifetimes observed in our experiment ranged from more than 100 ms down to less than 10 ms. For the experiments reported in this work lifetime was around 6 ms. Generally, the trap lifetime seemed to decrease with time after placing a nanofiber in the vacuum chamber.

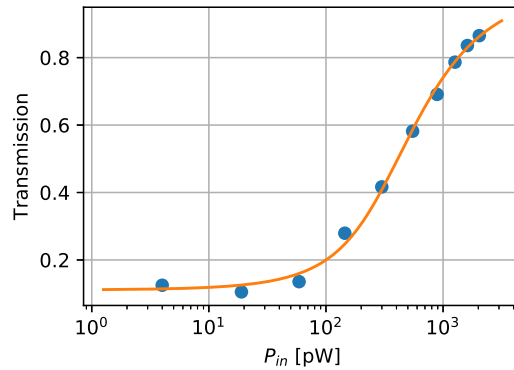


Figure 4.14: Saturation measurement to extract the coupling strength β . The trapped ensemble is exposed to different probing intensities and the transmission is measured as a function of probe power, yielding $\beta = 0.0070(5)$.

A possible explanation is that absorbers adsorbed to the fiber surface with time and caused increased absorption from the trap fields. This increases the temperature of the fiber which may lead to increased vibrations and thus increased atom heating.

The trap lifetime in our experiment is lower than the lifetime we obtain in the other nanofiber experiment in our group of typically 70 ms with maximum values of up to 150 ms. Currently, this large discrepancy is not well understood. One difference between the two setups is the smaller nanofiber radius in our experiment (200 nm compared to 250 nm) which may lead to worse mechanical stability of our nanofiber. Another difference are the trap wavelengths. In particular, our blue trap wavelength of 686 nm is further blue detuned from the probing transition than in the other nanofiber experiment that uses 780 nm as the blue-detuned field. The consequence is that we require higher blue trap power to achieve a comparable trap depth which leads to increased absorption from impurities and thus to a higher fiber temperature. This in turn leads to stronger thermal excitation of vibrational modes of the nanofiber which can couple to the vibrational modes of the trapped atoms and heat them out of the trap.

4.6.5 Measuring atom number and coupling strength

The previous paragraphs explained how we measure the optical depth of the trapped atomic ensemble. This OD is given by the product of the optical depth per atom and the number of trapped atoms. To determine these values we perform a saturation measurement where the atoms are exposed to increasingly higher intensities and their saturation is observed, i.e. we measure the transmitted light as a function of the input power. This allows us to extract both the coupling strength β and the number of trapped atoms N from the measurement. A typical measurement is shown in Fig. 4.14 where we plot the transmission of the ensemble as a function of input power.

To describe this process analytically we consider the the change of power in the light field along the fiber as the light propagates through the trapped ensemble. On resonance, each atom

scatters at the rate

$$R = \frac{\Gamma}{2} \frac{S}{1+S} \quad (4.7)$$

where we the saturation parameter $S = I/I_{\text{sat}}$ relates the intensity at the position of the atom to the saturation intensity $I_{\text{sat}} = \frac{\hbar\omega}{\sigma_0} \frac{\Gamma}{2}$. The change of power along the fiber due to scattering from trapped atoms is

$$\frac{dP}{dz} = -R\hbar\omega n(z) \quad (4.8)$$

where $n(z)$ is the atomic density along the fiber. Next, we introduce an effective area A that relates the power in the guided field to the intensity at the position of the atom via $P = AI$ and use the expressions for R , I_{sat} to rewrite Eq. 4.8 as

$$dP \left(1 + \frac{P}{P_{\text{sat}}} \right) \frac{1}{P} = -\frac{\sigma_0}{A} n(z) dz \quad (4.9)$$

Integrating both sides leads to

$$\int_{P_{\text{in}}}^{P_{\text{out}}} dP \left(\frac{1}{P} + \frac{1}{P_{\text{sat}}} \right) = - \int_0^L dz \frac{\sigma_0}{A} n(z) \quad (4.10)$$

Integrating the atom density over the length of the ensemble gives simply the total number of atoms, N , while the left side can be integrated and one obtains

$$\ln \frac{P_{\text{out}}}{P_{\text{in}}} + \frac{1}{P_{\text{sat}}} (P_{\text{out}} - P_{\text{in}}) = -\frac{\sigma_0}{A} N \quad (4.11)$$

Now we have an equation that relates transmission through the ensemble to input power, since $T = P_{\text{out}}/P_{\text{in}}$. Solving for T requires use of the Lambert W function, denoted with \mathcal{W} , and we obtain

$$T = \frac{\mathcal{W}(e^{\frac{\sigma_0}{A} N + \frac{P_{\text{in}}}{P_{\text{sat}}})}}{\frac{P_{\text{in}}}{P_{\text{sat}}}}. \quad (4.12)$$

This function can be fitted to the measured experimental data, an example of which is plotted in Fig. 4.14 using the total atom number and A as fitting parameter. Note that P_{sat} is a function of A and the exact relation can be found by considering Eq. 4.9 in the limit of $P \ll P_{\text{sat}}$. The equation then simplifies and we obtain

$$\frac{dP}{dz} = -\frac{\sigma_0}{A} n(z) P \quad (4.13)$$

which we can be integrated easily such that

$$P_{\text{out}} = P_{\text{in}} e^{-\frac{\sigma_0}{A} N} \quad (4.14)$$

Here, the exponent has the function of the optical depth (OD) of the ensemble which relates to the coupling strength according to $\beta = \text{OD}/4N$. There, we can derive β from A via

$$\beta = \frac{\sigma_0}{4A} \quad (4.15)$$

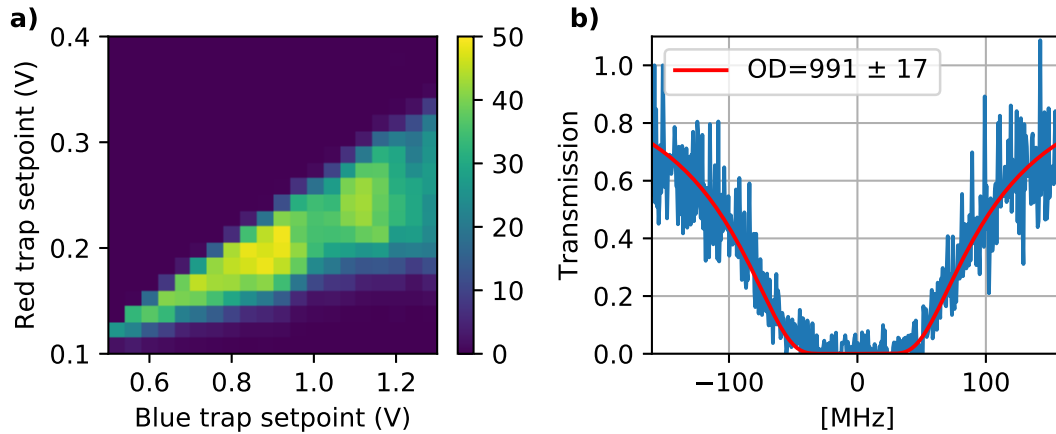


Figure 4.15: a) Optical depth as function of red and blue trap power stabilisation setpoint. The plot shows a global maximum OD and illustrates the interplay between red and blue trap power. b) Transmission of the nanofiber as a function of probing frequency, showing the highest optical depth achieved in our experiment.

With this relation we can also calculate the saturation power P_{sat} since

$$P_{sat} = AI_{sat} = \hbar\omega \frac{\Gamma}{8\beta}. \quad (4.16)$$

These calculations can be combined to obtain $T = T(\beta, N)$ such that we obtain for the measurement in Fig. 4.14 the values $\beta = 0.0070(5)$ and $N = 79 \pm 3$. The value of β leads to $P_{sat} = 136$ pW. This value will be our reference for input powers in Chapter 5.

4.7 Optimizing the optical depth

One early experimental goal was to significantly increase the number of trapped atoms compared to previous trap realisations and ODs beyond 1000. High ODs are crucial to many experimental quantum memory schemes, where a photon is stored as a collective excitation of the trapped atomic ensemble, scale beneficially with optical depth. Therefore, considerable time was spent on optimizing the number of trapped atoms and thus the OD. In principle, the nanofiber has approximately 4 trapping sites per micrometer length, assuming a red-trap wavelength of 935 nm, and thus a 10 mm long nanofiber has ~ 40.000 trapping sites. Due to the collisional blockade effect one can reach a maximum filling factor of 50% [33]. This implies a theoretical upper limit for the number of trapped atoms of 20.000. The coupling of trapped atoms to fiber guided fields can be optimized via the trap geometry and the optical depth from a single trapped atom can exceed 0.1 [57]. This implies a maximally attainable OD of 2000. In this section we report experimental results of optical depths around 1000.

In order to maximize the number of trapped atoms and the optical depth per atom we found the following points to be critical:

- **Optimum trap power:** Both the red- and the blue-trap must be optimized for loading the maximum number of atoms during the molasses phase. This is achieved best in a 2D scan since the trapping potential depends on both parameters. An exemplary 2D scan is shown in Fig. 4.15a where the mutual dependence of the red and blue trap power for trap loading efficiency is apparent. Importantly, the plot shows a global maximum of optical depth that marks the point of optimum trap loading. As noted in Sec. 4.6.3 and maximum OD/atom occur for different trap shapes. Therefore, the trap configuration during probing has to be optimized for maximum optical depth in a separate 2D scan.
- **Optimum overlap between MOT and nanofiber:** Both the position and the shape of the MOT cloud can be adjusted to maximize the number of atoms close to the nanofiber waist during molasses cooling and thus the number of trapped atoms. Through the fiber mount the x- and y-position of the fiber can be optimized relative to the atom cloud and the z-position of the cloud can be adjusted via the magnetic compensation coil. The cloud shape can be altered by adding a quadrupole-field onto the magnetic field provided by the MOT coils which stretches the cloud along the fiber while increasing the confinement in the transverse direction. However, this stretched MOT-configuration is less efficient to load atoms from the background and loading saturates for a smaller atom number. Therefore, we design the sequence with separate MOT loading and reshaping stage. After loading the MOT until the number of atoms has saturated we switch the magnetic field configuration for around 100 ms to the configuration that achieves better overlap. This reshapes the cloud while keeping losses due to a reduced trap volume minimally.
- **Minimize spectral broadening of the trapped ensemble:** To translate a high number of trapped atoms into a high OD it is necessary that all atoms are resonant at the same frequency, i.e. that the ensemble is not broadened from spatially varying light shifts in the trap. This motivated the use of magic wavelengths in our experiment.
- **Mechanical stability:** Trapping was substantially harmed when the nanofiber was excited mechanically, for example by working on the vacuum chamber. The optical table was floated to reduce mechanical excitation via the floor.

Optimizing all of the above aspects lead to a maximum measured optical depth of almost 1000, as is shown in Fig. 4.15b. In this measurement, the MOT was loaded for 2 s, followed by cloud reshaping, atom loading, and trap reshaping. The trap lifetime was 75 ms. Unfortunately, this high optical depth could not be maintained for more than a week. Then the maximally attainable OD reduced to around 200 while trap lifetime reduced to around 10 ms. The reason for this substantial reduction is not clear. We suspected that the nanofiber was damaged, possibly from the heating due to absorption of the trap lasers, and decided to exchange it with a newly pulled nanofiber of the same dimensions. After recovering the previous trapping procedure the maximum OD was 200 while lifetime was 30 ms. The lifetime degraded further over the course of the following weeks. A range of possible causes for the unstable trapping were investigated:

- **Trap laser power noise:** We recorded power spectra of all trap lasers to check that no particular noise features existed at frequencies around the trap frequency, typically around

100 kHz, but nothing suspicious was observed. Still, both the red and the blue trap fields were exchanged with 1064 nm and 780 nm respectively, yielding no notable improvement.

- Acoustic noise in the laboratory: A range of fans and the air-conditioning caused an overall noise floor in the lab. Both the level of noise was reduced as much as possible and the sound insulation was increased by glueing sound-absorbing foam under the experiment rack that forms the ceiling of the experiment optical table, even though it remains unclear if this insulation had any notable effect.
- Vary position of the nanofiber holder: One hypothesis suggested that the translatable nanofiber holder has positions that are mechanically more stable than other positions, possibly because the screws in the mechanical feedthroughs are more stable in some positions than in others. No improvement was found.
- Switch the trapping plane: The trapping plane was rotated by 90° to test if this affects the trap lifetime. It was surmised that the nanofiber might vibrate more in flexural modes in the vertical plane than the horizontal plane or vice versa. However, no improvement was observed.
- Heating from a nearby quadrupole-transition: The ground state of Cesium can be excited via a quadrupole-transition close to the blue trapping wavelength of 685 nm [58]. This transition is extremely narrow and weak such that small detunings already reduce scattering to negligible rates. To avoid the unlucky scenario that the blue trap laser was accidentally on resonance with this transition it was shifted by 0.1 nm. No lifetime improvement resulted from this.

In order to understand if any deformations or even chemical reactions occur at the waist of the nanofiber a sample of a fiber that was used in our apparatus for several months was studied with an scanning electron microscope (SEM). This revealed peculiar structures at various positions along the nanofiber and the taper. Examples are shown in the appendix App. B. However, it seems unlikely that the observed structures were present on the nanofiber waist while it was under vacuum because the high nanofiber temperature would cause them to evaporate. It seems more likely that these structures formed during flooding of the chamber with ambient air, which causes the elementary Cesium adsorbed to surfaces to oxidize. Indeed, X-ray spectroscopy of these structures suggests that they consisted of Cesium-Oxide (see App. B for a more detailed discussion).

Since we could not resolve the cause of the OD reduction it was decided to turn to experiments that require more modest ODs of less than 10 which were attainable at all times.

4.8 Summary

A nanofiber based dipole trap for laser cooled Cesium was constructed and the experimental apparatus characterized in various aspects. We implemented a scheme for measuring the atom number in the MOT and in the nanofiber trap. Spectroscopy confirms that Cesium atoms are interfaced with fiber guided light and the dependence of optical depth on the power of the red trap

4. CONSTRUCTION OF A NANOFIBER-BASED DIPOLE TRAP

shows that the atoms are trapped. Our measurements show that we can routinely trap ensembles of a few thousand atoms with an optical depth around 100 and we realised a maximum optical depth of ~ 1000 .

Observation of Squeezed Light

Equipped with a theoretical framework of squeezed light and non-linear photon transport, and an overview over the experimental apparatus to study these phenomena, we now turn to the specific experiments to study the light after it interacted with an ensemble of trapped atoms.

The probing routines described in Ch.4 were practical for the optimization and characterization of the nanofiber-based dipole trap but in order to experimentally access the quadratures and their variance the probing had to be modified. Therefore, before turning to the experimental procedure and observed results we describe the homodyne detection setup.

5.1 Experimental Setup

For the experimental observation of squeezed light we recall the result from Sec. 3.2 where we showed for the balanced detector output in a homodyne detection scheme that

$$I_\theta \propto \alpha X_\theta, \quad (5.1)$$

meaning that the balanced detector output I_θ is proportional to the angle-dependent signal quadrature X_θ which is amplified by the strength of the coherent local oscillator, α . With this in mind we turn to the realisation of the homodyne detection setup.

5.1.1 Probing Setup

Resonant light from the Ti:Sa is split into a strong local oscillator field and a weak probing field on a non-polarizing 90:10 beam splitter. The LO arm is fiber coupled for spatial filtering and sent to the homodyne setup discussed in detail below. The probing field (signal) passes through two phase-stable AOM double pass setups that shift the light up and down in frequency. Phase stability is ensured by deriving the AOM RF frequency from the same digital function generator (Rigol, DG4162). The amplitude of one AOM is controlled via an analog modulation input and thus provides signal amplitude control. The modulation input for the other signal generator channel is used to shifts the output frequency digitally between to programmed frequencies.

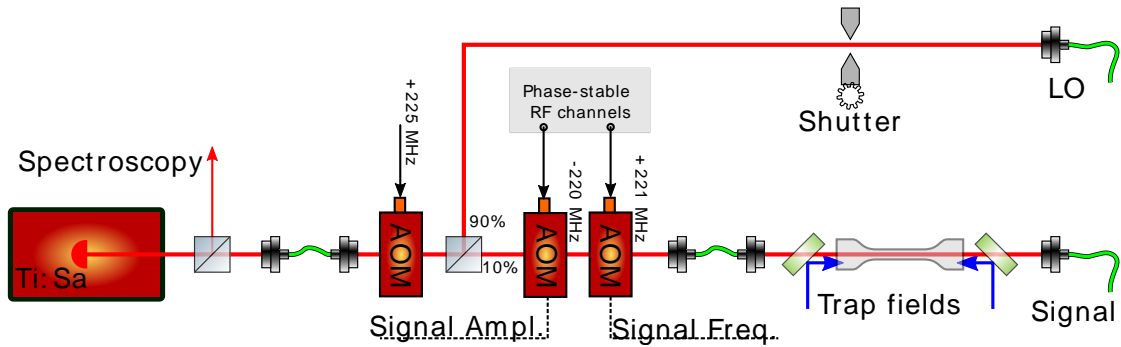


Figure 5.1: Probe setup for homodyne detection. Resonant light from Ti:Sa laser is split on a 90:10 NPBS to be used as phase-stable local oscillator (LO). The 10% output of the NPBS passes through two AOMs to be shifted in total by small frequencies of typically 1 MHz. The AOMs are driven from the same digital frequency generator where the outputs are phase stable and thus no phase noise is added to the signal relative to the LO. After frequency shifting the light is injected into the nanofiber coupling setup from Fig.4.11, filtered from the trap fields after propagating through the nanofiber, and sent to the other input of the homodyne detection setup.

This digital switching ensures that no analog noise is added to the channel frequency and phase stability between the outputs is maintained. Lastly, the light is fiber coupled and sent to the nanofiber coupling setup detailed in Sec. 4.4. Here, it is overlapped with the trap fields, injected into the nanofiber, filtered from the trap fields at the nanofiber output, and fiber coupled once again to be sent to the homodyne detection setup.

5.1.2 Homodyne Detection Setup

The signal light, extracted from the nanofiber, and the local oscillator light, derived in the probing setup, are injected into the homodyne detection setup shown in Fig. 5.2. The signal light passes through an optical isolator since we observed LO reflections from the setup that propagated to the nanofiber waist where it heated the trapped ensemble. After the optical isolator the signal interferes with the local oscillator field on a 50:50 non-polarizing beam splitter (NPBS, Thorlabs BS005). Polarization mode matching is ensured through polarization optics in the signal and LO arm prior to the NPBS. Both NPBS outputs reflect on a subsequent polarizing beam splitters (PBS) to filter the polarization matched component of the combined signal- and LO-field. The transmission of one PBS is coupled to a single-mode (SM) fiber. We optimize the spatial mode matching by optimizing the coupling of signal and LO field into the SM fiber. When not used for optimizing mode matching the SM fiber is connected to an SPCM such that a standard transmission measurement through the nanofiber can be done. To prevent damaging the SPCM we place a mechanical shutter in the LO arm. The signal polarization can be flipped via a $\lambda/2$ -waveplate on a flip mount before the PBS to select between sending the signal light to the homodyne detector or to the SPCM. Permanent $\lambda/2$ -waveplates after the NPBS are aligned such that a maximum share of the signal field is reflected and incident on the balanced detector. The PBS serve an additional purpose of optically isolating the nanofiber from LO reflections

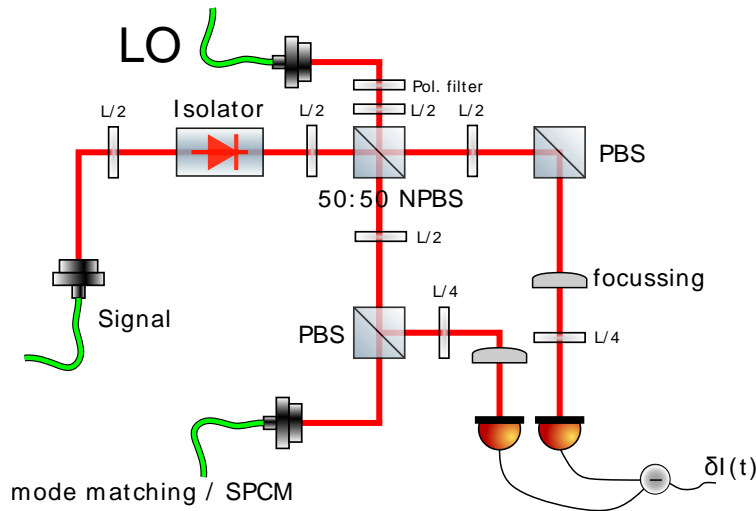


Figure 5.2: Homodyne detection setup. The signal field originating from the nanofiber interferes with the phase stable local oscillator (LO) derived from the same original laser on a non-polarizing beam splitter (NPBS). An optical isolator is included to prevent back-reflection of the strong LO field into the nanofiber. Mode matching between signal and LO is achieved by coupling both fields to the same single-mode fiber ("mode matching" fiber). Polarization mode matching is achieved by reflecting the two NPBS outputs from polarizing beam splitters (PBS). Additional optical isolation of the LO is achieved by $\lambda/4$ -waveplates before the balanced detector that ensure that reflections are transmitted through the PBS'. The focussing lenses are positioned to prevent beam clipping on the photo diodes while also not focussing the light to prevent local saturation of the diode.

since we place $\lambda/4$ -waveplates after them, aligned such that the LO reflection from the detector transmits through the PBS. Lastly, lenses ensure that the beams are not clipped on the photo diode but also not focused which could introduce noise from alignment drifts if the photo diode is locally saturated or varies in sensitivity.

5.1.3 Detection losses

Analysing the light exiting the nanofiber requires high detection efficiency since losses are equivalent to inserting undesired noise into the system. The resonant 852 nm light has to be separated from the the trap light fields, coarsely indicated in the probing setup description of Sec. 5.1.1, but actually done via the Volume Bragg Grating (VBG) mentioned in the more detailed nanofiber coupling setup description in Sec. 4.4. More than 90% of the resonant light incident on the VBG are reflected at an angle of 8° where a d-shaped mirror reflects it towards a fiber coupler. Since the light has a good Gaussian mode profile shortly after exiting the nanofiber it can be coupled with almost 90% efficiency into the fiber which guides it towards the homodyne detection setup. Further losses occur here from the optical isolator (10%) and improper mode matching to the local oscillator field. The mode matching is achieved by coupling both fields to the same single

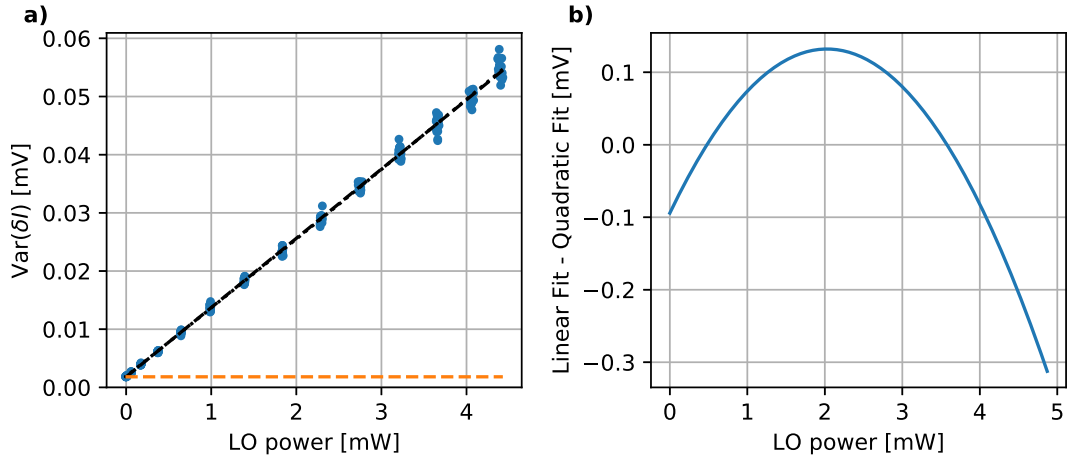


Figure 5.3: a) Variance of the balanced detector output as a function of local oscillator power. The linear fit intersection with the y -axis indicates the inherent electronic noise of the detector. b) Difference between a linear and a quadratic fit for the data in a). The maximum indicates the point of maximum detector linearity, at 2.03 mW.

mode fiber, as indicated in Fig. 5.2, and typically coupling efficiencies of 90% can be achieved for both fields. Finally, the photo diodes of the detector have a detection efficiency of 80% at 852 nm. The total collection efficiency of probe light on the balanced detector can be measured straightforwardly by measuring the nanofiber output power and comparing it to the sum of the powers at the two photo diodes which leads to 60%. To estimate the total detection efficiency we multiply this value with the mode matching efficiency, estimated from the product of the signal and LO fiber coupling efficiencies, and the photo diode efficiency, leading to a value of

$$\eta = \eta_{\text{collection}} \eta_{\text{modematching}} \eta_{\text{PD}} = 0.6 \times 0.9^2 \times 0.8 = 0.39 \quad (5.2)$$

This detection efficiency affects the measured squeezing amplitude as described in Sec. 3.2.1. For the total detection efficiency we have to include the electronic noise of the detector, which is described below.

5.2 Balanced Detector Calibration

Balanced detection in our experiment uses a device purchased from the University of Basel (SP1'023, [59]) where the photo diode difference current is amplified with low noise and a bandwidth of 50 MHz. Individual photo diode currents are accessible with up to 1 MHz bandwidth as the voltage drop across the individual photo diodes is available as a monitoring output from the device. For our measurements the balanced detector should be operated at maximum linearity which determines the optimum local oscillator power. This value is found via the following calibration measurement.

We block the signal input side of the beam splitter and vary the local oscillator power. Figure 5.3a shows the variance of the detector output calculated in the frequency range from 3 to 20 MHz as a function of LO power incident on the two photo diodes. This frequency range is the same as used for data analysis later. We record the detector output for a range of LO powers together with a monitoring output that is proportional to the intensity on one of the two photo diodes. From the latter trace we extract the LO power via the calibration factor of 1.95 mW/V and compare it to the variance of δI . We fit the data with a linear function to obtain the inherent electronic detector noise from the y -axis intersection of the fit. Comparing this value with the variance at the LO power used in a particular experiment gives the signal to noise ratio of this measurement.

In order to find the optimum LO power we fit the data with a linear and a quadratic function and plot the difference between the two fits in Fig. 5.3b. The maximum of this difference corresponds to the point of maximum detector linearity at 2.03 mW, the LO power used in the experiments presented below. Electronic noise in homodyne detection has the same effect as optical losses [60], i.e. it reduces the detection efficiency. The calibration measurement shows that at the selected LO power the electronic noise of the detector amounts to a reduction in detection efficiency of 7%. The overall detection efficiency is then $\eta_{\text{tot}} = 36\%$.

5.3 Experimental sequence and data acquisition

The first step in our homodyning sequence is to trap atoms around the nanofiber as detailed in Sec. 4.6.1. Once the atomic ensemble is ready for probing it is exposed to a resonant signal field of well defined and SPCM-calibrated power, typically with tens of picowatt guided in the nanofiber. The probe power is calibrated via the SPCM countrate of the fiber output with detection losses taken into account.

5.3.1 Stages of the sequence

The signal field is switched on via the signal amplitude AOM and kept at this level for 200 μs . After this homodyning stage the atoms are released from the trap by switching the red trap power to zero and the signal power is increased to the maximum attainable via the amplitude signal AOM. Then we switch the signal frequency by 1 MHz via the corresponding AOM to record the beat note between the signal and the local oscillator. The beat note will later be used to extract the relative phase between signal and LO during the homodyning. After the heterodyning stage the signal is switched off and the vacuum signal is recorded as reference, i.e. the output of the detector when no signal field is incident but only local oscillator. After recording the vacuum reference the LO is switched off and the electronic noise is recorded for 50 μs . This last part of the trace can be used to infer the signal to noise ratio of a particular trace by comparing the variances during the vacuum homodyning and during the dark detector stage.

5.3.2 Atom number estimate

In order to study the dependence of the spectrum on atom number N and compare it to theoretical simulations we need to extract N from the transmission measured when calibrating a

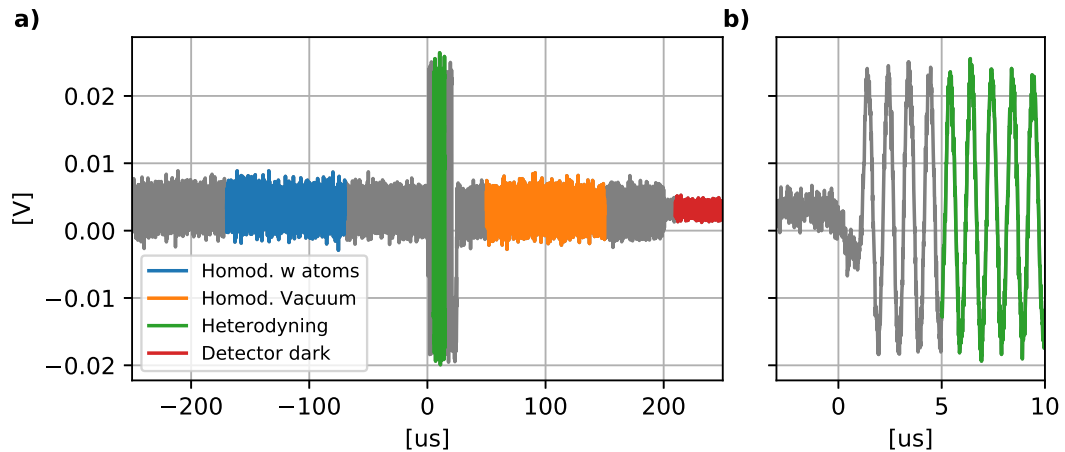


Figure 5.4: a) Typical experiment trace recorded on the oscilloscope with the various regions of interest indicated. The phase θ between signal and local oscillator is extracted via the starting phase of the oscillation during the heterodyning stage. All fields are switched off at the end of the sequence to record the dark detector signal from which the signal-to-noise ratio during the rest of the trace is extracted. b) Zoom onto the beginning of the heterodyning stage from which the signal phase θ is extracted.

homodyne measurement. In principle, the best way to do this would be a saturation measurement as described in Sec.4.6.5 prior to every homodyne measurement. This was, however, not practical for us as it requires modifying the detection setup with neutral density filters and thus takes considerable time and poses the risk of accidentally misaligning the setup which may spoil the detection efficiency. Therefore, we characterise the ensemble simply through measuring the optical depth at a given probe power prior to starting the homodyne measurement. The measured OD is discounted with saturation effects via $OD_{\text{eff}} = OD_{\text{unsaturated}} / (1 + S_0)$. From the unsaturated OD we calculate the atom number via the coupling strength according to $N = OD / (4\beta)$ which follows from our definition of β and is explained in Sec.4.6.5. We note that measurement errors in the coupling strength thus affect all values of N that are given below. Trapping with the nanofiber appeared stable over the time where the measurements in this thesis were taken and thus the coupling strength is assumed to be stable. However, this was checked only sporadically and thus fluctuating β -values cannot be ruled out.

5.4 Trace analysis

The balanced detector output during the experimental sequence is recorded on a digital oscilloscope (Teledyne Lecroy, HDO4054A, setup details in App.C.1) and stored for every trace. An example trace, is shown in Fig. 5.4 where the regions of interest (ROI), i.e. the atom homodyning, the heterodyning for phase extraction and the vacuum homodyning are marked. The right

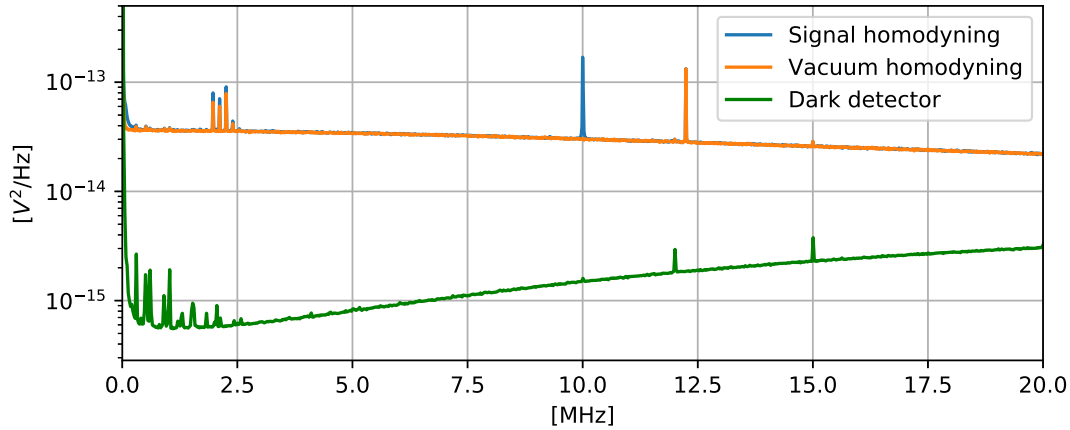


Figure 5.5: Averaged detector power spectra during the ROIs marked in Fig.5.4. a) For the homodyning and vacuum ROI. The origin of the 10MHz peak in the signal spectrum could not be resolved and the peak was masked for variance calculations. The peak was present with and without atoms surrounding the nanofiber and thus seems to be a technical artefact. b) Dark detector, reflecting the noise characteristics of the balanced detector circuit.

panel of Fig. 5.4 shows a zoom of the beginning of the heterodyning stage where a buffer of $5 \mu\text{s}$ is kept to allow the signal power to rise. For the phase extraction we assume that the phase of the beat note is the same phase as during the homodyning modulo a stable offset. We confirm independently that the interferometer composed of the signal path and the local oscillator path has negligible path length variations within the experiment duration.

5.4.1 Detector spectra

From the ROIs in the example trace in Fig.5.4 we can calculate the respective power spectrum by taking the square of the absolute value of the complex fourier analysis. Since we record the detector output δI at N discrete points in time we calculate the complex discrete Fourier transform by

$$\delta \tilde{I}_\omega = \sum_{n=1}^{N-1} \delta I e^{-i \frac{2\pi}{N} \omega n} \quad (5.3)$$

To obtain the averaged power spectrum we calculate the mean of the absolute squares. Figure 5.5 shows these respective spectra averaged for a squeezing measurement containing 50k traces. The dark detector spectrum reflects the noise characteristics of the balanced detector circuit and shows that, apart from a few peaks, it is least noisy for ~ 2 MHz. The other two spectra show a raised noise floor due to the shot noise of LO field. Several spikes are visible in the spectra of the illuminated balanced detector. The fact that all these spikes, with the exception of one at 10 MHz, are visible in both spectra indicates that they stem from technical noise in the detection setup or in the LO power spectrum and are unrelated to the fiber trapped atoms. Therefore, they

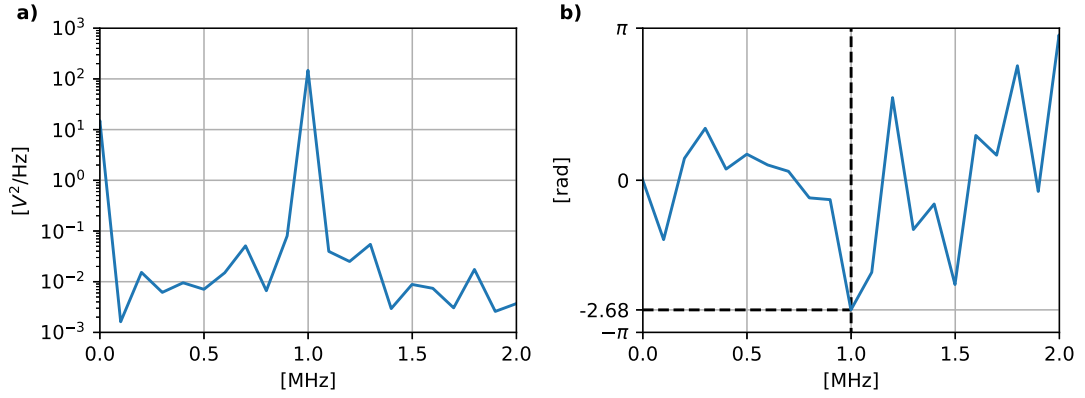


Figure 5.6: a) Exemplary power spectrum during heterodyning with the beat note between the signal and the LO at 1 MHz. b) Phase spectrum corresponding to a) from which the phase θ at the beat note frequency is extracted.

are masked before extracting the variance from the spectra. Masking is done by overwriting 10 frequency bins around a peak, corresponding to a window width of 100 kHz, with the values of the adjacent 10 bins. The 10 MHz peak, present only in the signal spectrum, is of unclear origin and has considerable amplitude. However, it is also present when no atoms are trapped and therefore is technical noise from some component of the nanofiber coupling setup. A possible explanation is that it originates from the two AOMs that switch the frequency and the amplitude of the signal.

5.4.2 Phase extraction

In order to extract the relative phase between signal and LO during the homodyning stage we calculate the spectrum in the heterodyning ROI, as shown in Fig.5.6. The heterodyning length of the ROI has to be chosen such that the discrete fourier analysis includes the beat note frequency of 1 MHz. This can be achieved if the length is an integer of beat note periods, in our case we chose $10 \mu\text{s}$. The phase of the beat note is obtained from the complex fourier transform of δI according to Eq. (5.3). The resulting phase array is shown in the lower plot in Fig. 5.6 with a line marking the phase of the 1 MHz beat note. This analysis is carried out for every single trace to correlate it with the signal variance.

5.4.3 Variance extraction

The variance of any series of N data points is defined as

$$(\Delta X)^2 = \frac{1}{N} \sum_i x_i^2 - \mu^2 \quad (5.4)$$

where μ is the arithmetic mean of X . However, from the spectra in Fig. 5.5 it is clear that there is noise in the system that is of no physical interest, even with the 20 MHz low pass filter

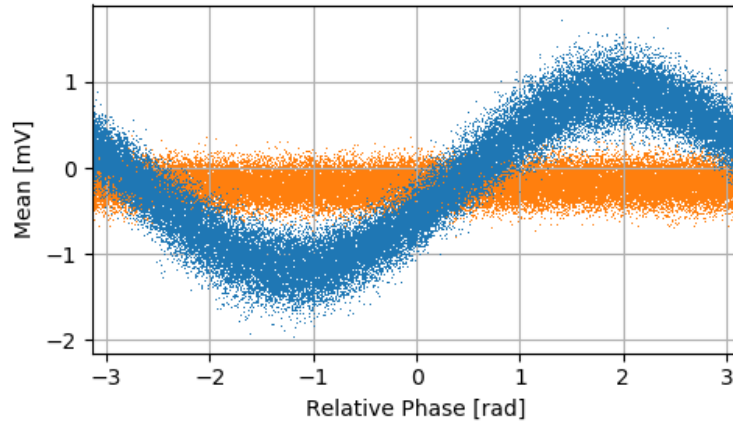


Figure 5.7: Mean detector output $\bar{\delta I}$ in the signal- (orange) and vacuum-ROI (blue) versus relative phase extracted from the heterodyning beat note for a data set including 50.000 files. Each data point corresponds to one execution of the sequence. The signal field power was 0.4 pW, amplified with 2 mW local oscillator field.

of the oscilloscope. This is especially true at frequencies below 1 MHz where, among others, LO intensity noise, nanofiber vibrations, atom loss during probing can superpose the physical signal of interest. To this end the trace could be filtered digitally with a bandpass filter before calculating its variance. A more straightforward way, however, makes use of Parseval's theorem which relates the square of a function to the square of the integral over its Fourier transform. This means we can calculate the signal variance directly from the spectrum by integrating its absolute square. For a discrete spectrum this results in

$$(\Delta\delta I)^2 = \frac{1}{N^2} \sum_{\omega_{\min}}^{\omega_{\max}} |\tilde{\delta I}(\omega)|^2, \quad (5.5)$$

where N is the number of frequency bins and $\tilde{\delta I}(\omega)$ is the discrete Fourier transform of the detector output $\delta I(t)$. This is a very useful relation with the advantage that we can calculate this for any frequency range of interest and no digital filtering with possible undesired filter features is necessary. It also allows us to filter out detrimental peaks, for example the previously mentioned 10 MHz feature. Therefore, the squeezing analysis throughout this work is done by first binning the spectra according to θ and subsequently extracting the variance for the desired frequency range.

5.4.4 Signal field amplitude

Extracting the phase of every trace allows us to plot the electric field of the signal and the vacuum with respect to phase by calculating the mean detector signal in each ROI, shown in Fig.5.7. Even though the trace itself shows no notable difference in the signal ROI and the vacuum ROI

we have in fact an extremely weak field incident during the signal ROI whereas only phase-less vacuum is incident on the homodyning NPBS during the vacuum ROI. Note that the power of the signal field was only 0.4 pW in this measurement, corresponding to ~ 320 photons over the duration of the region of interest. This illustrates the great sensitivity of homodyne detection despite using normal photo diodes.

5.5 Observation of squeezed light

The previous section detailed how the traces recorded by the oscilloscope are processed such that for every trace we extract the LO phase and the corresponding spectra used for variance calculation. In Sec. 3.2 we show that the variance of the balanced detector output is directly proportional to the quadrature variance. Therefore, squeezed light can be observed by calculating the ratio of the signal variance and the vacuum variance as a function of LO phase θ , that is

$$Q_\theta = \frac{(\Delta X_\theta^{\text{signal}})^2}{(\Delta X_\theta^{\text{vacuum}})^2}, \quad (5.6)$$

and we take $Q < 1$ as the signature of squeezing.

For a squeezing measurement we typically record 50,000 traces, sort them according to θ into 15 bins, and calculate the average spectrum for each θ . Averaging is necessary because the squeezing signal is too weak to be observable in a single shot. To observe squeezing we trap an ensemble of ~ 100 atoms around the nanofiber. The variance is evaluated in the frequency range from 3 to 20 MHz to exclude the low frequency peaks visible in the spectrum in Fig. 5.5 and generally low frequency technical noise. The upper limit covers almost four natural linewidths and is sufficient to capture the atom related physics as discussed in Sec. 3.3. As seen from the dark detector spectra the signal to noise ratio decreases with increasing frequency and thus the upper limit has the additional benefit of excluding high frequency detector noise. More discussion of the spectral characteristics is given in Sec. 5.8. Figure 5.8a shows Q binned for relative LO phase θ for a probing power of $P_{\text{in}} = 91$ pW. The variance ratio Q shows a characteristic $\cos(2\theta)$ modulation, i.e. indicates that the light from the signal field is squeezed with a lowest Q_θ that is 0.64% below 1. The data is fitted with a function given by

$$Q(\theta) = a_0 + a_1 \cos(2\theta + \theta_0^{\text{sig}}), \quad (5.7)$$

from which we extract the squeezing phase θ_{min} for which Q has the lowest value. The squeezing strength is extracted from Q directly.

Figure 5.8b shows the phase-resolved mean output $\bar{\delta I}$ of the balanced detector output during the respective ROIs. The data is fitted with a sine function given by

$$\bar{\delta I}(\theta) = a_0 - a_1 \sin(\theta + \theta_0^{\text{LO}}) \quad (5.8)$$

from which we extract the phase of the electric field that corresponds to a given squeezing phase. This allows us to compare the phase of the variance modulation to the phase of the electric field. The variance reflected by Q_θ is lowest when the electric field amplitude is maximized. This means that the output field, in the case of a resonant drive, is amplitude squeezed.

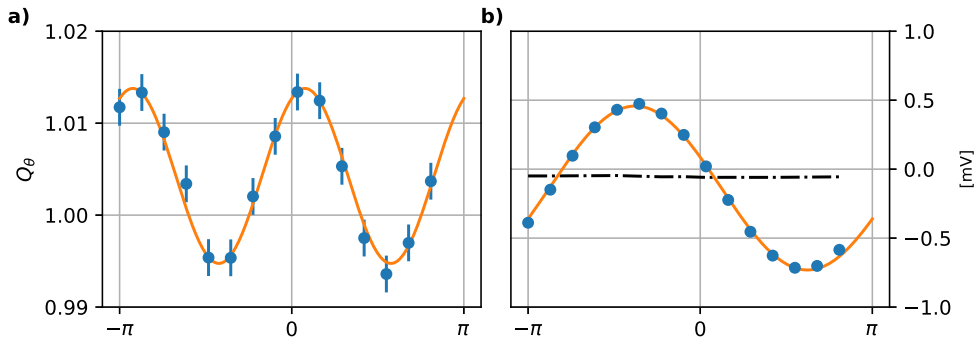


Figure 5.8: a) Averaged ratio Q_θ of the signal variance and the vacuum variance as a function of θ . The error bars are standard deviations of the averaged ratios. b) Offset-corrected mean of the balanced detector output as function of θ during the signal incidence and the vacuum reference measurement. This signal is directly proportional to the electric field of the signal input.

5.6 Detuned probing

The optical non-linearity investigated in this chapter strongly depends on the frequency of the probe field. In this section we show how finite detuning alters the phase of maximum squeezing while simultaneously the squeezing amplitude reduces.

We perform squeezing measurements as described above with varying detuning and for 50 pW input power, i.e. $P_{\text{in}}/P_{\text{out}} = 0.35$. The data sets are analysed according to phase and variance and we extract the phase of strongest squeezing via fitting the $\cos(2\theta)$ modulation of Q . Similarly, we extract the phase ϕ_E of the electric field amplitude and calculate the relative phase of maximum squeezing via $\phi_{\text{max}} = \phi_E - \theta$. The result is shown in Fig.5.9a. The data shows dispersive behaviour around resonance. This is compared to a theoretical calculation based on [46], described in Sec. 3.3.4, kindly made available to us by our collaborators.

We can understand this measurement intuitively in the limit of squeezed vacuum. The detuned drive alters the phase of the photon pairs that are created through the atom mediated non-linear photon-photon interaction. Recall the approximation of weakly squeezed vacuum in Sec. 3.1.3 that was given by

$$\hat{S}(\epsilon)|0\rangle \approx |0\rangle - \frac{\epsilon}{\sqrt{2}}|2\rangle = |\epsilon\rangle. \quad (5.9)$$

where $\epsilon = re^{i\phi_S}$ characterizes the squeezing operator. The squeezing angle ϕ_S appears in the phase of the two-photon component of the squeezed vacuum and determines how the squeezing is distributed between the two quadratures.

More technically and within the framework of [46] we recall the expression the spectrum of squeezing in Eq. 3.68 given by

$$S_\theta(\omega) = -\frac{\Gamma_{\text{tot}}}{2\beta} \frac{P_{\text{in}}}{P_{\text{sat}}} \text{Re} \left[e^{2i\theta} \phi_N(\omega - k_0) \right] \quad (5.10)$$

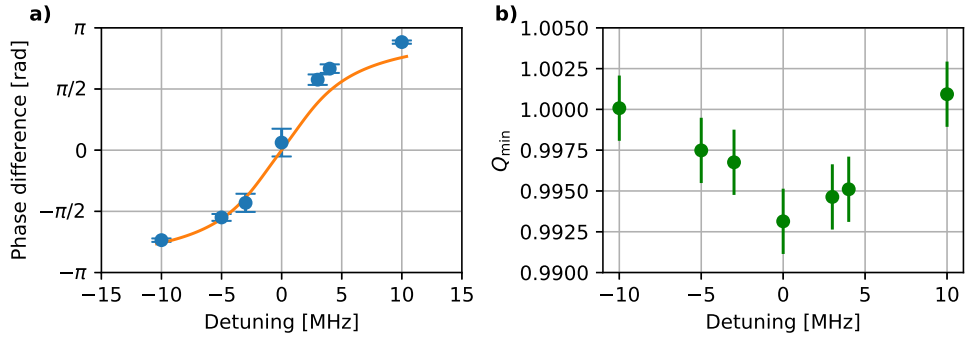


Figure 5.9: a) Relative phase $\theta_0^{\text{sig}} - \theta_0^{\text{LO}}$ between the $\cos(2\theta)$ modulation of the variance and the electric field evolution with $\sin(\theta)$. This is compared to the phase of the numerically calculated complex function that accounts for correlated photons $\phi_N(\omega - \Delta)$ calculated for $\beta = 0.007$ and $N = 50$. Note that the theory assumes the limit of weak input field, $P_{\text{in}}/P_{\text{out}} \ll 1$ while the measurement has $P_{\text{in}}/P_{\text{out}} = 0.35$. b) Minimum Q for the detuning values in a). While the squeezing phase shifts with detuning the squeezing strength reduces with increasing detuning. The complete plot for $Q(\theta)$ is shown in App. C.4

As explained in Sec. 3.3, the complex function ϕ_N captures the photon correlations. For a resonant drive field ϕ_N is real and therefore does not add to the phase θ in (5.10). For a detuned drive, however, ϕ_N is complex and we can calculate a phase that adds to θ . This is done in Fig. 5.9 where ϕ_{max} was extracted from ϕ_N , where ϕ_N was calculated assuming $\beta = 0.007$ and $N = 50$. The theoretical prediction is in good agreement with the data for negative detunings. For positive detunings it follows the same trend as the theory but differs quantitatively. This is likely to be a consequence of the trap modification from the detuned drive. The red detuned drive pulls the atoms closer to the fiber and thus increases their coupling strength but also the heating rate due to increased scattering. The opposite effect takes place for blue a detuned drive field. Overall, this results in a variation of β throughout the plotted data while the theory assumes constant β . The strength of the squeezing reduces with increasing detuning. Figure 5.9b shows the lowest value of Q for every detuning as extracted via the fit. For ± 10 MHz detuning, where the output is almost completely phase squeezed (and therefore amplitude anti-squeezed) Q does not fall below 1. This is consistent with the numerical analysis of ϕ_N with respect to detuning from Sec. 3.3.4. The squeezing angle asymptotically approaches $\pi(-\pi)$ for positive (negative) detuning while the amplitude of ϕ_N goes to zero, i.e. squeezing vanishes.

5.7 Probe power dependence

The next parameter that influences the squeezing is the power of the probe field. Therefore, we carry out a range of squeezing measurements with varying probe power and analyse the results in the usual way, i.e. we extract the variance as a function of phase.

The analysis of a total of 10 measurements of 50k traces each is summarised in Fig. 5.10

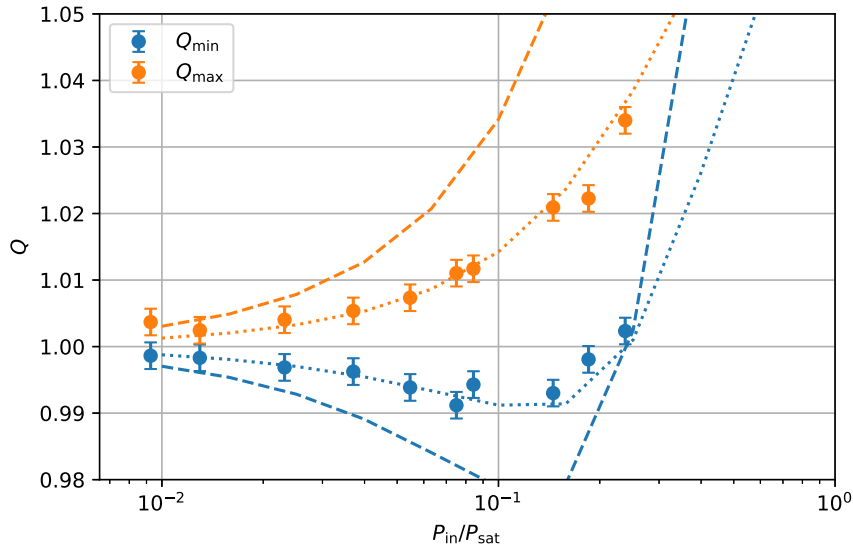


Figure 5.10: Maximum and minimum Q as function of probing power, normalised to $P_{sat} = 135$ pW. The dashed and dotted lines are obtained from numerical simulations by the authors of [40], where the dashed line corresponds to the simulation rescaled with our measured detection efficiency and the dotted line to the simulation rescaled with an effective efficiency of 15%. The difference may be explained by additional detection noise from the setup and the fact that the theoretical curve assumes the full frequency spectrum compared to a 17 MHz window in our analysis.

where we plot the minimum and maximum values of Q as a function of the normalized input power, i.e. P_{in}/P_{in} . The underlying variance measurements and fits are given in App.C. The relative phase between the variance modulation and the electric field amplitude is close to zero for all powers, indicating amplitude squeezing (see Fig.C.6 for the respective plot). While the maximum variance in Fig. 5.10 grows continuously with input power the minimum variance decreases down to the local minimum at $P_{in}/P_{in} \sim 0.1$ and increases then as well.

The non-linear photon transport framework discussed in Sec.3.3 assumes the limit of a weak drive field to truncate Fock space for $n > 2$ to simplify the calculation. Therefore, this framework is not suited to evaluate the squeezing for arbitrary input power. A new framework was developed by our collaborators, based on an approach that truncates the correlations rather than the photon number [61]. Unlike the theoretical framework reviewed in Sec. 3.3, this new framework cannot predict the spectral distribution of squeezing, such that the values in Fig. 5.10 correspond to the complete squeezing at all frequencies. This is in contrast to the measured data that corresponds to a finite frequency window and in particular cuts out the correlations from 0 to 3 MHz which limits the comparison between theory and experiment. The lower frequency cut-off can be reduced to decrease the comparison difference but that affects the observed squeezing at high probing powers where transmission changes due to atom heating affect the signal transmission

and increase the signal variance.

The experiment data in Fig. 5.10 is compared to numerical calculations by the authors of [40] using the new framework mentioned in the previous paragraph. Conversion between the numerical results and the experimental data is explained in Sec. 3.4. The numerical results are rescaled with our detection efficiency $\eta_{\text{tot}} = 0.36$ (dashed lines). For this detection efficiency it is in poor agreement with the simulation. This may be explained by additional detection noise in the interferometer at higher frequencies that is not taken into account through the detection efficiency measurement. The dotted lines correspond to an effective detection efficiency of 15% and are in good agreement with the data. In particular, the data exhibits minimum Q at a similar P_{in} as the numerical calculation. Another discrepancy between theory and experiment lies in the different frequency ranges that are considered, as was discussed in the previous paragraph.

To develop intuition for the curve we consider the low and high power limit. We know already from the initial low-power limit framework that for small $P_{\text{in}}/P_{\text{sat}}$ squeezing scales proportional with input power, as is apparent from Eq. 3.67. This makes sense since the chance of two photons interacting with the same atom within its lifetime is higher for a higher number of photons. As the drive power increases saturation effects start to appear. In the limit of saturation each atom scatters at the maximum scattering rate which only adds noise to both quadratures. Note that the increasing variances only correspond to the correlated component of the output field. In the limit of complete saturation this component is vanishing relative to the component of the input light field that propagates through the ensemble without any absorption due to bleaching. This satisfies the intuition that a completely bleached ensemble has vanishing effect on the incident field as the field strength increases.

5.8 The spectrum of squeezing

Having investigated the role of probe detuning and power we turn to the spectral characteristics of the squeezed light. We are particularly interested if the predicted spectral characteristics can be observed that are expected for low and high optical depths. To this end we perform a homodyne measurement in both respective regimes. The spectra are binned into frequency bins that include 100 bins of the raw spectrum in order to observe the trend that is otherwise hidden by noise. The bin size corresponds to 1.4 MHz spectral width. Figure 5.11 shows the angle resolved spectra S_θ for the angle relative to the electric field phase of maximum and minimum variance, that is $\theta = -0.44\pi \sim \pi/2$ and $\theta = 0.15\pi \sim 0$. The corresponding underlying plots of Q_θ are provided in App.C.7. The error bars correspond to the standard error of the spectral average of the respective bin. Before binning the spectra a few narrow and technical peaks were masked in the same fashion as already described for the pronounced 10 MHz peak. The masked peaks were at 1.97, 2.1, 2.25, 2.4, 10, 12.5, and 24.5 MHz. The maximum masking width was 10 bins while the data points in the two spectra correspond to 100 bins, i.e. the masking is still narrow when compared to the bin width. Without masking several extremely large error bars appear in the spectra which originate entirely from calculating the standard error of a spectral average that includes a large peak and are of no interest with respect to the relevant atom-induced physics that lacks such sharp features.

Low optical depth

We start with the low optical depth regime for which the spectra of maximum and minimum noise are shown in Fig.5.11a, averaged from 50k traces. In this measurement, the average optical depth was 1.17, corresponding to an ensemble of ~ 50 atoms. Probing power was 20 pW and thus $P_{\text{in}}/P_{\text{in}} \sim 0.15$. This lower value was necessary to reduce heating-induced atom losses that reduce the non-linear features. Note that the y -axis spans twice the range as the left panel, i.e. the spectrum has higher amplitudes. Both the minimum and maximum variance spectra in the graph display a trend of increasing and decreasing amplitude, respectively. More specifically, the minimum variance spectrum has the lowest values in the frequency range from 0 to 10 MHz, in contrast to the high OD spectrum. The overall amplitude of the squeezing spectrum is larger in the low OD limit than in the high OD limit due to the lower optical depth, only partially compensated by the higher drive power. Beyond 20 MHz the minimum and maximum variance spectra start to have similar amplitudes. This shows reduced squeezing at high frequencies. Note that the error bars increase with frequency due to the reduced signal to noise ratio of the balanced detector for increasing frequency and the low pass filter of the oscilloscope. The data compares well with the theoretical calculations of S_θ . In particular the trend in the data of decreased squeezing with increasing frequency is well described by the theory.

High optical depth

Next we turn to the high optical depth regime, depicted in Fig.5.11b, averaged from 50k traces. The average optical depth in this measurement was 5.3, corresponding to on average ~ 330 trapped atoms. Probing power was 80 pW and thus $S_0 = P_{\text{in}}/P_{\text{in}} \sim 0.6$. The blue spectrum, corresponding to the smallest electric field variance with respect to phase, is consistently below 0 for frequencies up to 25 MHz. More importantly, the lowest values are in the range from 10 to 20 MHz, i.e. the spectrum peaks and thus exhibits the sideband that was discussed in Sec. 3.3.3. The orange spectrum, corresponding to maximum electric field variance, also peaks but for lower frequencies than the minimum noise spectrum. This may be explained through technical noise at low frequencies that always adds to the variance and never reduces it since it is uncorrelated. Considering the error bars and the spread of the data points the spectrum shape is not particularly clear but it bears qualitative resemblance to the sideband shape that we expect.

The figure also shows the amplitude of the squeezing spectrum obtained from the framework in [40] and given by Eq. (3.67). The spectrum is plotted for $\theta = 0$, corresponding to maximum quadrature variance with a correction due to the extraction efficiency of 36%. Quantitative agreement between the calculated spectrum and the data is reasonable considering the size or the error bars. A possible explanation of the deviation is a fluctuation of N which shifts the frequency of the sideband peak and thus causes increased noise at these frequencies. Another hypothesis is a generally too low estimate of the atom number due to varying coupling strength. As discussed above the calculation to estimate the atom number from the optical depth depends on β which may have deviated from the value of 0.007 that is assumed here and was extracted from the measurement in Sec. 4.6.5. Finally, note the framework assumes low input power whereas the measurement is done at $S_0 = 0.6$ which may account for part of the differences between experiment and theory.

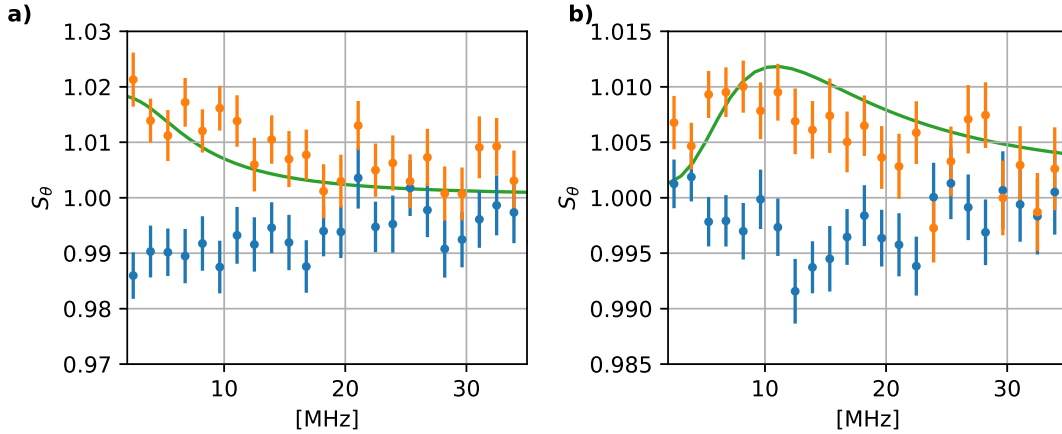


Figure 5.11: Homodyne spectrum for $N = 50$ (a) and $N = 200$ (b) for the maximally squeezed θ_{\min} (blue) and maximally anti-squeezed phase $\theta_{\max} = \theta_{\min} + \pi/2$ (orange). For comparison we show the theoretically calculated spectrum according to [40] and scaled with a detection efficiency of 36%.

In summary, the spectral analysis of the output light allows only qualitative statements. Squeezing shifts from lower to higher frequencies when increasing the number of trapped atoms and sidebands are weakly discernible in the high optical depth regime. Besides this, the analysis here illustrates that squeezing occurs continuously over frequency bands of several MHz around the carrier frequency, a feature that is not apparent from the variance analysis in the majority of this thesis where the spectrum is integrated and thus averages out spectral features.

5.9 Squeezing from a free space ensemble

The focus of this thesis is on interfacing an ensemble of trapped atoms. However, for many experiments the trapping is not mandatory and similar measurements can be made with just the MOT cloud surrounding the fiber. There are three major differences between the free cloud interface and the trapped ensemble interface. Firstly, the coupling strength β of different atoms varies over a larger range for the free cloud. A trapped ensemble, molasses-cooled into the 1D-lattice trap, exhibits a smaller spread of β albeit still finite due to the thermal occupation of vibrational levels in the micro-traps. Thus, while the cloud may present the same optical depth for probe fields it is still physically a different experiment since some atoms are interfaced significantly more strongly than others, an effect that is reduced by the trapping. The second major difference is that the MOT cloud disperses more quickly, i.e. the experiment duration has to be low enough to be carried out before the cloud density has changed too much. This can be difficult for example when magnetic fields have to be ramped up which takes finite time due to coil inductance. Thirdly, the trap allows to interface the ensemble with well defined polarization since the atoms are centered around the same azimuthal angle. A linearly-polarized probe field

can thus interface the atoms with elliptical polarization, if the strong axis of the probe field is aligned to the trapping plane, and with approximately linear polarization if the strong axis is rotated by 90° . This choice is not possible when interfacing the probe light with the MOT cloud that is more uniformly distributed around the fiber.

Having discussed these differences we demonstrate that squeezed light can also be obtained from a free MOT cloud. To this end we perform another homodyne measurement with the difference that the red trap field is switched off completely and the blue trap field is reduced to ~ 1 mW. The latter is necessary to keep the fiber waist hot in order to prevent coating it with Cesium atoms that adsorb to the fiber surface from the background gas and then render it opaque to weak probe fields. To obtain the optical depth of 2.5 the fall down time of the MOT cloud before probing is reduced substantially. Since the coupling strength is not known in this interface configuration we cannot make a statement regarding the number of probed atoms. However, in [62] the authors report a coupling strength of $\beta = 0.0055$ of a MOT cloud to a nanofiber which suggests that this configuration is in fact comparable to the trapped ensemble where we found $\beta = 0.007$. Indeed, the homodyne measurement with the MOT cloud yields squeezing with a minimum variance of 0.3% below the vacuum variance. The underlying analysis is plotted in App.C.7. This result is particularly interesting since it illustrates that the experiment can be simplified significantly if the trap is omitted at the price of an apparently only modest reduction of the coupling strength. Furthermore, it shows that our observation of squeezed light is independent of the atom periodicity, in agreement with the theoretical framework.

5.10 Possible experimental improvements

The observation of squeezed light from an ensemble of requires reducing all possible noise sources and loss channels as much as possible. Several ways exist to improve the existing setup.

5.10.1 Reduce detection losses

Several possibilities exist to increase the current detection efficiency. Firstly, one could propagate the signal in free space from the nanofiber coupling setup to the homodyne detection setup to avoid the losses from fiber coupling but that this could reduce spatial alignment stability and spatial mode filtering, both of which important for LO mode matching. It was reported in other squeezing experiments [63] that it can be beneficial to remove the protective glass shield on the photo diodes to increase their efficiencies at the expense of photo diode lifetime. Furthermore, the NPBS in the homodyne detection has inevitable reflections at the front and rear face, despite its anti-reflection coating, which could be eliminated by replacing it with a plate beam splitter. Such beam splitters can be manufactured with great precision and thus also offer splitting ratios closer to 50:50 than the Thorlabs beam splitter used in our setup.

5.10.2 Improve power balance

We observed that the power balance on the homodyne detector can lead to undesired signatures in the detected variances. To investigate this we perform a reference measurement with deliberately imbalanced levels on the two photo diodes by rotating the local oscillator input polarization

by a small angle. This does not affect the splitting of the signal field so we are essentially testing if the absolute power incident on the photo diode affects the noise measured by the balanced detector. Figure 5.12 shows the results from this measurement. The amplitudes of the averaged detector output δI , proportional to the electric field of the signal input, are shown in the right panels. Here, we the offset was not corrected by subtracting the heterodyning DC level, as was done in the previous plots. For optimum power balance (assuming equal photo diode efficiency) the detector output should be centered around 0 V. Thus, the offsets in the two plots indicate imbalance while the amplitude of the sine (blue curves) is approximately similar, i.e. the strength of the signal field was similar. But the trend for the variances, shown in the left panels of the same figure, is significantly different and bears similarity to the reference measurement discussed previously. Both variances approximate a sine modulation but the sign appears to depend on the sign of the imbalance on the detector. The phase of the variance modulation means that the balanced detector output noise is proportional the signal field amplitude. Maximum field amplitude in the right hand plots of Fig.5.12 means that the phase between local oscillator and signal field is 0 or π and perfect constructive or destructive interference occurs. Consequently, the signal field is maximal in one detector arm and minimal in the other, presumably close to perfectly extinguished due our good mode matching. This could explain the variance modulation we observe if we assume that the two photo diodes have different noise characteristics. If the signal is incident almost entirely on one photo diode the variance reflects the noise characteristics of that photo diode and vice versa for the other photo diode of the detector. Of course, the two photo diodes are the exact same model but manufacturing variations are possible. Still, this speculation is arguable since the power incident on the photo diode is almost entirely local oscillator light, i.e. the power variation due to constructive and destructive signal interference is extremely small. However, it seems convincing that the variance modulation is linked to the technical imperfection of improper power balance on the balanced detector and thus not an intrinsic feature of the light that we want to analyze.

The beam splitter used in our setup (Thorlabs, BS105) was in fact not splitting perfectly 50:50 but rather 45:40, i.e. it split both unevenly and with losses. Beam splitters that are superior in both regards are available and could replace the current beam splitter to improve the homodyne setup.

5.10.3 Reduce heating

The probing pulse incident on the atoms is comparable to the saturation power of fiber coupled Cesium atoms. On resonance and at saturation, a Cesium atom scatters $\Gamma/4$ photons per second, corresponding to ~ 8 MHz. This leads to heating and eventually atom loss, thus reducing the overall probe field absorption. Therefore, the signal amplitude on the detector changes over the course of the probing pulse. Naturally, this amplitude change is proportional to the field amplitude and the variance will thus also be proportional to the field amplitude. This effect can give rise to a $\sin(2\theta)$ variance modulation with a phase strictly linked phase of to the signal amplitude. The spectral features of this transmission change are most pronounced at low frequencies. Indeed, the signal spectrum shown in Fig. 5.5a rises notably above the vacuum reference at very low frequencies up to a few hundred kHz. Since we can see the transmission change in the signal spectrum we can also deduce that it is negligible at higher frequencies. Thus, the low fre-

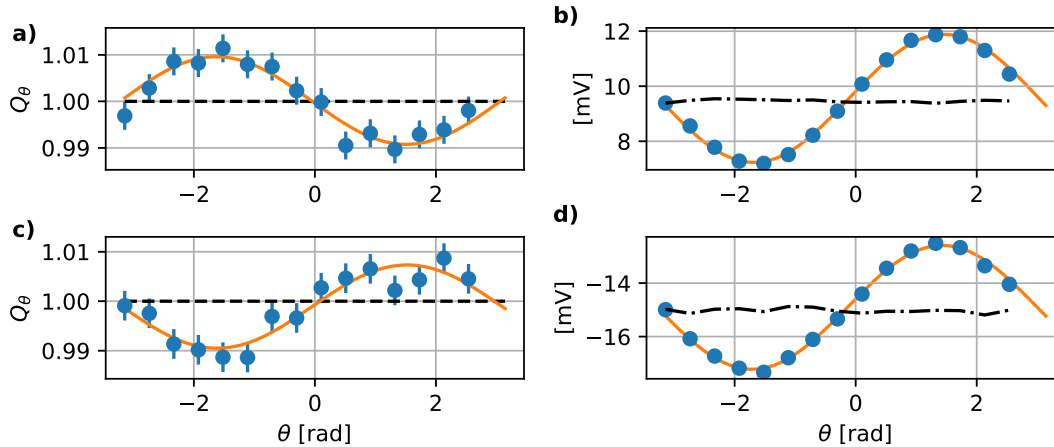


Figure 5.12: Effect of imbalanced power levels on the balanced detector. a) and b) correspond to positive imbalance, and c) and d) to negative imbalance. The sign flip of the the $\sin(\theta)$ variance modulation suggests power imbalance as the explanation for the asymmetry observed in several variance measurements.

quency cut-off of 3 MHz used for the variance calculation in the above squeezing measurement is sufficient to exclude this effect.

Reducing the atomic heating generally improves the homodyne measurement of quadratures in our experiment. This can be achieved by shorter probing duration which requires recording more traces to recover the loss of signal. Another option is to interleave the homodyne probing stage with molasses cooling stages to cool the ensemble back to its initial configuration. Finally, the trap depth could be lowered by increasing the trap field intensity to create stronger atom confinement. Through this, atoms can scatter more photons before being lost from the trap and thus less atoms are lost if the probing duration is kept constant.

5.11 Summary

This chapter reported on the observation of quadrature squeezing through homodyne detection of light that couples weakly to an ensemble of emitters. The experimental setup was detailed, the key analysis procedures explained, and finally the squeezing was studied with regards to probe detuning, probing power and atom number. The effect of detuning onto the squeezing phase is in good agreement with the theoretical framework. The power dependence shows a global maximum squeezing (minimum Q_θ) at similar power as theoretical predictions for our experimental parameters. The squeezing amplitude deviates which may be explained through higher frequency detection noise. The spectral analysis provides qualitative insight regarding the spectral shape of the transmitted light and shows good agreement with theory. Finally, we demonstrated that squeezed light can also be obtained from a MOT cloud surrounding the nanofiber which suggests simplified experimental schemes to obtain squeezed light from weakly coupled

5. OBSERVATION OF SQUEEZED LIGHT

emitters.

Outlook and Conclusion

We moved from empty optical tables to observing faint light fields for which we showed that they are in fact quadrature squeezed due to a non-linear interaction with the trapped atom ensemble. Can the experimental setup be improved? And how do these results relate to other squeezing measurements?

6.1 Further experiments

A key advantage of the homodyne detection presented here is that it directly accesses the spectrum of correlations. This is in principle also possible via time resolved single-photon detection but requires better background suppression since SPCMs cannot distinguish well between background photons and signal photons. Even more difficult, but not impossible, is phase resolved detection via SPCMs. Therefore, the current setup offers a practical path to studying the spectrum of squeezing in more depth. A first step would be to increase the detection efficiency to map out the frequency sidebands emerging due to the non-linear interaction more clearly than was done in this work. This would allow to study their scaling with respect to atom number and coupling strength. Higher coupling strengths could be achieved with improved trap geometry due to higher blue trap power.

For atom trapping itself it may prove beneficial to exchange the nanofiber in the current setup and increase the diameter to a level where the trade-off between reduced coupling strength and increased mechanical stability is still acceptable. A shorter waist length should also improve stability. This could once again motivate the attempt to trap very large ensembles with optical depths of more than 1000. In this context, schemes to increase the filling factor beyond 0.5 and possible to approach unity may be implemented [34]. Unity filling combined with a longitudinal trap periodicity below $\lambda/2$, possible through a trap configuration with a 685 nm blue detuned standing wave, would open the path study sub-radiant coupling of an atom ensemble to the fiber guided mode [64].

6.2 Squeezed light as a signature of non-linear interaction

Comparing the squeezing strength in our results with the squeezing strengths achieved through spontaneous parametric down-conversion (SPDC) it is clear that our scheme is very unlikely to find application in metrology. Numerical calculations indicate that for realistically achievable coupling strengths the maximum level of squeezing calculated from the existing theoretical framework is below 10% for any atom number and input power [46]. On the other hand, setups based on SPDC are capable of up to 15 dB noise suppression with higher brightness and over a broader frequency range [65].

Instead, our experiment (literally) sheds new light on the simple scenario of light propagating through an ensemble of emitters. A classical input field, meaning a coherent state, exits the ensemble as a non-classical field, i.e. a quadrature squeezed state, due to interaction with an ensemble of hundreds of atoms. Squeezing in optical fibers was already observed decades ago but then the non-linearity emerged from the fiber material itself [66]. Such non-linearities are much weaker than for the atomic ensemble in our experiment. Consequently, higher pumping powers are required to make them observable. Squeezed light was also already observed in a nanophotonic platform but again relying on the bulk material non-linearity of silicon-nitride, additionally enhanced in a ring resonator, instead of the non-linear response of an atomic ensemble [67]. These two examples illustrate the novelty of our results: We obtain squeezed light from a single passage through a small atomic ensemble coupled to a nanophotonic waveguide.

Appendices



Die approbierte gedruckte Originalversion dieser Dissertation ist an der TU Wien Bibliothek verfügbar.
The approved original version of this doctoral thesis is available in print at TU Wien Bibliothek.

Supplementary plots of squeezed states

A.1 Evolution of a coherent state with increasing squeezing

In Ch.3 we calculate the coefficients of squeezed states in the Fock basis (Eq.3.41) and plot the scenario of a weakly squeezed state, where coherent fraction dominates, and a strongly squeezed state, that has been deformed substantially by the squeezing operator (Fig. 3.3b and c). Figure A.1 details the evolution of this squeezing in Fock space with respect to r , starting with a coherent state and applying increasingly stronger squeezing operators.

A.2 Phase dependence of squeezed states

The Fock space representation of a bright, squeezed state depends on the relative phase between the coherent state and the squeezing operator, i.e. $\alpha - \phi$. Here, we depict the Fock space dynamics due to this phase.

Figure A.2 shows the phase evolution of a squeezed state with $\alpha = \sqrt{10}e^{i\theta}$ with respect to ϕ , assuming $\theta = 0$, and for $r = 0.4$. For reference, the envelope of a pure coherent state is shown which demonstrates that the width of the state in Fock space is below and above the width of a coherent state at different phases. That means there are both number-squeezed states and anti-number-squeezed states in the group of quadrature squeezed states.

The effect of the squeezing phase becomes even more impressive for strongly squeezed states. This is demonstrated for $r = 2$ in Fig.A.3, again for $\alpha = \sqrt{10}e^{i\theta}$, $\alpha = 0$ and varying ϕ . For a relative phase of $\pi/2$ the Fock coefficients look very similar to squeezed vacuum where only even photon numbers are measurable.

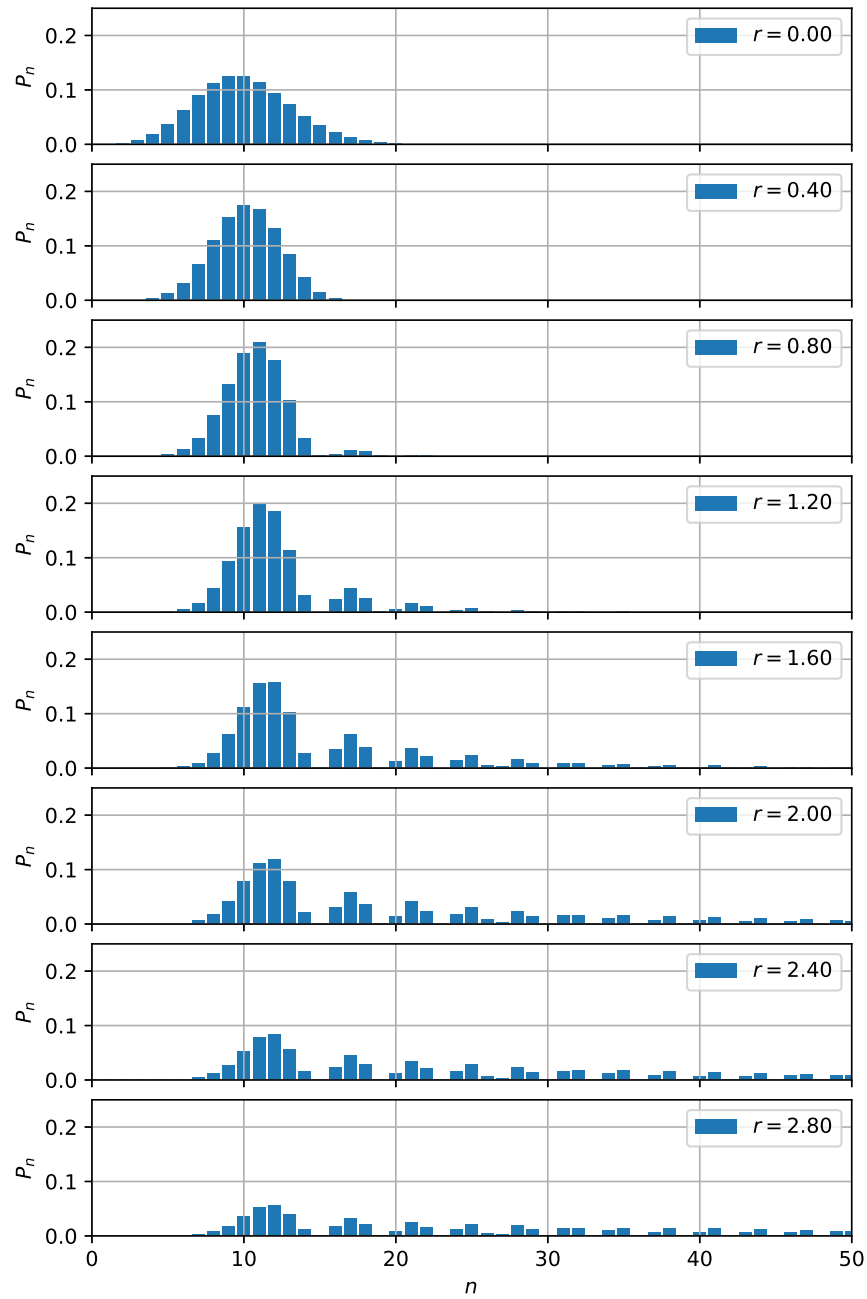


Figure A.1: Evolution of a coherent state with $\alpha = \sqrt{10}$ for increasing squeezing strength r for $\phi = 0$.

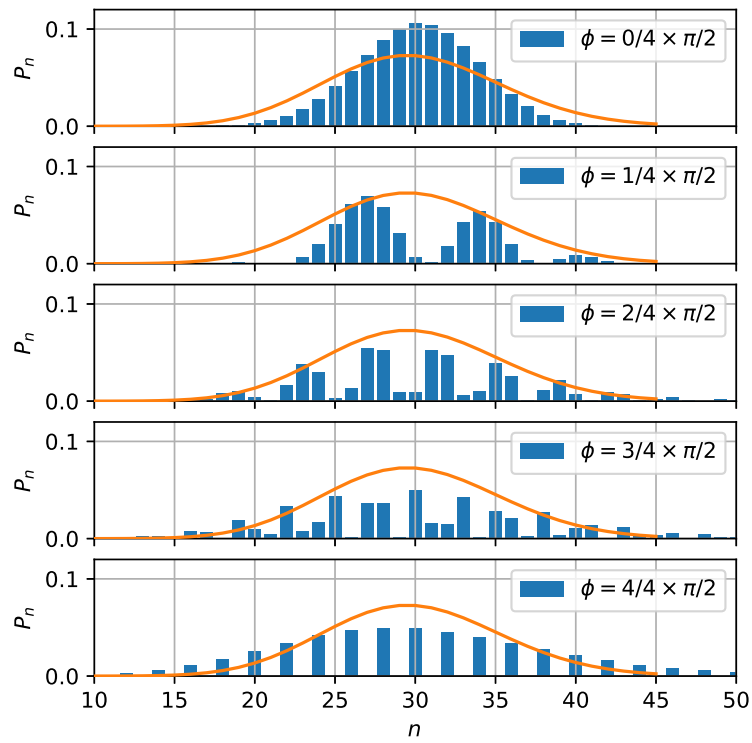


Figure A.2: Fock space distribution for different optical phases and for weak squeezing ($r = 0.4$)

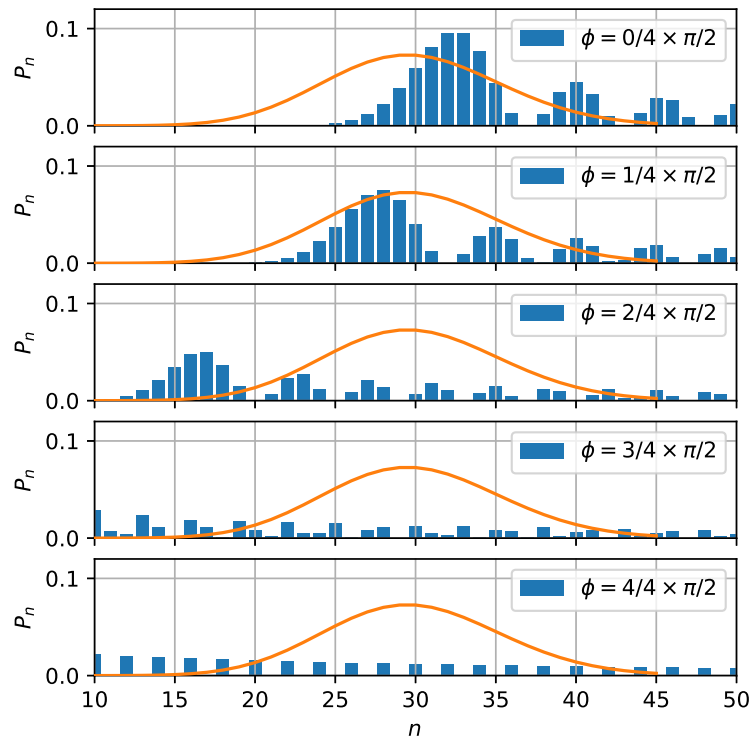


Figure A.3: Fock space distribution for different optical phases and for strong squeezing ($r = 2$)

Fiber analysis after removal from the vacuum

The difficulties with stable trap lifetime and optical depth described in Sec.4.7 prompted a thorough investigation of a fiber that was used in our apparatus, had trapped atoms and exhibited a substantial drop in lifetime. Specifically, the question was if there were deformations visible on the fiber that might have altered its mechanical properties or the optical modes guided by the fiber. Also pollution of the fiber surface was suspected at some point, especially since the vacuum pump in our setup, a combination of an ion pump and a getter pump, was not tested before in conjunction with a nanofiber and possible outgassing of the getter element during its activation might lead to detrimental deposits on the fiber waist. Similarly, elements outgassing from the Cesium dispenser were considered. To pursue this question, the fiber recovered from the vacuum was brought to the scanning electron microscope (SEM) facility at TU Wien where unexpected structures were found on the surface, detailed below. These findings suggested a spectroscopic analysis to understand their chemical composition and the results from this measurement are described in Sec.B.2.

B.1 SEM images

A scanning electron microscope directs a focused electron beam of various powers, typically in the keV range, at a target sample, scans it and detects deflected electrons at each scanning position in order to reconstruct an image. The advantage over optical microscopy is that the imaging wavelength, in this case the deBroglie wavelength of electrons, is orders of magnitude shorter such that structures as small as 1nm can be resolved whereas standard optical microscopy is limited to hundreds of nanometer resolution. The downside is that the sample, subject to electron bombardment, can be damaged or completely destroyed. Additionally, the sample has to be coated with a conducting layer, in the study presented here Palladium was used. Therefore,

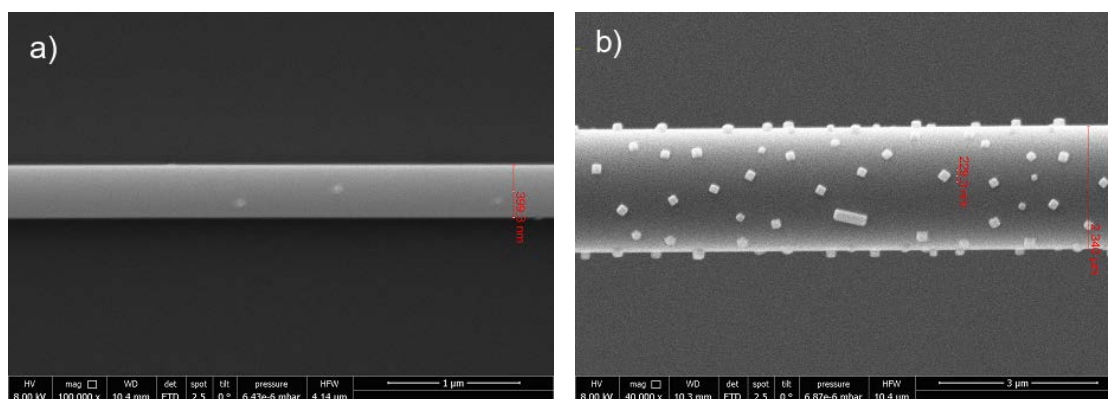


Figure B.1: a) SEM image of the nanofiber waist. Only small dots of the substance are visible. Electron beam spectroscopy was carried out on the substance with the results shown in Fig. B.2 b) SEM image of the nanofiber taper at a diameter of $2.34 \mu\text{m}$. Cubic shapes are spread across the fiber surface, mostly with similar size.

optical components like a nanofiber cannot guide light anymore after SEM imaging because the Palladium renders them highly opaque to visible and infrared light.

The recovered fiber was imaged along the majority of its waist and at several positions along the taper. SEM images of two sections are shown in Fig. B.1. The waist of the fiber shows various small round deposits, with typical sizes of tens of nanometers and evenly distributed along the fiber. The nanofiber diameter was confirmed to be very close to the intended 400 nm. The shape of the deposits varied at nanofiber taper and particularly interesting shapes were observed at a few micrometer diameter, shown in Fig. B.1b. Here, the fiber was evenly covered with quadratic blocks with a side length of 150 nm. In some instances, the blocks had twice or three times the side length in one dimension with the other dimension unaltered, as visible in the central fiber section in Sec. B.2b.

B.2 Electron Energy Loss Spectroscopy

Observing these structures immediately rose the questions about their composition and at what time they formed on the fiber, that is whether they were already present on the fiber under vacuum and during the operation of the nanofiber trap. Understanding the deposit composition was considered key to understanding at what time they appeared.

To approach these questions electron energy loss spectroscopy (EELS) was performed on one of the cubes visible in Fig. B.1b. This technique exposes the sample to an electron beam of well defined energy and records the energy spectrum of the electrons after sample interaction. Incident electrons can excite atoms of the sample through inelastic collision and lose the characteristic energy of the induced transition. Thus the electron energy spectrum is a fingerprint of the materials contained in the spectrum that can be compared to calibration spectra for various elements. Such a spectrum is shown in Fig. B.2, where detection counts are binned with respect to

electron energy. The software used for analysing of the spectra compares peaks with a database and labels the peaks with the name of the element. The most pronounced peaks of the spectrum belong to copper and stem from the sample holder. Even though the EELS module on the SEM at TU Wien allows to extract the spectrum for a specified region of interest it is very difficult to completely suppress background signatures from the holder and other microscope components. The more significant signature in the spectrum is characteristic for Cesium, suggesting that the observed cubes contain at least partially Cesium. This element is highly reactive when exposed to ambient air and forms Oxides in a highly exothermal reaction and elementary cesium even catches fire when exposed to air. Since the interior of the vacuum chamber becomes coated with elementary Cesium emitted from the dispenser we naturally expect Cesium oxide to form once the vacuum is broken and Oxygen enters the chamber. The leading explanation became thus that the deposits consisted of Cesium-Oxide and were not present during trap operation. Additional features of the spectrum such as Silicon, and Aluminum, Iron, Gold and Lead, were attributed to the optical fiber and the fiber holder respectively.

In order to confirm the conjecture of the deposits consisting of Cesium-Oxyde we performed an X-ray diffraction measurement on one of the deposits in order characterize the lattice structure which, in combination with EELS, can serve as a fingerprint for chemical compositions of solids. The findings from X-ray diffraction were consistent with a range of Cesium-Oxydes but our hypothesis could not be confirmed with absolute certainty. It was decided to settle with this likely but not certain explanation and return to placing a new nanofiber in the vacuum instead of performing more extensive studies on the recovered fiber.

B. FIBER ANALYSIS AFTER REMOVAL FROM THE VACUUM

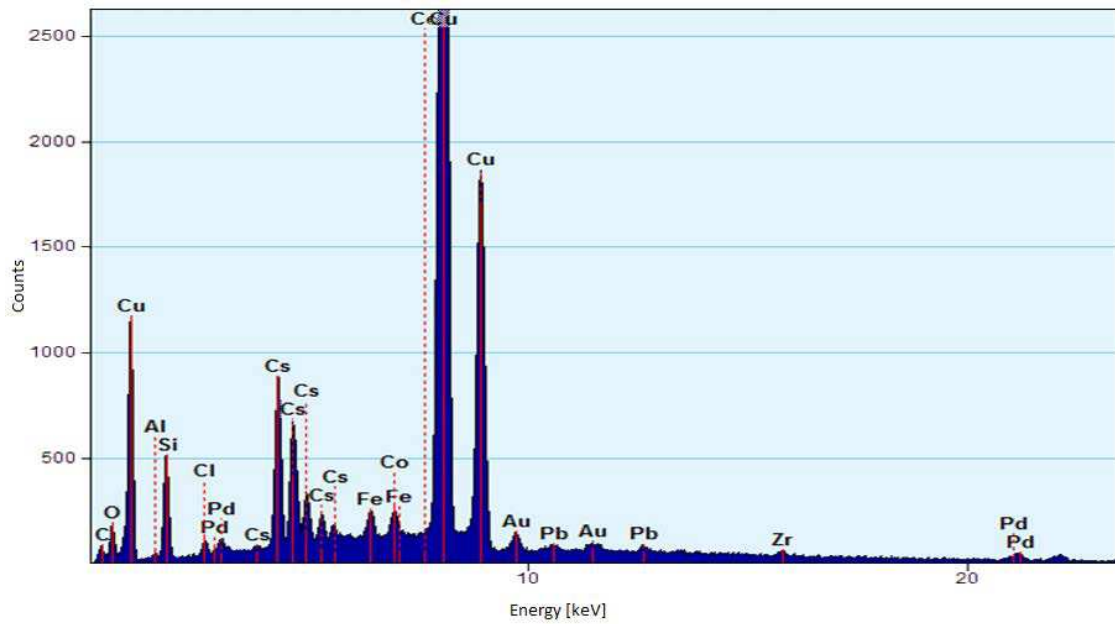


Figure B.2: Electron energy loss spectrum of a cube similar to those shown on the surface of the nanofiber in Fig. B.1. The analysis software compares peaks to a database and labels them with the element matching the characteristic peak position. Peaks are visible for Cesium and Oxygen, suggesting that the deposits consist of Cesium-Oxide. Peaks for Copper, Lead, Iron and Aluminum are attributed to the sample holder. Palladium originates from the coating of the sample, as does Gold and Lead. Silicon is likely to originate from the bulk of the silica fiber.

Supplementary material on Ch. 5

C.1 Oscilloscope setup

C.1.1 Sampling rate

The oscilloscope records a symmetric window of $500\ \mu\text{s}$ around the trigger and stores it with 65k data points, i.e. a time resolution of 8 ps in a .trc file that can be extracted readily via a Python module *lecroyparser*. The number of samples per trace needs to be high enough to allow resolving the frequencies of relevance in the experiment but should not be unnecessarily high which increases file size, slows down the storage process thus reducing the overall experiment frequency, and substantially increases data processing time. The time resolution of 8 ps entails a maximally resolvable frequency of 63 MHz, above the 50 MHz bandwidth of the balanced detector and well above the frequencies at which the squeezing is expected namely $1-2\ \Gamma \sim 5-10\ \text{MHz}$.

C.1.2 Low-pass filter

The choice of the sampling resolution detailed above lead to aliasing errors in the oscilloscope which could be corrected by switching on a 20 MHz low pass filter. The physical signals in our experiment are well below this limit, therefore it presents no harm to our measurement. Since the filter is applied to the whole trace it is included in both the signal and the reference ROI and cancels out for the ratio of the respective variances. The main consequence is that the signal, i.e. this ratio, becomes increasingly noise dominated above the filter limit. To characterize this filter we record 100 traces once with the filter activated and once with the filter deactivated. The respective spectra are averaged over all files and the ratio of the averages is plotted in Fig. C.1. The curve is fitted with a second order polynomial ($f(x) = \dots$) yielding a 3 dB attenuation at 19.7 MHz. This is a limitation for the squeezing spectra presented later.

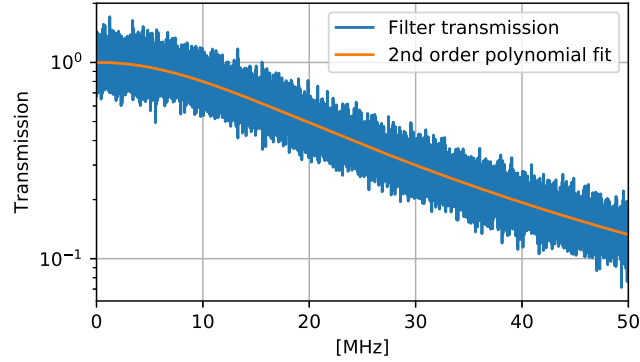


Figure C.1: Measured transfer function of the 20 MHz low-pass filter of the oscilloscope with a polynomial fit. The filtering proved necessary to avoid aliasing effects arising due to the relatively large sampling time of 8 ps which was chosen to limit file sizes.

C.2 The Wiener-Khinchin-Theorem

Processes that generate squeezing may be easier to calculate in the time domain while measurements of these processes may be easier to perform in the frequency domain. A link between both realms is provided by the Wiener-Khinchin-Theorem that provides a direct relationship between the power spectral density of a variable and its auto-correlation function.

We consider a general operator \mathcal{O} the expectation value of which we measure for a finite time τ . Then its power spectral density is defined as [68]

$$S_{\mathcal{O}\mathcal{O}}(\omega) = \lim_{\tau \rightarrow \infty} \langle \hat{\mathcal{O}}^\dagger(\omega) \hat{\mathcal{O}}(\omega) \rangle, \quad (\text{C.1})$$

where $\hat{\mathcal{O}}_\tau(\omega)$ is the Fourier transform of $\hat{\mathcal{O}}(t)$, windowed over the time period $-\tau/2 < t < \tau/2$. Then the Wiener-Khinchin theorem states the following equality

$$S_{\mathcal{O}\mathcal{O}}(\omega) = \int_{-\infty}^{\infty} d\tau e^{i\omega\tau} \langle \hat{\mathcal{O}}^\dagger(t+\tau) \hat{\mathcal{O}}(t) \rangle_{t=0} = \int_{-\infty}^{\infty} d\omega' \hat{\mathcal{O}}^\dagger(-\omega) \hat{\mathcal{O}}(\omega) \quad (\text{C.2})$$

C.3 Comparing squeezed and coherent light

To illustrate that the character of the analyzed light is substantially altered by the interaction with the atoms we analyze a light field of the same strength that has not interacted with an ensemble. To this end we attenuate the probe light via neutral density filters and perform the same analysis. The results are shown in Fig.C.3. The electric field amplitude shown in the right panel is very similar in amplitude compared to the amplitude in Fig.C.2b which means that the signal power entering the detection setup was similar. But the variances of these comparably bright fields look markedly different: The reference measurement lacks the $\sin(2\theta)$ modulation associated with squeezing and Q deviates substantially less from 1. Ideally, however, Q_θ should

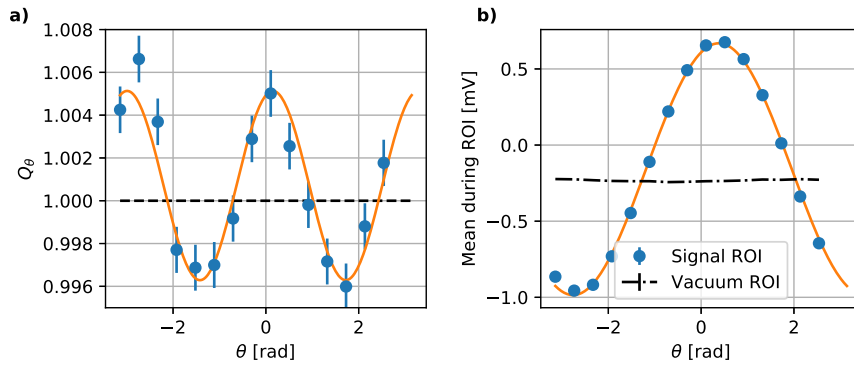


Figure C.2: a) Ratio of the signal variance and the vacuum variance, Q , as a function of θ . b) Offset-corrected mean δI of the balanced detector output as function of θ during the signal ROI and the vacuum ROI.

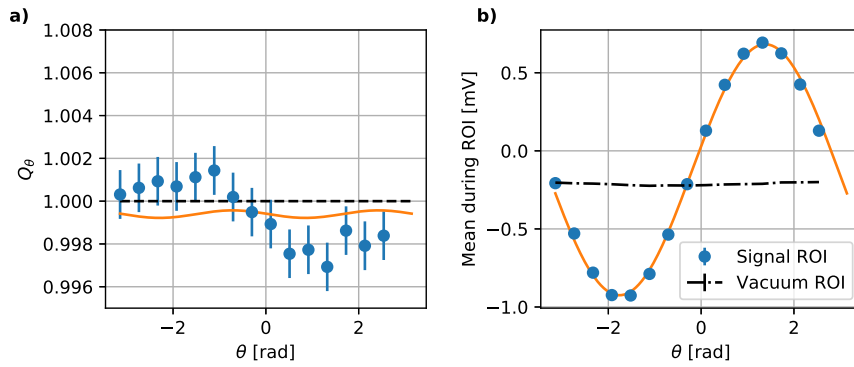


Figure C.3: Reference measurement of field attenuated by neutral density filters instead of trapped atoms. The y -scale matches the one from Fig.C.2a to emphasize that the modulation of the variance is significantly weaker than in the case of trapped atoms. The origin of the $\sin(\theta)$ modulation may originate from power imbalance on the detector photo diodes.

be perfectly flat for a coherent state. Evidently, that is not the case for the reference measurement where a $\sin(\theta)$ modulation is notable that is just π out of phase with the electric field amplitude. The modulation may originate from an imbalance of the signal field in the two arms of the balanced detector, as was discussed in Sec. 5.10.2.

C.4 Detuning measurement

The underlying data for the discussion in Sec.5.6 is given in Fig.C.4.

C.5 Power measurement

The underlying data for the discussion in Sec.5.7 is given in Fig.C.5.

From the underlying data we see the modulation of the variance continuously grows with input power, unlike the squeezing that peaks and then decreases. The fitting results for the variance modulation with $\sin(2\theta)$ are shown in Fig.C.6 together with the relative phase between the electric field amplitude and the variance modulation. This relative phase is approximately stable and indicates amplitude squeezing at any input power. The small offset from zero could originate from a finite probe detuning or aliasing effects due to finite bin size.

C.6 Squeezing spectra

The underlying data for the discussion of the squeezing spectra at high and low optical depth in Sec.5.8 are given in Fig.C.7, where a) corresponds to high optical depth and b) to low optical depth. The dashed vertical lines mark the data point for which the spectrum in the main text was plotted. The asymmetry of Q_{θ} with respect to θ for the low optical depth limit may be result from improper power balance on the homodyne detector.

C.7 Squeezing from a MOT cloud

The underlying data for the discussion in Sec.5.9 is given in Fig.C.8.

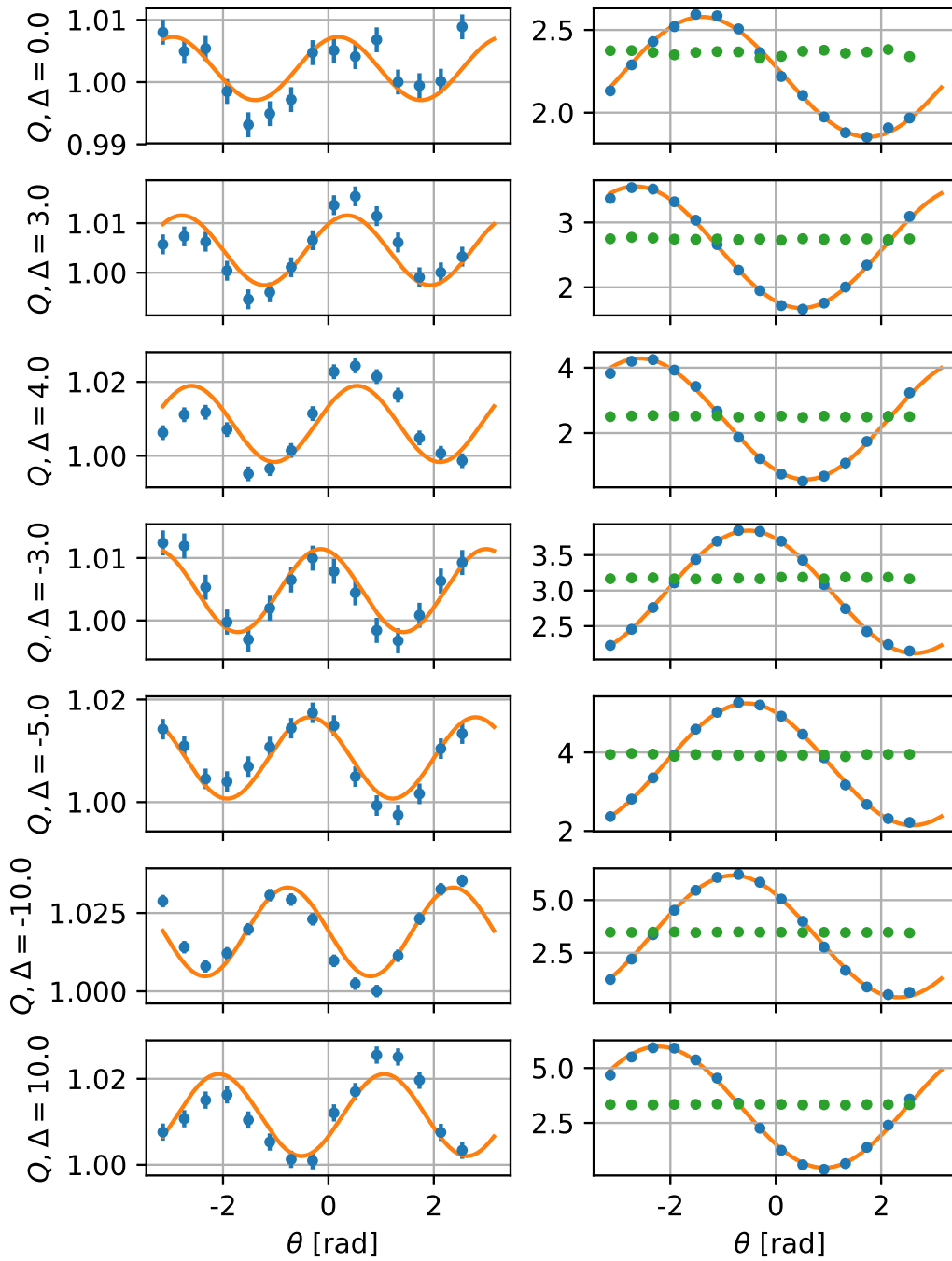


Figure C.4:

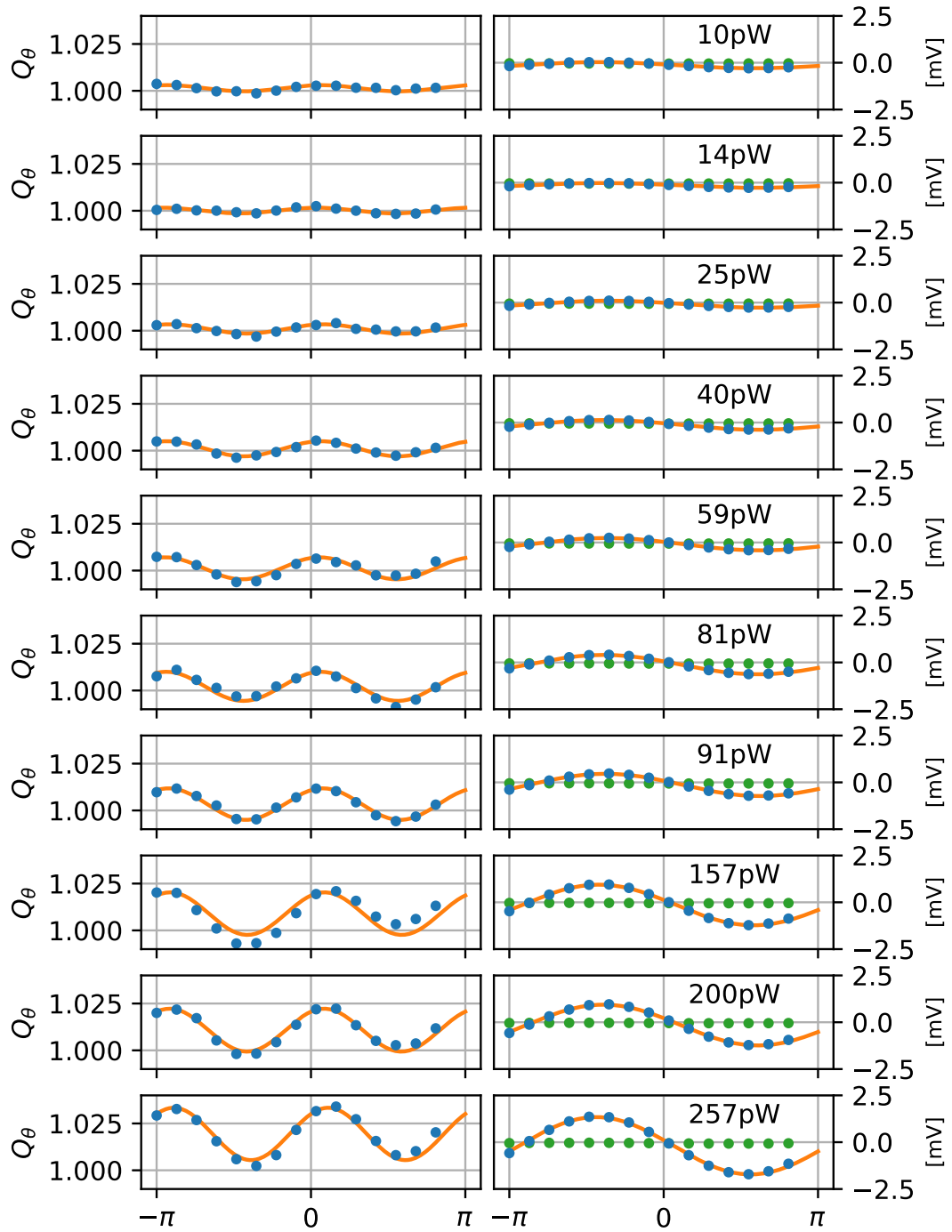


Figure C.5:

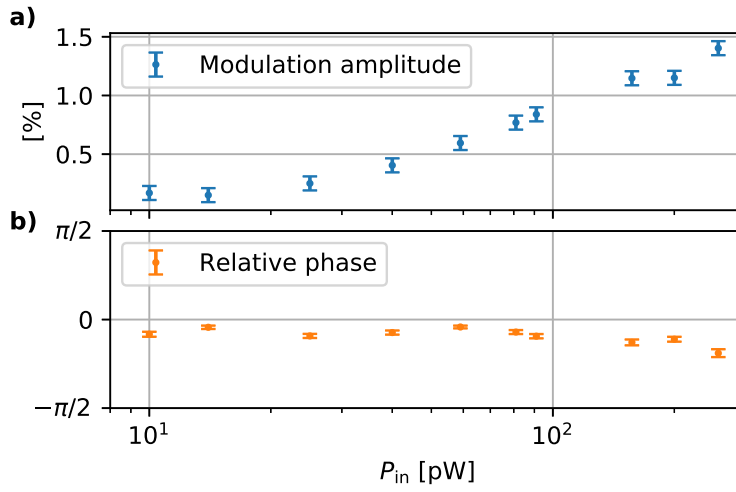


Figure C.6: a) Amplitude of the $\sin(\theta)$ -variance modulation as function of input power. The amplitude appears to follow a power law scaling. b) Relative phase between the electric field amplitude and the variance modulation, where 0 indicates amplitude squeezing and $\pm\pi/2$ indicates phase squeezing. We note good phase stability throughout the entire measurement.

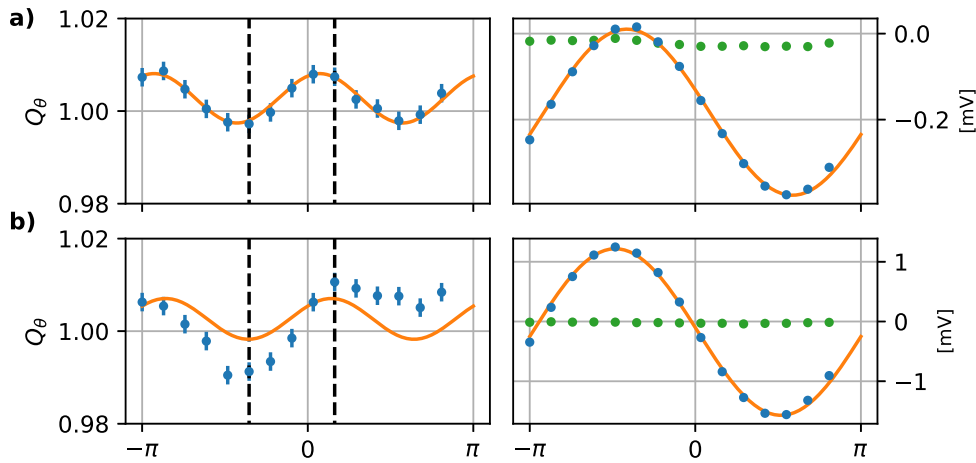


Figure C.7: Variance ratios and electric field amplitude underlying the spectrum analysis in Sec.5.8. The dashed vertical lines indicate the angles at which the spectra are analysed.

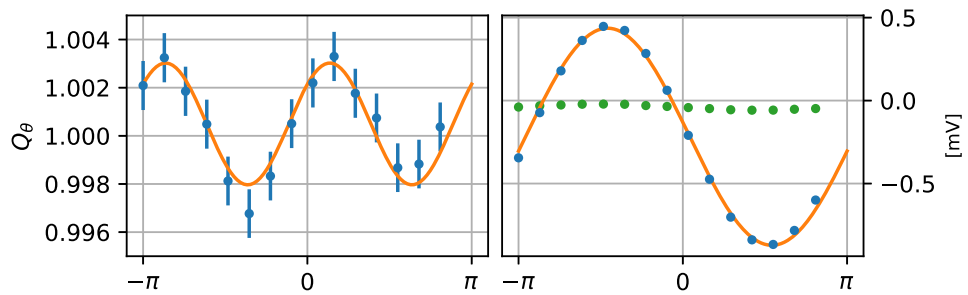


Figure C.8: a) Ratio of the signal variance and the vacuum variance as a function of θ when interfacing the probe light with a free MOT cloud around the nanofiber. b) Averages balanced detector output for the signal ROI (blue) and the vacuum (green).

Bibliography

- [1] Johann Wolfgang von Goethe. *Zur Farbenlehre*. 1810.
- [2] Isaac Newton. A letter of Mr. Isaac Newton, Professor of the Mathematicks in the University of Cambridge; containing his new theory about light and colors: Sent by the author to the publisher from Cambridge, Febr. 6. 1671/72; in order to be communicated to the R. Society. *Philosophical Transactions of the Royal Society of London*, 6(80):3075–3087, January 1671.
- [3] James Clerk Maxwell. VIII. A dynamical theory of the electromagnetic field. *Philosophical Transactions of the Royal Society of London*, 155:459–512, January 1865.
- [4] Fam Le Kien, J.Q. Liang, K. Hakuta, and V.I. Balykin. Field intensity distributions and polarization orientations in a vacuum-clad subwavelength-diameter optical fiber. *Optics Communications*, 242(4-6):445–455, December 2004.
- [5] R. Garcia-Fernandez, W. Alt, F. Bruse, C. Dan, K. Karapetyan, O. Rehband, A. Stiebeiner, U. Wiedemann, D. Meschede, and A. Rauschenbeutel. Optical nanofibers and spectroscopy. *Applied Physics B*, 105(1):3, September 2011.
- [6] K. P. Nayak, P. N. Melentiev, M. Morinaga, Fam Le Kien, V. I. Balykin, and K. Hakuta. Optical nanofiber as an efficient tool for manipulating and probing atomic fluorescence. *Optics Express*, 15(9):5431–5438, April 2007.
- [7] E. Vetsch, D. Reitz, G. Sagué, R. Schmidt, S. T. Dawkins, and A. Rauschenbeutel. Optical Interface Created by Laser-Cooled Atoms Trapped in the Evanescent Field Surrounding an Optical Nanofiber. *Physical Review Letters*, 104(20):203603, May 2010.
- [8] A. Goban, K. S. Choi, D. J. Alton, D. Ding, C. Lacroûte, M. Pototschnig, T. Thiele, N. P. Stern, and H. J. Kimble. Demonstration of a State-Insensitive, Compensated Nanofiber Trap. *Physical Review Letters*, 109(3):033603, July 2012.
- [9] Jan Petersen, Jürgen Volz, and Arno Rauschenbeutel. Chiral nanophotonic waveguide interface based on spin-orbit interaction of light. *Science*, 346(6205):67–71, October 2014.
- [10] R. Mitsch, C. Sayrin, B. Albrecht, P. Schneeweiss, and A. Rauschenbeutel. Quantum state-controlled directional spontaneous emission of photons into a nanophotonic waveguide. *Nature Communications*, 5:5713, December 2014.

- [11] Peter Lodahl, Sahand Mahmoodian, Søren Stobbe, Arno Rauschenbeutel, Philipp Schneeweiss, Jürgen Volz, Hannes Pichler, and Peter Zoller. Chiral quantum optics. *Nature*, 541(7638):473–480, January 2017.
- [12] C. Sayrin, C. Clausen, B. Albrecht, P. Schneeweiss, and A. Rauschenbeutel. Storage of fiber-guided light in a nanofiber-trapped ensemble of cold atoms. *Optica*, 2(4):353–356, April 2015.
- [13] B. Gouraud, D. Maxein, A. Nicolas, O. Morin, and J. Laurat. Demonstration of a Memory for Tightly Guided Light in an Optical Nanofiber. *Physical Review Letters*, 114(18):180503, May 2015.
- [14] Clément Sayrin, Christian Junge, Rudolf Mitsch, Bernhard Albrecht, Danny O’Shea, Philipp Schneeweiss, Jürgen Volz, and Arno Rauschenbeutel. Nanophotonic Optical Isolator Controlled by the Internal State of Cold Atoms. *Physical Review X*, 5(4):041036, December 2015.
- [15] L.-M. Duan, M. D. Lukin, J. I. Cirac, and P. Zoller. Long-distance quantum communication with atomic ensembles and linear optics. *Nature*, 414(6862):413–418, November 2001.
- [16] Neil V. Corzo, Jérémy Raskop, Aveek Chandra, Alexandra S. Sheremet, Baptiste Gouraud, and Julien Laurat. Waveguide-coupled single collective excitation of atomic arrays. *Nature*, 566(7744):359–362, February 2019.
- [17] Neil V. Corzo, Baptiste Gouraud, Aveek Chandra, Akihisa Goban, Alexandra S. Sheremet, Dmitriy V. Kupriyanov, and Julien Laurat. Large Bragg Reflection from One-Dimensional Chains of Trapped Atoms Near a Nanoscale Waveguide. *Physical Review Letters*, 117(13):133603, September 2016.
- [18] H. L. Sørensen, J.-B. Béguin, K. W. Kluge, I. Iakoupov, A. S. Sørensen, J. H. Müller, E. S. Polzik, and J. Appel. Coherent Backscattering of Light Off One-Dimensional Atomic Strings. *Physical Review Letters*, 117(13):133604, September 2016.
- [19] Sarah M. Skoff, David Papencordt, Hardy Schauffert, Bernhard C. Bayer, and Arno Rauschenbeutel. Optical-nanofiber-based interface for single molecules. *Physical Review A*, 97(4):043839, April 2018.
- [20] Chao Meng, Yao Xiao, Pan Wang, Lei Zhang, Yanxin Liu, and Limin Tong. Quantum-Dot-Doped Polymer Nanofibers for Optical Sensing. *Advanced Materials*, 23(33):3770–3774, 2011.
- [21] Amnon Yariv. *Optical Electronics*. The Holt, Rinehart and Winston Series in Electrical Engineering. Saunders College Publ, Fort Worth, TX, 4th ed edition, 1991.
- [22] Rudolf Grimm, Matthias Weidemüller, and Yuri B. Ovchinnikov. Optical Dipole Traps for Neutral Atoms. In Benjamin Bederson and Herbert Walther, editors, *Advances In Atomic, Molecular, and Optical Physics*, volume 42, pages 95–170. Academic Press, January 2000.

- [23] Cecilia Muldoon, Lukas Brandt, Jian Dong, Dustin Stuart, Edouard Brainis, Matthew Himsworth, and Axel Kuhn. Control and manipulation of cold atoms in optical tweezers. *New Journal of Physics*, 14(7):073051, July 2012.
- [24] A. M. Kaufman, B. J. Lester, and C. A. Regal. Cooling a Single Atom in an Optical Tweezer to Its Quantum Ground State. *Physical Review X*, 2(4):041014, November 2012.
- [25] Manuel Endres, Hannes Bernien, Alexander Keesling, Harry Levine, Eric R. Anschuetz, Alexandre Krajenbrink, Crystal Senko, Vladan Vuletic, Markus Greiner, and Mikhail D. Lukin. Atom-by-atom assembly of defect-free one-dimensional cold atom arrays. *Science*, 354(6315):1024–1027, November 2016.
- [26] Waseem S. Bakr, Jonathon I. Gillen, Amy Peng, Simon Fölling, and Markus Greiner. A quantum gas microscope for detecting single atoms in a Hubbard-regime optical lattice. *Nature*, 462(7269):74–77, November 2009.
- [27] Immanuel Bloch, Jean Dalibard, and Sylvain Nascimbène. Quantum simulations with ultracold quantum gases. *Nature Physics*, 8(4):267–276, April 2012.
- [28] C.-L. Hung, S. M. Meenehan, D. E. Chang, O. Painter, and H. J. Kimble. Trapped atoms in one-dimensional photonic crystals. *New Journal of Physics*, 15(8):083026, August 2013.
- [29] T. G. Tiecke, J. D. Thompson, N. P. de Leon, L. R. Liu, V. Vuletić, and M. D. Lukin. Nanophotonic quantum phase switch with a single atom. *Nature*, 508(7495):241–244, April 2014.
- [30] Fam Le Kien, Philipp Schneeweiss, and Arno Rauschenbeutel. Dynamical polarizability of atoms in arbitrary light fields: General theory and application to cesium. *The European Physical Journal D*, 67(5):92, May 2013.
- [31] Fam Le Kien, V. I. Balykin, and K. Hakuta. Atom trap and waveguide using a two-color evanescent light field around a subwavelength-diameter optical fiber. *Physical Review A*, 70(6):063403, December 2004.
- [32] Fam Le Kien, P. Schneeweiss, and A. Rauschenbeutel. State-dependent potentials in a nanofiber-based two-color trap for cold atoms. *Physical Review A*, 88(3):033840, September 2013.
- [33] N. Schlosser, G. Reymond, and P. Grangier. Collisional Blockade in Microscopic Optical Dipole Traps. *Physical Review Letters*, 89(2):023005, June 2002.
- [34] M. O. Brown, T. Thiele, C. Kiehl, T.-W. Hsu, and C. A. Regal. Gray-Molasses Optical-Tweezer Loading: Controlling Collisions for Scaling Atom-Array Assembly. *Physical Review X*, 9(1):011057, March 2019.
- [35] B. Albrecht, Y. Meng, C. Clausen, A. Dureau, P. Schneeweiss, and A. Rauschenbeutel. Fictitious magnetic-field gradients in optical microtraps as an experimental tool for interrogating and manipulating cold atoms. *Physical Review A*, 94(6):061401, December 2016.

- [36] Y. Meng, A. Dureau, P. Schneeweiss, and A. Rauschenbeutel. Near-Ground-State Cooling of Atoms Optically Trapped 300 nm Away from a Hot Surface. *Physical Review X*, 8(3):031054, September 2018.
- [37] Daniel Hümmer, Philipp Schneeweiss, Arno Rauschenbeutel, and Oriol Romero-Isart. Heating in Nanophotonic Traps for Cold Atoms. *arXiv:1902.02200 [cond-mat, physics:physics, physics:quant-ph]*, February 2019.
- [38] C. Wuttke and A. Rauschenbeutel. Thermalization via Heat Radiation of an Individual Object Thinner than the Thermal Wavelength. *Physical Review Letters*, 111(2):024301, July 2013.
- [39] Eugen Vetsch. *Optical Interface Based on a Nanofiber Atom-Trap*. PhD thesis, Johannes Gutenberg-Universität Mainz, Mainz, 2010.
- [40] Sahand Mahmoodian, Mantas Čepulkovskis, Sumanta Das, Peter Lodahl, Klemens Hammerer, and Anders S. Sørensen. Strongly Correlated Photon Transport in Waveguide Quantum Electrodynamics with Weakly Coupled Emitters. *Physical Review Letters*, 121(14):143601, October 2018.
- [41] Christopher Gerry and Peter Knight. *Introductory Quantum Optics*. Cambridge: Cambridge University Press., 2004.
- [42] Roy J. Glauber. Coherent and Incoherent States of the Radiation Field. *Physical Review*, 131(6):2766–2788, September 1963.
- [43] Horace P. Yuen. Two-photon coherent states of the radiation field. *Physical Review A*, 13(6):2226–2243, June 1976.
- [44] A. I. Lvovsky. Squeezed light. *arXiv:1401.4118 [physics, physics:quant-ph]*, January 2014.
- [45] Jung-Tsung Shen and Shanhui Fan. Strongly correlated multiparticle transport in one dimension through a quantum impurity. *Physical Review A*, 76(6):062709, December 2007.
- [46] Sahand Mahmoodian. Squeezing in chiral waveguide QED. *private communications*, 0(0):8, May 2018. 0.
- [47] Shanhui Fan, Şükrü Ekin Kocabaş, and Jung-Tsung Shen. Input-output formalism for few-photon transport in one-dimensional nanophotonic waveguides coupled to a qubit. *Physical Review A*, 82(6):063821, December 2010.
- [48] D. F. Walls and G. J. Milburn. *Quantum Optics*. Springer, Berlin, 2nd ed edition, 2008.
- [49] Adarsh Prasad. *PhD Thesis (in Preparation)*. PhD thesis, TU Wien, 2020.
- [50] Harold J. Metcalf and Peter van der Straten. *Laser Cooling and Trapping*. Graduate Texts in Contemporary Physics. Springer-Verlag, New York, 1999.

- [51] Mark Kasevich and Steven Chu. Laser cooling below a photon recoil with three-level atoms. *Physical Review Letters*, 69(12):1741–1744, September 1992.
- [52] J. Dalibard and C. Cohen-Tannoudji. Laser cooling below the Doppler limit by polarization gradients: Simple theoretical models. *JOSA B*, 6(11):2023–2045, November 1989.
- [53] Daniel Steck. Cesium D Line Data. *available online at <http://steck.us/alkalidata>*, December 2010.
- [54] Wolfgang Demtröder. *Experimentalphysik 1: Mechanik und Wärme*. Springer-Lehrbuch. Springer Spektrum, 8 edition, 2018.
- [55] Martin Blaha. *Combined Polarisation and Absorption Imaging for Experiments with Nanofiber Trapped Atoms*. PhD thesis, May 2016.
- [56] Ertner, Sebastian. Constuction of a Microwave Setup for Hyperfine Transitions in Cesium. Technical report, April 2016.
- [57] Fam Le Kien, S. Dutta Gupta, V. I. Balykin, and K. Hakuta. Spontaneous emission of a cesium atom near a nanofiber: Efficient coupling of light to guided modes. *Physical Review A*, 72(3):032509, September 2005.
- [58] Sebastian Pucher. Spectroscopy of the $6S_{1/2}$ to $5D_{5/2}$ Electric Quadrupole Transition of Atomic Cesium. Technical report, September 2018.
- [59] Michael Steinacher. Balanced Photo-Detector (BPD), 2017.
- [60] Jürgen Appel, Dallas Hoffman, Eden Figueroa, and A. I. Lvovsky. Electronic noise in optical homodyne tomography. *Physical Review A*, 75(3):035802, March 2007.
- [61] Laurin Ostermann, Clément Meignant, Claudiu Genes, and Helmut Ritsch. Super- and subradiance of clock atoms in multimode optical waveguides. *New Journal of Physics*, 21(2):025004, February 2019.
- [62] Aisling Johnson, Martin Blaha, Alexander E. Ulanov, Arno Rauschenbeutel, Philipp Schneeweiss, and Jürgen Volz. Observation of Multimode Strong Coupling of Cold Atoms to a 30-m Long Optical Resonator. *arXiv:1905.07353 [quant-ph]*, May 2019.
- [63] Bastian Hacker. *Two-Photon Gate and Creation of Optical Cat States Using One Atom in a Cavity*. PhD thesis, TU München, 2018.
- [64] A. Asenjo-Garcia, M. Moreno-Cardoner, A. Albrecht, H. J. Kimble, and D. E. Chang. Exponential Improvement in Photon Storage Fidelities Using Subradiance and “Selective Radiance” in Atomic Arrays. *Physical Review X*, 7(3):031024, August 2017.
- [65] Henning Vahlbruch, Moritz Mehmet, Karsten Danzmann, and Roman Schnabel. Detection of 15 dB Squeezed States of Light and their Application for the Absolute Calibration of Photoelectric Quantum Efficiency. *Physical Review Letters*, 117(11):110801, September 2016.

BIBLIOGRAPHY

- [66] R. M. Shelby, M. D. Levenson, S. H. Perlmutter, R. G. DeVoe, and D. F. Walls. Broad-Band Parametric Deamplification of Quantum Noise in an Optical Fiber. *Physical Review Letters*, 57(6):691–694, August 1986.
- [67] Avik Dutt, Kevin Luke, Sasikanth Manipatruni, Alexander L Gaeta, Paulo Nussenzveig, and Michal Lipson. On-Chip Optical Squeezing. *Phys. Rev. Applied*, 3(044005):7, 2015.
- [68] Warwick P Bowen and Gerard J Milburn. *Quantum Optomechanics*. CRC Press, 2015.

Acknowledgments

The past five years were an intense and challenging time. It wouldn't have been possible to complete this work without the support from a great number of people.

The *Applied Quantum Physics* group at the Atominstitut was a great academic family. It speaks volumes that we ended up in our common room on many evenings discussing pretty much everything, sometimes also Physics. As the head of the group Arno Rauschenbeutel created an environment where everyone felt free to take the time and sit down for a coffee (or a beer, from our genius hidden beer wall) and join the company. I learned tremendously from the many discussions with Jürgen Volz, both in the field of physics and politics. His patience with our understanding and his intuitive way of describing the physics and relate it back to fundamental principles is legion. Without his ideas and advice this PhD may not have succeeded. Thank you! Very useful ideas and feedback were also always available from Philipp Schneeweiss. I am particularly thankful to my second thesis advisor Thorsten Schumm. His encouragement at the difficult stages of the PhD was a great support. Thank you.

Philipp Treutlein and Jörg Helge Müller kindly agreed to examine my thesis. Thank you very much!

In the beginning of the experiment construction our little ERC team was lead by Christoph Clausen who is a great physicist and taught me much about electronics, coding and of course physics. Adarsh Prasad and I started together with our PhDs. It has been a challenging journey but I am happy that both of us concluded with a nice result. Sam Rind joined the experiment as a Maser student and has become a dear friend. I taught him some physics and he taught me how to single-handedly fire a shotgun. Thank you! Max Schemmer joined our team towards the end of my PhD time and without his hard work the squeezing measurement would probably not have worked out in time. Thank you! A golden memory will always be the legendary band that was Entdenker, made of many dear people from our group: Hardy Schauffert (git), Master Luke (voc), Martin Blaha (drums), Alexandre Dareau (piano, synth), Aisling Johnson (bass), Daniele De Bernardis (also bass) and the honorary member of Yijian Deckard Meng. Great colleagues and lab neighbours were also Michael Scheucher, Bernhard Albrecht, Stefan Walser, Thomas Hoinkes, Fam LeKien, Sebastian Pucher, Elisa Will, and Sarah Skoff. Thank you all!

The greater family at the Atominstitut is also full of nice people. Barbara Stros, Evgenya Schimpf, Rici Cerny, Britta Buchberger, and before they left ATI also Zorica Jelovic and Melissa König were extremely supportive with pretty much every administrative aspect, from travel reimbursement to the notorious time sheets. Thank you! Stephan Schneider is a true gem for the ATI, taking care of so many organisational matters and always with an attitude of 'We can talk about it' (it being my ridiculous critique or request). I am thankful for the friendship or

company of many other great people at ATI, Kjeld Beeks, Tiantian Zhang, Marion Mallweger, Filippo Borselli, Frederik Møller, and many more, including my favorite Piefke-bully Hannes Majer.

Another great circle of people is the graduate school CoQuS that is jointly hosted by TU Wien and Vienna University. The numerous CoQuS retreats are golden memories, in particular Shanghai this year. Thank you for the fun times Yuri Minoguchi, Lorenzo Magrini, Ralf Riedel, Valentin Zauner, Giuseppe Calarco, Daniel Hartley, Daniel Wirtitsch, and many other good people. To this day I often think back to my friend Tom Milburn. You are missed.

My three months in New York were a precious experience due to great people like Oscar Jiminez, Aseema Mohanty, Brian Stern, Steven Miller, Gaurang Bhatt, Samantha Roberts, and the entire Lipson Nanophotonics Group. Thank you, I am stoked to be back with you! Thank you also to Michal Lipson for giving me the opportunity and for asking me to come back.

Finally, I am deeply grateful for the support of my amazing family. Thank you all.

Vienna, October 2019

LEBENS LAUF

Jakob Gillespie Hinney
Badhausgasse 1-3/44
jakob.hinney@gmx.de
1070 Wien
Österreich

Persönliche Daten

Geburtsdatum: 27. Juni 1989
Geburtsort: Mannheim-Neckarau
Staatsangehörigkeit: deutsch

Ausbildung

seit 10/2014	Technische Universität Wien Doktorand in Technischer Physik
09/2013 – 08/2014	University of Strathclyde, Glasgow, Großbritannien Master of Philosophy
09/2009 – 05/2003	Ludwig-Maximilians-Universität, München and University of Alberta, Edmonton, Canada Bachelor of Science in Physik
1999 – 2008	Elisabeth von Thadden Schule, Heidelberg